

# 1D/2D NANOSTRUCTURED HYBRID FILMS FOR APPLICATION IN ELECTROCATALYTIC ENERGY CONVERSION/ STORAGE REACTIONS

Marcos Daniel Ribeiro Rocha

Mestrado em Química

Departamento de Química e Bioquímica

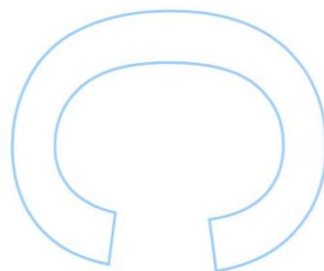
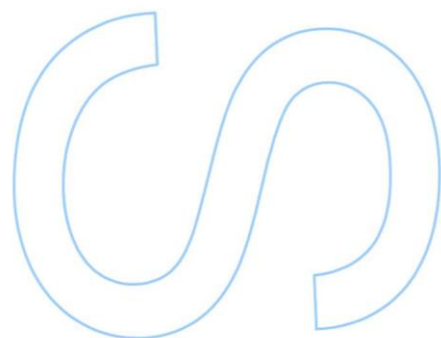
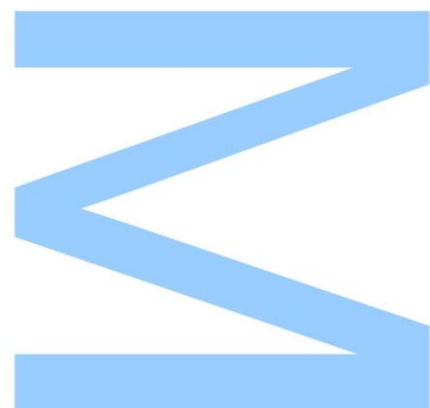
2021

**Orientador**

Professor Doutor Eduardo Jorge Figueira Marques, Professor Associado, FCUP

**Coorientador**

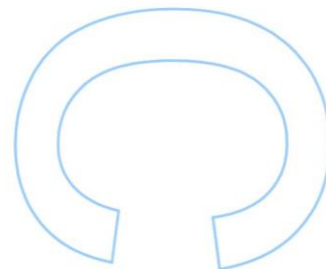
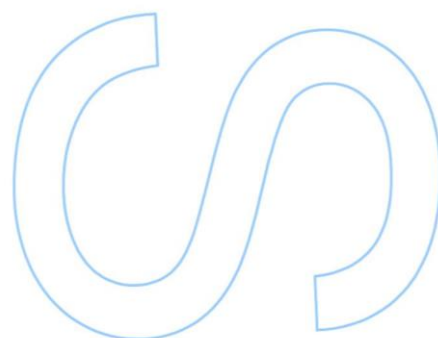
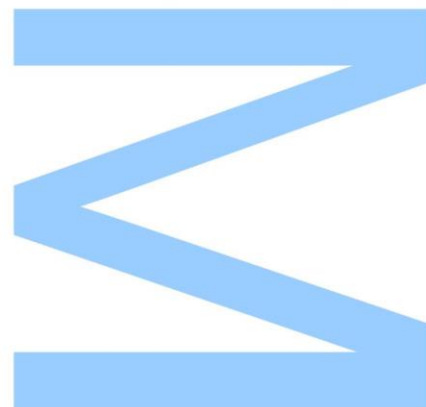
Doutora Marta Susete da Silva Nunes, Investigadora Auxiliar, LAQV-REQUIMTE





Todas as correções determinadas  
pelo júri, e só essas, foram efetuadas.  
O Presidente do Júri,

Porto, \_\_\_\_/\_\_\_\_/\_\_\_\_



## Acknowledgements

First of all, I would like to express my gratitude by the experience and memories created during these last two years of my academic career at the Faculty of Sciences of Porto University. It was a very laborious and arduous path, not only due to the academic challenges, but also because the problems and warnings imposed by the Covid-19 pandemic situation, that required a constant adaptation. So, I start by saying thank you:

To professor Eduardo Marques by the availability shown and knowledge transmitted during the development of my master's thesis. I would also like to thank by his work as teacher and director of the Master's degree in Chemistry at Faculty of Sciences of Porto University.

To Dr. Marta Nunes by her assistance and patience. I learned fundamental bases that I will keep with me. I also thank you for your support and dedication, it was a pleasure working with you.

To Dr. Bárbara Abreu, who, as also in the development of my final graduation project, helped in the progress of this work.

To my friends and colleagues, thank you for the good times. I will always remember these academic periods with you.

To my parents by their unconditional love from the very first moment. I love both of you with all my heart. I am very proud to be your son.

And lastly, to my dear twin brother Bruno Rocha, the person that I most admire and respect. You are the best brother that I could ever have. I will always love you and I wish to create even more memories with you in the years to come. We both went through a lot this past year once, just like me, you also worked for your master's thesis; but I am sure that with mutual support we will be able to overcome even more challenging barriers. Thank you for being just the way you are!

## Resumo

A obtenção de nanocompósitos avançados com propriedades melhoradas ou novas funcionalidades é um tópico desafiante na área das nanociências e da nanotecnologia. Estes materiais híbridos são desenvolvidos a partir da combinação criteriosa de dois ou mais constituintes. Os blocos de construção poderão apresentar diferentes propriedades e dimensionalidade, e após a sua combinação efeitos sinérgicos poderão ser obtidos no novo material desenvolvido.

Este trabalho teve como principal objetivo o desenvolvimento de novos nanocompósitos e o seu estudo como eletrocatalisadores para as reações de oxigénio, fulcrais em aplicações relacionados com a conversão e o armazenamento de energia, como, por exemplo, as pilhas de combustível e as baterias de metal-ar. Assim, pretendeu-se inicialmente desenvolver dois tipos de materiais: (i) nanocompósitos 2D constituídos por um dicalcogeneto de um metal de transição, o  $\text{MoS}_2$ , e nanoplaquetas de grafeno (GnPs), originando nanocompósitos do tipo  $\text{MoS}_2@\text{GnP}$ ; (ii) nanocompósitos 3D, constituídos pelo material híbrido  $\text{MoS}_2@\text{GnP}$  e nanotubos de carbono de parede múltipla (MWNTs) -  $(\text{MoS}_2@\text{GnP})@\text{MWNT}$ . Foram exploradas várias metodologias para a preparação dos nanocompósitos, baseadas em processos de esfoliação em fase líquida assistida por tensioativos e esfoliação micromecânica, por moinho de bolas. A funcionalização não covalente dos nanomateriais com recurso a tensioativos e polímeros permitiu o controlo da composição dos nanocompósitos preparados. Os componentes de partida e os nanocompósitos preparados foram posteriormente caracterizados por microscopia eletrónica de varrimento (SEM) e difração de raios-X de pó (P-XRD).

Adicionalmente, os nanocompósitos foram estudados como possíveis eletrocatalisadores eficientes para as reações de oxigénio, designadamente para a reação de redução do oxigénio (ORR) e a reação de evolução do oxigénio (OER).

A caracterização por SEM comprovou a influência dos métodos de preparação na estruturação do material e, para os nanocompósitos 3D, foi revelado que os MWNTs interagiram com o material híbrido  $\text{MoS}_2@\text{GnP}$ . Através da técnica de P-XRD foi demonstrada a presença dos nanomateriais de partida nos nanocompósitos, indicando assim a sua preparação bem-sucedida.

Os estudos eletroquímicos forneceram informações sobre a cinética das reações e a relação estrutura-atividade entre os nanocompósitos e os parâmetros eletrocatalíticos. Particularmente, foi investigada a influência do uso de diferentes proporções mássicas entre os componentes dos nanocompósitos, bem como a influência da dopagem das GnPs com nitrogénio no desempenho eletrocatalítico observado. Os materiais híbridos

mais promissores de entre os preparados foram selecionados tendo em conta o desempenho eletrocatalítico e também a simplicidade do processo de preparação utilizado. No geral, os materiais apresentaram um bom desempenho eletrocatalítico para ORR e OER. Os materiais mais promissores apresentaram ainda boa estabilidade a longo prazo e tolerância ao metanol.

**Palavras-chave:** Nanomateriais de carbono; Dicalcogenetos de metais de transição; Nanocompósitos; Funcionalização não-covalente; Tensioativos; Reações eletrocatalíticas do oxigénio.

## Abstract

The preparation of advanced nanocomposites with improved properties or new functionalities is a challenging topic in the field of nanoscience and nanotechnology. These hybrid materials are developed from the appropriate combination of two or more components. The building blocks may have different properties and dimensionality, and after their combination synergistic effects can be obtained in the new developed material.

This work aimed at the development of new nanocomposites and their study as electrocatalysts for oxygen reactions, pivotal to applications related to energy conversion and storage, such as, for example, fuel cells and metal-air batteries. Thus, the initial goal was to develop two types of materials: (i) 2D nanocomposites, consisting of a transition metal dichalcogenide,  $\text{MoS}_2$ , and graphene nanoplatelets (GnPs), originating  $\text{MoS}_2$ @GnP-type nanocomposites; (ii) 3D nanocomposites, consisting of the hybrid  $\text{MoS}_2$ @GnP material and multi-walled carbon nanotubes (MWNTs), leading to  $(\text{MoS}_2$ @GnP)@MWNT. Several methodologies were explored for the preparation of the nanocomposites, based on surfactant-assisted liquid phase exfoliation and micromechanical exfoliation by ball milling. The non-covalent functionalization of the nanomaterials using surfactants and polymers allowed the control of the composition of the prepared nanocomposites. The starting components and the prepared nanocomposites were subsequently characterized by scanning electron microscopy (SEM) and powder X-ray diffraction (P-XRD).

Additionally, the nanocomposites were studied as possible efficient electrocatalysts for oxygen reactions, namely for the oxygen reduction reaction (ORR) and the oxygen evolution reaction (OER).

SEM characterization demonstrated the influence of the preparation methods on the structure of the composite materials, and further revealed that in the 3D nanocomposites the MWNTs interact strongly with the 2D  $\text{MoS}_2$ @GnP hybrid. By P-XRD, the presence of the starting nanomaterials in the nanocomposites was corroborated, thus indicating the successful preparation of the latter.

The electrochemical studies provided information about the kinetics of the reactions and the structure-activity relationship between the nanocomposites and the electrocatalytic parameters. In particular, the influence of using different mass ratios between the components of the nanocomposites as well as the influence of doping the GnPs with nitrogen on the observed electrocatalytic performance was investigated. The most promising hybrid materials among those prepared was selected taking into account the electrocatalytic performance and also the simplicity of the preparation process. Overall, the materials showed good electrocatalytic performance for ORR and OER. The

most promising materials also showed good long-term stability and tolerance to methanol crossover.

**Keywords:** Carbon nanomaterials; Transition metal dichalcogenides; Nanocomposites; Non-covalent functionalization; Surfactants; Electrocatalytic oxygen reactions.

# Index

Acknowledgements.....	iii
Resumo .....	iv
Abstract .....	vi
Index.....	viii
List of figures .....	xi
List of tables .....	xvi
List of abbreviations, acronyms and symbols.....	xvii
1. Introduction.....	2
1.1. Carbon Nanomaterials.....	2
1.1.1. Carbon Nanotubes .....	4
1.1.2. Graphene .....	5
1.1.3. Heteroatom-doped Carbon Nanomaterials .....	6
1.2. Transition Metal Dichalcogenides .....	7
1.3. Hybrid Nanocomposites.....	8
1.3.1. Van der Waals heterostructures.....	9
1.3.1.1. Assembly Methods.....	10
1.4. Dispersion and Functionalization of Nanomaterials.....	12
1.4.1. Mechanical Dispersion Processes .....	13
1.4.2. Dispersant Agents .....	14
1.5. Electrochemical-related Technologies .....	16
1.5.1. Metal-Air Batteries and Fuel Cells.....	16
1.5.2. Oxygen Reactions.....	18
1.5.3. Benchmarking Electrocatalysts and Novel Electrocatalysts.....	21
1.6. Scope of this Work.....	22
2. Experimental Section.....	25
2.1. Materials, reagents and solvents .....	25
2.2. Nanocomposites Preparation.....	25
2.2.1. One-Step Dispersion .....	27

2.2.2.	Two-Step Dispersion .....	29
2.2.3.	Ball Milling .....	31
2.2.4.	Preparation of MoS <sub>2</sub> @N-GnP and (MoS <sub>2</sub> @N-GnP)@MWNT materials .....	33
2.3.	Characterization Techniques .....	34
2.4.	Electrochemical studies .....	35
2.4.1.	ORR studies .....	36
2.4.2.	OER studies .....	37
3.	Results and Discussion.....	39
3.1.	Materials characterization .....	39
3.1.1.	Scanning Electron Microscopy.....	39
3.1.1.1.	Starting materials .....	39
3.1.1.2.	MoS <sub>2</sub> @GnP nanocomposites.....	40
3.1.1.3.	(MoS <sub>2</sub> @GnP)@MWNT nanocomposites.....	42
3.1.2.	P-XRD characterization .....	46
3.2.	Electrocatalytic activity for the oxygen reactions .....	48
3.2.1.	ORR electrocatalytic activity .....	48
3.2.1.1.	MoS <sub>2</sub> @GnP nanocomposites.....	48
I.	<i>Influence of the preparation methods</i> .....	48
II.	<i>Influence of different mass ratios between building blocks</i> .....	51
III.	<i>Influence of nitrogen doping on GnPs</i> .....	53
3.2.1.2.	(MoS <sub>2</sub> @GnP)@MWNT nanocomposites.....	54
I.	<i>Influence of the preparation method</i> .....	54
II.	<i>Influence of different mass ratios between building blocks</i> .....	57
III.	<i>Influence of nitrogen doping on GnPs</i> .....	58
3.2.1.2.	Chronoamperometry assays .....	60
3.2.2.	OER electrocatalytic performance .....	62
3.2.2.1.	MoS <sub>2</sub> @GnP nanocomposites.....	63
I.	<i>Influence of the preparation methods</i> .....	63
II.	<i>Influence of different mass ratios between building blocks</i> .....	64

III.	<i>Influence of nitrogen doping on GnPs</i> .....	65
3.2.2.2.	<i>(MoS<sub>2</sub>@GnP)@MWNT nanocomposites</i> .....	66
I.	<i>Influence of the preparation methods</i> .....	66
II.	<i>Influence of different mass ratios between building blocks</i> .....	67
III.	<i>Influence of nitrogen doping on GnPs</i> .....	68
3.3.	Overview of the electrocatalytic properties of the nanocomposites .....	68
4.	Conclusions and Future Perspectives .....	73
	References .....	75
	Appendix .....	86
A.1.	CVs of the materials in N <sub>2</sub> - and O <sub>2</sub> -saturated solutions .....	86
A.2.	ORR polarization plots at several rotation rates .....	90
A.3.	ORR polarization Koutecky-Levich (K-L) plots .....	94

## List of figures

Figure 1. Structures of different carbon allotropes. <sup>3</sup> .....	3
Figure 2. Schematic representation of the single-walled carbon nanotube (SWNTs) and multi-walled carbon nanotube (MWNTs) structures. <sup>12</sup> .....	4
Figure 3. <b>a</b> Side view of the molecular structure of MoS <sub>2</sub> . <b>b</b> Schematic representation of unit cell structures of 2H-MX <sub>2</sub> and 1T-MX <sub>2</sub> . <sup>32</sup> .....	7
Figure 4. Schematic representation of the assembly of a vdW heterostructure and analogy of 2D graphene, TMDs, h-BN and fluorographene crystals to Lego pieces. <sup>53</sup>	10
Figure 5. Schematic representation of an assembly method between graphene oxide and single-layer MoS <sub>2</sub> based on dispersion-processing. Adapted from ref. <sup>52</sup> .....	12
Figure 6. Sequential steps of the CNTs isolation process through sonication and surfactant functionalization, lines – CNTs, dots – dispersant agent. <sup>4</sup> .....	14
Figure 7. Illustration of a metal-air battery and its operation mode. <sup>92</sup> .....	17
Figure 8. Illustration of a fuel cell (right), combined with an electrolyzer (left) and their operational scheme. ....	18
Figure 9. Different experimental procedures explored for the preparation of the MoS <sub>2</sub> @GnP and the (MoS <sub>2</sub> @GnP)@MWNT nanocomposites. ....	26
Figure 10. Flowchart of the sequential preparation order by method a) of the one-step dispersion procedure, with the alternative routes of the synthesis of the 1S_E and 1S_E@MWNT nanocomposites. ....	28
Figure 11. Flowchart of the sequential order preparation by method b) of the One-step dispersion procedure, with the alternative routes of the synthesis of the 1S_F and 1S_F@MWNT nanocomposites. ....	29
Figure 12. Flowchart of the sequential preparation order by the two-step dispersion procedure, with the alternative routes of the synthesis of the 2S and 2S@MWNT nanocomposites. ....	30
Figure 13. Flowchart of the sequential preparation order by method a) of the ball milling procedure, with the alternative routes of the synthesis of the BM_wos and BM_wos@MWNT nanocomposites. ....	32
Figure 14. Flowchart of the sequential preparation order by method b) of the ball milling procedure, with the alternative routes of the synthesis of the BM_ws and BM_ws@MWNT nanocomposite. ....	33
Figure 15. SEM micrographs, obtained at 50,000x magnification of: <b>a</b> MWNTs; <b>b</b> MoS <sub>2</sub> ; <b>c</b> GnPs and <b>d</b> N-GnPs. ....	39

Figure 16. SEM micrographs of the cross sections of: <b>a</b> and <b>b</b> – 1S_E ( <b>a</b> 3000x magnification; <b>b</b> 50000x magnification); <b>c</b> and <b>d</b> – 1S_F ( <b>c</b> 5000x magnification; <b>d</b> 50000x magnification).....	40
Figure 17. SEM micrographs of the cross sections of 2S <b>a</b> 5000x magnification (yellow arrow corresponds to the cellulose acetate substrate); <b>b</b> 50000x magnification).....	41
Figure 18. SEM micrographs of the cross sections of 1S_F(N-GnP) ( <b>a</b> 5000x magnification; <b>b</b> 20000x magnification).....	41
Figure 19. SEM micrographs of: <b>a</b> and <b>b</b> – BM_wos ( <b>a</b> 5000x magnification; <b>b</b> 50000x magnification); <b>c</b> and <b>d</b> – BM_ws ( <b>c</b> 3000x magnification; <b>d</b> 50000x magnification)....	42
Figure 20. SEM micrographs of the cross sections of: <b>a</b> and <b>b</b> – 1S_E@MWNT ( <b>a</b> 3000x magnification; <b>b</b> 20000x magnification); <b>c</b> and <b>d</b> – 1S_F@MWNT ( <b>c</b> 5000x magnification; <b>d</b> 50000x magnification); (yellow arrows – visible MWNT networks). ....	43
Figure 21. SEM micrographs of the cross sections of 2S@MWNT ( <b>a</b> 5000x magnification; <b>b</b> 50000x magnification); (yellow arrows – visible MWNT networks). ....	43
Figure 22. SEM micrographs of the cross sections of 1S_F@MWNT (1:3) ( <b>a</b> 5000x magnification; <b>b</b> 50000x magnification); (yellow arrows – visible MWNT networks). ...	44
Figure 23. SEM micrographs of the cross sections of: <b>a</b> and <b>b</b> – 1S_F(N-GnP)@MWNT (1:3) ( <b>a</b> 5000x magnification; <b>b</b> 20000x magnification); <b>c</b> and <b>d</b> – 1S_F(N-GnP)@MWNT (3:1) ( <b>c</b> 5000x magnification; <b>d</b> 100000x magnification); (yellow arrows – visible MWNT networks).....	45
Figure 24. SEM micrographs of: <b>a</b> and <b>b</b> – BM_wos@MWNT ( <b>a</b> 20000x magnification; <b>b</b> 200000x magnification); <b>c</b> and <b>d</b> – BM_ws@MWNT ( <b>c</b> 20000x magnification; <b>d</b> 200000x magnification). ....	46
Figure 25. P-XRD patterns of: GnPs; MoS <sub>2</sub> ; MWNTs; N-GnPs; 1S_F; 1S_F@MWNT (1:3); 1S_F(N-GnP); 1S_F(N-GnP) @MWNT (1:3) and 1S_F(N-GnP) @MWNT (3:1).47	
Figure 26. ORR electrocatalytic results for building blocks (MoS <sub>2</sub> and GnPs), MoS <sub>2</sub> @GnP nanocomposites (1S_E, 1S_F, 2S, BM_wos and BM_ws), and Pt/C: <b>a</b> CVs (O <sub>2</sub> -saturated 0.1 mol·dm <sup>-3</sup> KOH, $v = 0.005 \text{ V}\cdot\text{s}^{-1}$ ); <b>b</b> LSVs (O <sub>2</sub> -saturated 0.1 mol·dm <sup>-3</sup> KOH, $v = 0.005 \text{ V}\cdot\text{s}^{-1}$ , $\omega = 1600 \text{ rpm}$ ); <b>c</b> $n_{\text{O}_2}$ estimated at different potential values; <b>d</b> Tafel plots with the respective TS values. ....	49
Figure 27. ORR electrocatalytic results for 1S_F, 1S_F(9:1) and 1S_F(1:9) MoS <sub>2</sub> @GnP nanocomposites: <b>a</b> CVs (O <sub>2</sub> -saturated 0.1 mol·dm <sup>-3</sup> KOH, $v = 0.005 \text{ V}\cdot\text{s}^{-1}$ ); <b>b</b> LSVs (O <sub>2</sub> -saturated 0.1 mol·dm <sup>-3</sup> KOH, $v = 0.005 \text{ V}\cdot\text{s}^{-1}$ , $\omega = 1600 \text{ rpm}$ ); <b>c</b> $n_{\text{O}_2}$ estimated at different potential values; <b>d</b> Tafel plots with the respective TS values.....	52
Figure 28. ORR electrocatalytic results for the building blocks GnPs and N-GnPs and MoS <sub>2</sub> @GnP nanocomposites 1S_F and 1S_F(N-GnP): <b>a</b> CVs (O <sub>2</sub> -saturated 0.1 mol·dm <sup>-3</sup>	

<sup>3</sup> KOH, $v = 0.005 \text{ V}\cdot\text{s}^{-1}$ ); <b>b</b> LSVs ( $\text{O}_2$ -saturated $0.1 \text{ mol}\cdot\text{dm}^{-3}$ KOH, $v = 0.005 \text{ V}\cdot\text{s}^{-1}$ , $\omega = 1600 \text{ rpm}$ ); <b>c</b> $n_{\text{O}_2}$ estimated at different potential values; <b>d</b> Tafel plots with the respective TS values.....	54
Figure 29. ORR electrocatalytic results for MWNTs, $(\text{MoS}_2@\text{GnP})@\text{MWNT}$ nanocomposites ( $1\text{S}_\text{E}@\text{MWNT}$ , $1\text{S}_\text{F}@\text{MWNT}$ , $2\text{S}$ , $\text{BM}_\text{wos}@\text{MWNT}$ and $\text{BM}_\text{ws}@\text{MWNT}$ ), and Pt/C: <b>a</b> CVs ( $\text{O}_2$ -saturated $0.1 \text{ mol}\cdot\text{dm}^{-3}$ KOH, $v = 0.005 \text{ V}\cdot\text{s}^{-1}$ ); <b>b</b> LSVs ( $\text{O}_2$ -saturated $0.1 \text{ mol}\cdot\text{dm}^{-3}$ KOH, $v = 0.005 \text{ V}\cdot\text{s}^{-1}$ , $\omega = 1600 \text{ rpm}$ ); <b>c</b> $n_{\text{O}_2}$ estimated at different potential values; <b>d</b> Tafel plots with the respective TS values.....	55
Figure 30. ORR electrocatalytic results for the $(\text{MoS}_2@\text{GnP})@\text{MWNT}$ nanocomposites ( $1\text{S}_\text{F}@\text{MWNT}$ and $1\text{S}_\text{F}@\text{MWNT}$ (1:3)): <b>a</b> CVs ( $\text{O}_2$ -saturated $0.1 \text{ mol}\cdot\text{dm}^{-3}$ KOH, $v = 0.005 \text{ V}\cdot\text{s}^{-1}$ ); <b>b</b> LSVs ( $\text{O}_2$ -saturated $0.1 \text{ mol}\cdot\text{dm}^{-3}$ KOH, $v = 0.005 \text{ V}\cdot\text{s}^{-1}$ , $\omega = 1600 \text{ rpm}$ ); <b>c</b> $n_{\text{O}_2}$ estimated at different potential values; <b>d</b> Tafel plots with the respective TS values. ....	58
Figure 31. ORR electrocatalytic results for the $(\text{MoS}_2@\text{GnP})@\text{MWNT}$ nanocomposites ( $1\text{S}_\text{F}@\text{MWNT}$ , $1\text{S}_\text{F}@\text{MWNT}$ (1:3), $1\text{S}_\text{F}(\text{N-GnP})@\text{MWNT}$ (1:3) and $1\text{S}_\text{F}(\text{N-GnP})@\text{MWNT}$ (3:1)): <b>a</b> CVs ( $\text{O}_2$ -saturated $0.1 \text{ mol}\cdot\text{dm}^{-3}$ KOH, $v = 0.005 \text{ V}\cdot\text{s}^{-1}$ ); <b>b</b> LSVs ( $\text{O}_2$ -saturated $0.1 \text{ mol}\cdot\text{dm}^{-3}$ KOH, $v = 0.005 \text{ V}\cdot\text{s}^{-1}$ , $\omega = 1600 \text{ rpm}$ ); <b>c</b> $n_{\text{O}_2}$ estimated at different potential values; <b>d</b> Tafel plots with the respective TS values.....	59
Figure 32. <i>i-t</i> response curves obtained during <b>a</b> the stability studies and <b>b</b> the methanol resistance tests for selected 2D $\text{MoS}_2@\text{GnP}$ nanocomposites ( $1\text{S}_\text{F}$ and $1\text{S}_\text{F}(\text{N-GnP})$ ) and 3D $(\text{MoS}_2@\text{GnP})@\text{MWNT}$ nanocomposites ( $1\text{S}_\text{F}@\text{MWNT}$ (1:3) and $1\text{S}_\text{F}(\text{N-GnP})@\text{MWNT}$ (3:1)), and for Pt/C reference. $E_{\text{applied}} = 0.54 \text{ V}$ vs. RHE and $\omega = 1600 \text{ rpm}$ during 50000 s, in $\text{O}_2$ -saturated $0.1 \text{ mol}\cdot\text{dm}^{-3}$ KOH; in <b>b</b> addition of $0.5 \text{ mol}\cdot\text{dm}^{-3}$ methanol at 1000 s.....	60
Figure 33. <b>a</b> RDDE voltammograms of the $\text{MoS}_2@\text{GnP}$ nanocomposites ( $1\text{S}_\text{F}$ and $1\text{S}_\text{F}(\text{N-GnP})$ ), $(\text{MoS}_2@\text{GnP})@\text{MWNT}$ ( $1\text{S}_\text{F}@\text{MWNT}$ (1:3) and $1\text{S}_\text{F}(\text{N-GnP})@\text{MWNT}$ (3:1)) and Pt/C ( $\text{O}_2$ -saturated $0.1 \text{ mol}\cdot\text{dm}^{-3}$ KOH, $v = 0.005 \text{ V}\cdot\text{s}^{-1}$ , 1600 rpm). <b>b</b> Variation of the calculated percentages of $\text{H}_2\text{O}_2$ formed with the applied potential. ....	62
Figure 34. OER electrocatalytic results for the building blocks (pristine $\text{MoS}_2$ and $\text{GnPs}$ ), $\text{MoS}_2@\text{GnP}$ nanocomposites ( $1\text{S}_\text{E}$ , $1\text{S}_\text{F}$ , $2\text{S}$ , $\text{BM}_\text{wos}$ and $\text{BM}_\text{ws}$ ), and $\text{RuO}_2$ : <b>a</b> LSVs ( $\text{N}_2$ -saturated $0.1 \text{ mol}\cdot\text{dm}^{-3}$ KOH, $v = 0.005 \text{ V}\cdot\text{s}^{-1}$ , $\omega = 1600 \text{ rpm}$ ); <b>b</b> Tafel plots with the respective TS values.....	63
Figure 35. OER electrocatalytic results for the $\text{MoS}_2@\text{GnP}$ nanocomposites ( $1\text{S}_\text{F}$ , $1\text{S}_\text{F}(9:1)$ and $1\text{S}_\text{F}(1:9)$ ): <b>a</b> LSVs ( $\text{N}_2$ -saturated $0.1 \text{ mol}\cdot\text{dm}^{-3}$ KOH, $v = 0.005 \text{ V}\cdot\text{s}^{-1}$ , $\omega = 1600 \text{ rpm}$ ); <b>b</b> Tafel plots with the respective TS values.....	65

Figure 36. OER electrocatalytic results for the building blocks (GnP and N-GnP) and MoS<sub>2</sub>@GnP nanocomposites (1S\_F and 1S\_F(N-GnP)): **a** LSVs (N<sub>2</sub>-saturated 0.1 mol·dm<sup>-3</sup> KOH,  $v = 0.005 \text{ V}\cdot\text{s}^{-1}$ ,  $\omega = 1600 \text{ rpm}$ ); **b** Tafel plots with the respective TS values. .... 65

Figure 37. OER electrocatalytic results for the MWNTs, (MoS<sub>2</sub>@GnP)@MWNT nanocomposites (1S\_E@MWNT, 1S\_F@MWNT, 2S, BM\_wos@MWNT and BM\_ws@MWNT), and RuO<sub>2</sub>: **a** LSVs (N<sub>2</sub>-saturated 0.1 mol·dm<sup>-3</sup> KOH,  $v = 0.005 \text{ V}\cdot\text{s}^{-1}$ ,  $\omega = 1600 \text{ rpm}$ ); **b** Tafel plots with the respective TS values..... 66

Figure 38. OER electrocatalytic results for the (MoS<sub>2</sub>@GnP)@MWNT nanocomposites (1S\_F@MWNT and 1S\_F@MWNT (1:3)): **a** LSVs (N<sub>2</sub>-saturated 0.1 mol·dm<sup>-3</sup> KOH,  $v = 0.005 \text{ V}\cdot\text{s}^{-1}$ ,  $\omega = 1600 \text{ rpm}$ ); **b** Tafel plots with the respective TS values..... 67

Figure 39. OER electrocatalytic results for the (MoS<sub>2</sub>@GnP)@MWNT nanocomposites (1S\_F@MWNT (1:3), 1S\_F(N-GnP)@MWNT (1:3) and 1S\_F(N-GnP)@MWNT (3:1)): **a** LSVs (N<sub>2</sub>-saturated 0.1 mol·dm<sup>-3</sup> KOH,  $v = 0.005 \text{ V}\cdot\text{s}^{-1}$ ,  $\omega = 1600 \text{ rpm}$ ); **b** Tafel plots with the respective TS values..... 68

Figure 40. CVs of **a** GnPs, **b** MoS<sub>2</sub>, **c** 1S\_E, **d** 1S\_F, **e** 2S, **f** BM\_wos, **g** BM\_ws and **h** Pt/C, 0.1 mol·dm<sup>-3</sup> KOH N<sub>2</sub>- and O<sub>2</sub>-saturated solutions, at 0.005 V·s<sup>-1</sup>. .... 86

Figure 41. CVs of **a** 1S\_F(9:1) and **b** 1S\_F(1:9), 0.1 mol·dm<sup>-3</sup> KOH N<sub>2</sub>- and O<sub>2</sub>-saturated solutions, at 0.005 V·s<sup>-1</sup>..... 87

Figure 42. CVs of **a** N-GnPs and **b** 1S\_F(N-GnP), 0.1 mol·dm<sup>-3</sup> KOH N<sub>2</sub>- and O<sub>2</sub>-saturated solutions, at 0.005 V·s<sup>-1</sup>. .... 87

Figure 43. CVs of **a** MWNTs, **b** 1S\_E@MWNT, **c** 1S\_F@ MWNT, **d** 2S@MWNT, **e** BM\_wos@MWNT and **f** BM\_ws@MWNT, 0.1 mol·dm<sup>-3</sup> KOH N<sub>2</sub>- and O<sub>2</sub>-saturated solutions, at 0.005 V·s<sup>-1</sup>..... 88

Figure 44. CVs of 1S\_F@MWNT (1:3), 0.1 mol·dm<sup>-3</sup> KOH N<sub>2</sub>- and O<sub>2</sub>-saturated solutions, at 0.005 V·s<sup>-1</sup>. .... 88

Figure 45. CVs of **a** 1S\_F(N-GnP)@MWNT (1:3) and **b** 1S\_F(N-GnP)@MWNT (3:1), 0.1 mol·dm<sup>-3</sup> KOH N<sub>2</sub>- and O<sub>2</sub>-saturated solutions, at 0.005 V·s<sup>-1</sup>. .... 89

Figure 46. ORR polarization plots for **a** GnPs, **b** MoS<sub>2</sub>, **c** 1S\_E, **d** 1S\_F, **e** 2S, **f** BM\_wos, **g** BM\_ws and **h** Pt/C, at 100-3000 rpm and 0.005 V·s<sup>-1</sup>, in 0.1 mol·dm<sup>-3</sup> KOH. .... 90

Figure 47. ORR polarization plots for **a** 1S\_F(9:1) and **b** 1S\_F(1:9), at 100-3000 rpm and 0.005 V·s<sup>-1</sup>, in 0.1 mol·dm<sup>-3</sup> KOH..... 91

Figure 48. ORR polarization plots for **a** N-GnPs and **b** 1S\_F(N-GnP), at 100-3000 rpm and 0.005 V·s<sup>-1</sup>, in 0.1 mol·dm<sup>-3</sup> KOH..... 91

Figure 49. ORR polarization plots for <b>a</b> MWNTs, <b>b</b> 1S_E@MWNT, <b>c</b> 1S_F@ MWNT, <b>d</b> 2S@MWNT, <b>e</b> BM_wos@MWNT and <b>f</b> BM_ws@MWNT, at 100-3000 rpm and 0.005 V·s <sup>-1</sup> , in 0.1 mol·dm <sup>-3</sup> KOH. ....	92
Figure 50. ORR polarization plots for 1S_F@MWNT (1:3), at 100-3000 rpm and 0.005 V·s <sup>-1</sup> , in 0.1 mol·dm <sup>-3</sup> KOH. ....	92
Figure 51. ORR polarization plots for <b>a</b> 1S_F(N-GnP)@MWNT (1:3) and <b>b</b> 1S_F(N-GnP)@MWNT (3:1), at 100-3000 rpm and 0.005 V·s <sup>-1</sup> , in 0.1 mol·dm <sup>-3</sup> KOH. ....	93
Figure 52. ORR polarization Koutecky-Levich (K-L) plots for <b>a</b> GnPs, <b>b</b> MoS <sub>2</sub> , <b>c</b> 1S_E, <b>d</b> 1S_F, <b>e</b> 2S, <b>f</b> BM_wos, <b>g</b> BM_ws and <b>h</b> Pt/C, extracted from data in Figure 46.....	94
Figure 53. ORR polarization Koutecky-Levich (K-L) plots for <b>a</b> 1S_F(9:1) and <b>b</b> 1S_F(1:9), extracted from data in Figure 47.....	95
Figure 54. ORR polarization Koutecky-Levich (K-L) plots for <b>a</b> N-GnPs and <b>b</b> 1S_F(N-GnP), extracted from data in Figure 48. ....	95
Figure 55. ORR polarization Koutecky-Levich (K-L) plots for <b>a</b> MWNTs, <b>b</b> 1S_E@MWNT, <b>c</b> 1S_F@ MWNT, <b>d</b> 2S@MWNT, <b>e</b> BM_wos@MWNT and <b>f</b> BM_ws@MWNT, extracted from data in Figure 49.....	96
Figure 56. ORR polarization Koutecky-Levich (K-L) plots for 1S_F@MWNT (1:3), extracted from data in Figure 50. ....	96
Figure 57. ORR polarization Koutecky-Levich (K-L) plots for <b>a</b> 1S_F(N-GnP)@MWNT (1:3) and <b>b</b> 1S_F(N-GnP)@MWNT (3:1), extracted from data in Figure 51.....	97

## List of tables

Table 1. Main properties of graphene and CNTs, adapted from ref. <sup>3</sup> .....	5
Table 2. Reaction pathways of ORR in aqueous electrolytes, with the respective potentials (vs.RHE). <sup>94</sup> .....	19
Table 3. Reaction pathways of OER in aqueous electrolytes. <sup>94</sup> .....	21
Table 4. ORR electrocatalytic parameters obtained: $j_L$ , $E_{onset}$ , and $\tilde{n}_{O_2}$ values, for pristine MoS <sub>2</sub> , GnPs, N-GnPs, MoS <sub>2</sub> @GnP nanocomposites (1S_E, 1S_F, 2S, BM_wos, BM_ws, 1S_F(9:1), 1S_F(1:9) and 1S_F(N-GnP)) and Pt/C.....	50
Table 5. ORR electrocatalytic parameters obtained: $j_L$ , $E_{onset}$ , and $\tilde{n}_{O_2}$ , for MWNTs, (MoS <sub>2</sub> @GnP)@MWNT nanocomposites (1S_E@MWNT, 1S_F@MWNT, 2S, BM_wos@MWNT and BM_ws@MWNT, 1S_F@MWNT (1:3), 1S_F(N-GnP)@MWNT (1:3) and 1S_F(N-GnP)@MWNT (3:1)) and Pt/C.....	56
Table 6. OER electrocatalytic parameters, $j_{1.8}$ and TS, for the building blocks (MoS <sub>2</sub> , GnPs and N-GnPs), MoS <sub>2</sub> @GnP nanocomposites (1S_E, 1S_F, 2S, BM_wos, BM_ws, 1S_F(9:1), 1S_F(1:9) and 1S_F(N-GnP)), and RuO <sub>2</sub> reference.....	64
Table 7. OER electrocatalytic parameters, $j_{1.8}$ and TS, for MWNTs, (MoS <sub>2</sub> @GnP)@MWNT nanocomposites (1S_E@MWNT, 1S_F@MWNT, 2S, BM_wos@MWNT and BM_ws@MWNT, 1S_F@MWNT (1:3), 1S_F(N-GnP)@MWNT (1:3) and 1S_F(N-GnP)@MWNT (3:1)), and RuO <sub>2</sub> reference.....	66
Table 8. ORR electrocatalytic parameters for the most promising materials prepared: $j_L$ , $E_{onset}$ , and $\tilde{n}_{O_2}$ , for the MoS <sub>2</sub> @GnP nanocomposites (1S_F and 1S_F(N-GnP)), (MoS <sub>2</sub> @GnP)@MWNT (1S_F@MWNT (1:3) and 1S_F(N-GnP)@MWNT (3:1)) and Pt/C. ....	69
Table 9. Framing with the results reported in current literature regarding nanocomposites prepared from MoS <sub>2</sub> and carbon nanomaterials and applied as ORR electrocatalysts.	70
Table 10. OER electrocatalytic parameters, $j_{1.8}$ and TS, for MoS <sub>2</sub> @GnP nanocomposites (1S_F and 1S_F(N-GnP)), (MoS <sub>2</sub> @GnP)@MWNT (1S_F@MWNT (1:3) and 1S_F(N-GnP)@MWNT (3:1)) and RuO <sub>2</sub> .....	71

# List of abbreviations, acronyms and symbols

CNTs: Carbon nanotubes

$C_{O_2}$ : Bulk concentration of  $O_2$

CTAB: Cetyltrimethylammonium bromide

CV: Cyclic voltammetry

CVD: Chemical vapor deposition

$D_{O_2}$ :  $O_2$  diffusion coefficient

$E$ : Electric potential

$E^\circ$ : Standard electric potential

$E_{Ag/AgCl}$ : Electric potential vs. Ag/AgCl

$E^\circ_{Ag/AgCl}$ : Standard electric potential vs. Ag/AgCl

$E_{onset}$ : Onset potential

$E_{pc}$ : Potential of the cathodic peak

$E_{RHE}$ : Electric potential vs. RHE

$F$ : Faraday constant

GnPs: Graphene nanoplatelets

GO: Graphene oxide

HER: Hydrogen evolution reaction

HOR: Hydrogen oxidation reaction

$i_D$ : Disk currents

$i_R$ : Ring currents

$j$ : Current density

$j_k$ : Kinetic current density

$j_L$ : Diffusion-limiting current density

$j_{\max}$ : Maximum current density

$j_0$ : Exchange current density

$j_{1.8}$ : Current density at  $E = 1.8$  V vs. RHE

K-L: Koutecky-Levich

KOH: Potassium hydroxide

LSV: Linear sweep voltammetry

MOFs: Metal Organic Frameworks

MWNTs: Multi-walled carbon nanotubes

$N$ : Current collection efficiency of the platinum ring

N-GnPs: Nitrogen-doped GnPs

$n_{O_2}$ : Number of electrons transferred per molecule of  $O_2$

$\tilde{n}_{O_2}$ : Average number of electrons transferred per molecule of  $O_2$

OER: Oxygen Evolution Reaction

ORR: Oxygen Reduction Reaction

POMs: Polyoxometalates

PVP: Polyvinylpyrrolidone

P-XRD: Powder X-Ray Diffraction

RDE: Rotating disk electrode

RHE: Reversible hydrogen electrode

RRDE: Rotating ring disk electrode

$R_u$ : Uncompensated resistances

SALPE: Surfactant-assisted liquid phase exfoliation

SC: sodium cholate

SEM: Scanning electron microscopy

SWNTs: Single-walled carbon nanotubes

TGA: Thermogravimetric Analysis

$T_{kr}$ : Krafft temperature

TMDs: Transition metal dichalcogenides

TS: Tafel slope

TX-100: Triton™ X-100

UV-Vis: Ultraviolet Visible spectroscopy

vdW: Van der Waals

XPS: X-ray photoelectron spectroscopy

%H<sub>2</sub>O<sub>2</sub>: Percentage of H<sub>2</sub>O<sub>2</sub>

$\zeta$ : Zeta potential

$\eta$ : Overpotential

$\nu$ : Kinematic viscosity

$\omega$ : Angular velocity

# **Chapter 1**

## *Introduction*

# 1. Introduction

In this chapter, the theoretical foundations of the work developed will be addressed. Firstly, fundamental concepts about the different nanomaterials used — carbon nanotubes (CNTs), graphene and transition metal dichalcogenides (TMDs) — and hybrid nanocomposites will be presented. Next, we will address the various preparation methodologies and functionalization methods of nanomaterials employed. The last part will be dedicated to the target application, where an analysis of the state-of-the-art energy conversion and storage technologies and the main challenges to be overcome will be carried out.

## 1.1. Carbon Nanomaterials

Carbon is a one-of-a-kind chemical element. In nature, elemental carbon, with a ground state configuration of  $2s^2 2p^2$ , has the ability to form  $sp$ ,  $sp^2$  and  $sp^3$  hybrid bonds, giving rise to three distinct structures, respectively, amorphous carbon, graphite and diamond. Undoubtedly, different configurations imply different properties.<sup>1,2</sup>

Regarding diamond and graphite both are considered as the natural crystalline frameworks. However, due to the type of carbon hybridization they display unlike features. On one hand, diamond is transparent and possesses a  $sp^3$  carbon hybridization with a systematic regular pattern, which gives rise to its unique hardness.<sup>2</sup> Contrarily, graphite shows a black coloring and a soft texture. In graphite, each carbon atom is uniformly bonded with three neighbor carbons in a  $xy$  plane, as shown in Figure 1.<sup>3</sup> The  $sp^2$  hybridization forms a honeycomb-like lattice and has the characteristic of forming a weak  $\pi$  bond outside the plane, in the  $z$  axis. This later orbital,  $p_z$ , is responsible for the generation of a weak bond between each layer, namely the van der Waals (vdW) interaction. Here, the free electrons are no longer attached to a single carbon atom, so they are delocalized in a cloud. These delocalized  $\pi$  electrons lead graphite to behave as an electrical conductor. In contrast, diamond has a poor electrical conductivity, similar to an electrical insulator.<sup>1, 3, 4</sup>

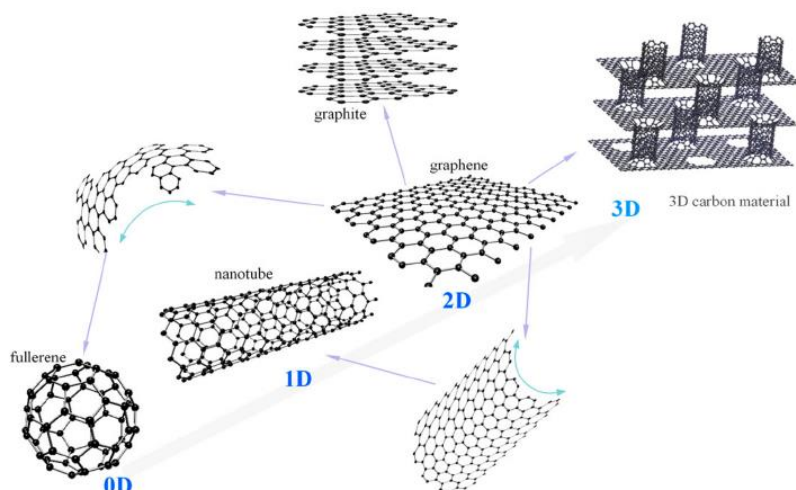


Figure 1. Structures of different carbon allotropes.<sup>3</sup>

Throughout years of intensive research and development, new allotropic forms of carbon emerged.<sup>2, 3</sup> These materials, which revolutionized nanotechnology, are mostly  $sp^2$  bonded with nanoscale dimension. One of the earliest discoveries in the area of carbon nanomaterials was the  $C_{60}$  fullerene<sup>5</sup>, shown in Figure 1, which consists in a cage-like structure of pentagonal and hexagonal faces of carbon atoms.<sup>2, 5</sup>

Following the discovery of fullerenes, a new allotrope was born: carbon nanotubes (CNTs). This type of material was firstly observed by Sumio Iijima in the early 1990s.<sup>6</sup> In short, a carbon nanotube possesses a concentric structure of carbon atoms displayed in hexagonal rings.<sup>3, 4</sup> Another carbon allotrope that emerged in the field was the 2D structure, graphene. Discovered by Geim and Novoselov in 2004<sup>7</sup>, graphene represents the basic structure of the  $sp^2$ -hybridized carbon nanomaterials, as shown in Figure 1. Numerous studies have been developed regarding the synthesis and applications of these new types of carbon nanomaterials.

More recently, at the forefront of carbon nanotechnology, the formation of composite 3D carbon nanomaterials with a well-ordered structure was introduced.<sup>2, 3</sup> A hierarchical structure can be formed with the combination of different carbon allotropes, such as graphene and CNTs (Figure 1). The unique hybrid nanomaterials have gained significant attention due to their interesting features, from remarkable mechanical properties to enhanced electronic and electrocatalytic properties.<sup>3, 8-10</sup> These complex materials must be assembled with efficient and systematic approaches in order to be implemented in advanced applications, such as energy conversion and storage, to be implemented.

### 1.1.1. Carbon Nanotubes

Carbon nanotubes, an artificial carbon allotrope, are composed of a graphene layer rolled into a cylinder shape. Due to their large length-to-diameter ratio, CNTs are typically considered as an one-dimensional nanomaterials.<sup>11</sup> CNTs can be categorized in two different types, based on the number of concentric graphene layers: single-walled carbon nanotubes (SWNTs) and multi-walled carbon nanotubes (MWNTs), as shown in Figure 2.<sup>4, 12</sup>

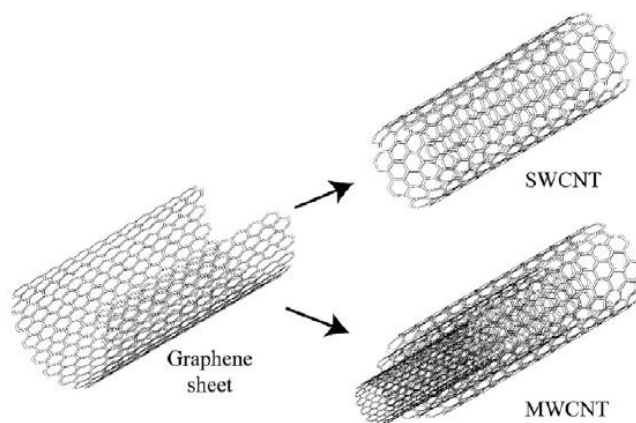


Figure 2. Schematic representation of the single-walled carbon nanotube (SWNTs) and multi-walled carbon nanotube (MWNTs) structures.<sup>12</sup>

The structure of CNTs confers this material unique thermal, electric and mechanical properties (Table 1). With surface modification procedures, the properties of carbon nanotubes can be optimized, or even new properties can be generated.<sup>4, 13</sup> The scope of application of this nanomaterial is vast. CNTs can be implemented in energy-related applications such as super capacitors and solar cells, and even on composite reinforced materials and water treatment filters.<sup>3, 14, 15</sup>

The fabrication method plays a pivotal role on the distribution of lengths and diameters of CNTs and their quality, namely in removal of impurities and the degree of debundling.<sup>16</sup> CNTs can be synthesized through several procedures, such as laser ablation<sup>17</sup>, arc discharge<sup>18</sup> and chemical vapor deposition (CVD).<sup>19</sup> Laser ablation and arc discharge were the pioneering methods for the production of larger quantities of CNTs, in the order of grams.<sup>16</sup> However, chemical vapor deposition is currently the most used one, due to the easy scale-up to higher quantities of CNTs with a high degree of purity. CVD is a simple and cost-effective growing method for CNTs and, compared with the other two, it offers an excellent control over the structure and length of the nanotubes.<sup>4, 16</sup>

### 1.1.2. Graphene

Currently, graphene is one of the most studied nanomaterials.<sup>20</sup> As can be seen in Figure 1, graphene is a 2D carbon structure with  $sp^2$  bonded carbon atoms disposed in a hexagonal lattice. Graphene shows many excellent properties as described in Table 1.<sup>3</sup> Due its high electrical and thermal conductivity and large specific surface area, this nanomaterial can be implemented in various applications such as solar cells, sensors, fuel cells and supercapacitors.<sup>21</sup>

Table 1. Main properties of graphene and CNTs, adapted from ref.<sup>3</sup>

Properties	CNTs	Graphene
Fracture strength / GPa	45	124 (modulus $\approx$ 1100)
Density / $g \cdot cm^{-3}$	1.33	>1
Specific surface area / $m^2 \cdot g^{-1}$	400 (for nanotube "paper")	2630
Thermal conductivity / $W \cdot m^{-1} \cdot K^{-1}$	3000	$\sim$ 5000
Electrical conductivity / $S \cdot cm^{-1}$	5000	$10^6$
Charge mobility / $cm^2 \cdot V^{-1} \cdot s^{-1}$	100000	200000

The first method used to obtain graphene was the Scotch tape method.<sup>21</sup> Briefly, the graphite crystals were exfoliated successively, using adhesive tape, until they reached a monolayer of the material. After the first visualization of graphene, new ways of producing single sheets emerged, which can be divided into top-down and bottom-up methods.<sup>21</sup> The main top-down procedure of graphene growth is the exfoliation of graphite into acid-oxidized graphite (or graphene) oxide (GO) and further chemical reduction of GO. Similar to CNTs, the most used bottom-up growth technique is the chemical vapor deposition. These procedures aim to overcome the main challenge of the mechanically peeled up graphite into graphene, which is the low yield of monolayers obtained.<sup>21, 22</sup> However, CVD is a less viable technique in commercial applications due to the high price and experimental sensitivity demonstrated in graphene production. The properties of graphene are intrinsically related to the strict control of the number of layers, and thus their method of preparation plays a crucial role in the performance of this nanomaterial.<sup>23</sup>

### 1.1.3. Heteroatom-doped Carbon Nanomaterials

Despite demonstrating unique properties, carbon nanomaterials can undergo chemical processes that provide significant optimization on their chemical and physical behavior. Surface modification using elemental doping proves to be an effective methodology to optimize the properties of these nanomaterials.<sup>24, 25</sup>

Usually modification with doping elements is accomplished through covalent bonding between the carbon atoms present in the nanomaterial lattice with periodic table neighboring heteroatoms (e.g.: nitrogen, sulfur, and boron).<sup>25</sup> Heteroatoms possess a larger electronegativity compared to carbon atoms, which confers a polarization effect on the nanomaterial structure. Thus, the material properties, such as magnetic and electronic ones, will be influenced by the induced polarization.<sup>25, 26</sup>

Nitrogen is the most common used heteroatom in the preparation of doped carbon nanomaterials.<sup>27, 28</sup> Compared to the available heteroatoms, nitrogen provides several advantages, namely the fact that it can more easily bond with carbon atoms. Both atoms have similar atomic radius and bond sizes (C–N, 1.41 Å and C–C, 1.41 Å), providing better chemical stability. Furthermore, nitrogen-doped materials are less hazardous.<sup>27, 28</sup>

From a morphological point of view, the insertion of heteroatoms induces effects on the  $\pi$ - $\pi$  coordination present in the  $sp^2$  carbon allotropes. The interferences caused by heteroatoms increases the number of active sites, which promotes charge transfer in carbon nanomaterials.<sup>28</sup> Other effects that can be driven by heteroatoms are the modification of the electronic structure and charge delocalization that can also assist in the evolution of the electrocatalytic performance of CNTs and graphene.<sup>26</sup>

The heteroatom doping can be carried out directly during the synthesis of the carbon nanomaterial, by *in-situ* methods, or through post-treatment doping methods. *In-situ* procedures, CVD, arc-discharge and segregation growth, all offer improved homogeneous doping than post-treatment techniques.<sup>25, 29</sup> Post-treatment doping, on the other hand, has the advantage of doping larger amounts of nanomaterial, and includes thermal or chemical treatment with heteroatom-containing precursors (e.g.: melamine, urea and thiosulfate). Other methods such as micromechanical and plasma treatment can also be classified as post-treatment doping processes.<sup>25, 29</sup>

## 1.2. Transition Metal Dichalcogenides

The discovery of graphene allowed to establish new methodologies that aimed at the production of individual monolayers from different layered materials. Monolayers of these 2D graphene analogs can be obtained through similar approaches as used with graphene, such as CVD and exfoliation.<sup>30</sup> Within this category of graphene-like materials transition metal dichalcogenides (TMDs) stand out as the most important and studied materials.<sup>31, 32</sup>

Generally, TMDs show the generic structure  $\text{MX}_2$ , where M and X correspond, to a transition-metal atom and a chalcogenide atom (such as selenium, sulfur or tellurium), respectively.<sup>31</sup> Typically, a monolayer of TMDs consists of a metal atom sandwiched between two chalcogenide atoms, as depicted in Figure 3 **a**. The M-X bonds have a covalent nature and depending on the configuration of the atomic stacking, the crystalline structure of each layer can be a trigonal prismatic (2H) phase or an octahedral (1T) phase (Figure 3 **b**).<sup>21, 32</sup> These configurations can be converted via intra-layer atomic gliding but, depending on the material, only one configuration is thermodynamically stable. In the example of Figure 3,  $\text{MoS}_2$  (the most studied compound of this class due to its robustness and properties) possesses a trigonal prismatic configuration.<sup>32, 33</sup>

Overall, the crystalline layered material presents weak interlayer interactions (van der Waals forces) which can favor the separation of single layers for further applications.<sup>33</sup> TMDs can be included in nanosensors<sup>34</sup>, as well as in piezoelectric devices<sup>35</sup> and for electrochemical energy storage<sup>36</sup>.

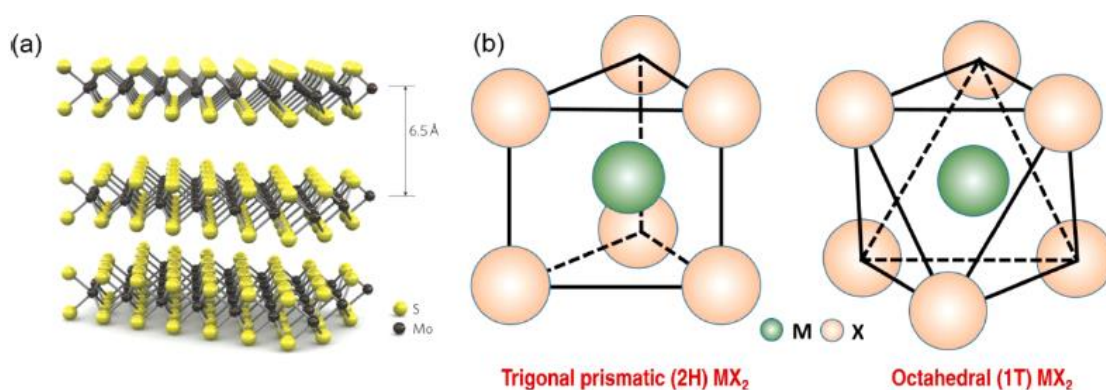


Figure 3. **a** Side view of the molecular structure of  $\text{MoS}_2$ . **b** Schematic representation of unit cell structures of 2H- $\text{MX}_2$  and 1T- $\text{MX}_2$ .<sup>32</sup>

### 1.3. Hybrid Nanocomposites

Commonly, nanocomposites are defined as hierarchical structures consisting of two, or more, materials, one of which has a dimensionality on the order of nanometers.<sup>37</sup> The building blocks, must have different morphologies, with one being the matrix of the structure and the other playing the role of the filler(s) (component(s) to be dispersed).<sup>37</sup>,<sup>38</sup> The aim of nanocomposites fabrication is to obtain enhanced or synergistic effects of properties or obtain new unique properties, resulting from the combination of the building blocks.<sup>38</sup>

Recently, the fabrication of nanocomposites based on carbon nanomaterials as building blocks has become an intensive area of research.<sup>2</sup> For example, within the nanomaterials presented above, there is the possibility to develop nanocomposites consisting of fullerene and CNTs (0D/1D)<sup>38</sup> or graphene (0D/2D)<sup>39</sup> and CNTs with graphene (1D/2D)<sup>40, 41</sup>. Particularly, there has been a growing interest in the assembly of nanocomposites composed by CNTs and graphene.<sup>40, 42</sup> As mentioned in Section 1.1, the  $sp^2$  allotropes of carbon exhibit delocalized  $\pi$ -electrons, which provides robust  $\pi - \pi$  interactions. The same interactions may induce an increase in electrical conductivity and tensile strength on the hybrid material.<sup>42</sup> Carbon nanocomposites are ideal candidates in applications involving electrochemical energy storage<sup>37</sup> and strain sensors<sup>40</sup>.

The combination of carbon materials with TMDs can also be highlighted in the context of the design and building of complex hierarchical structures. TMDs can be combined not only with graphene sheets (vdW heterostructures), but also with CNTs<sup>43</sup> and even with CNTs/graphene nanocomposites.<sup>44-46</sup> TMD-containing hybrid nanomaterials may prove attractive given the weak results that pristine TMDs exhibit in electrochemical assays, namely due to undesirable sheet restacking and limited electron (or ion) transport.<sup>47</sup> Therefore, the carbon materials are meant to play the role of matrix in the hybrid structure, obstructing possible aggregation of the planar sheets of TMDs. The increased spacing between layers will then induce an increase in the number of active sites present in the nanocomposite.<sup>44, 45</sup> Compared to TMDs, TMDs/carbon nanomaterials structures exhibit superior electron transport and diffusion and significant electrocatalytic stability.<sup>44, 47</sup> Given the number of advantages presented, TMD/carbon nanocomposites are important candidates for applications involving electrocatalytic energy conversion and storage, as described in section 1.5.3.

Despite their attractive advantages and applicability, the synthesis of these nanocomposites is a major challenge. Typically, nanocomposites are fabricated through procedures performed under extreme experimental conditions and with hazardous precursors, such as solvothermal methodologies.<sup>45, 48</sup> Furthermore, the nature of carbon

nanomaterials (and TMDs) is not convenient for practical use, due to the undesirable aggregation and agglomeration.<sup>49</sup> Thus, the formation of more complex structures requires functionalization of the surfaces of these nanomaterials so that proper interactions leading to assembly may occur.<sup>4</sup>

### 1.3.1. Van der Waals heterostructures

2D nanomaterials exhibit optimized and, often, novel properties compared to the bulk counterparts, such as improved electromagnetic properties and strong interactions with light.<sup>50, 51</sup> These properties are the product of the two-dimensional structure, since the absence of dangling bonds on the surface and the quantum confinement that they display enable strong in-plane stability and unique electronic and optical characteristics.<sup>52</sup>

2D nanomaterials paved the way for the development of even more complex 2D structures, typically designated as van der Waals heterostructures.<sup>53</sup> vdW heterostructures consist of two or more types of layered materials designed to confer different properties to a single material.<sup>54</sup> Several kinds of heterostructures were already studied, such as the combination between different types of TMDs<sup>55, 56</sup> (e.g. MoS<sub>2</sub> and WS<sub>2</sub>), graphene and TMDs<sup>57, 58</sup> and hexagonal boron nitride (h-BN) with graphene<sup>59</sup> and TMDs<sup>60</sup>.

Taking into account the nature of these materials, the principle of assembly is the opposite of the process of separating layers on the bulk by exfoliation.<sup>52</sup> The construction of heterostructures is based on the vertical stacking of different sheets, as illustrated in Figure 4.<sup>53</sup> As the inter-layer interaction is weak (vdW interactions), it allows the organization of several components without restrictions in the assembly process. Thus, it becomes feasible to synthesize a heterostructure with a vertical arrangement without the presence of divergences arising from the packing of materials with different crystal lattices.<sup>53, 54, 61</sup> Furthermore, 2D vdW heterostructures present a high anisotropy between the in-plane and out-of-plane directions.<sup>61</sup>

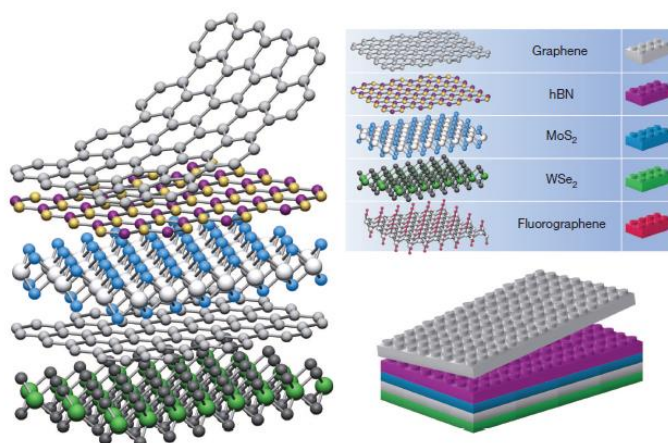


Figure 4. Schematic representation of the assembly of a vdW heterostructure and analogy of 2D graphene, TMDs, h-BN and fluorographene crystals to Lego pieces.<sup>53</sup>

Among myriad 2D materials, the heterostructures composed by graphene and TMDs are by far the most studied.<sup>57, 58, 62</sup> For instance in energy storage applications, when TMDs are present in 2D form they have a low capacitance retention, which can lead to difficulties in achieving desirable performances.<sup>33</sup> Thus, a solution to overcome this problem is based on the rigorous combination with TMDs that have different energy bands.<sup>55</sup> However, although the conjugation between different TMDs is advantageous compared to the singular components, TMD/graphene heterostructures exhibit more promising results,<sup>52</sup> especially, in certain applications, where synergistic effects occur.<sup>57, 63</sup>

Due to the innumerable possible combinations of 2D materials and their versatility, vdW structures can be implemented in a variety of applications and devices, with focus in energy conversion and storage related fields, such as supercapacitors<sup>64</sup>, lithium ion batteries<sup>63</sup> and as electrocatalysts for the hydrogen evolution reaction (HER)<sup>65</sup>.

#### 1.3.1.1. Assembly Methods

The production of vdW heterostructures is a recent topic, and the elaboration of reproducible experimental procedures requires prior precautions. As the crystal quality of singular 2D nanomaterials can vary according to the production techniques, the heterostructure is also strongly dependent on the respective qualities of the components.<sup>50, 53</sup>

To overcome problems such as the presence of undesirable stacks between layers and contaminants, rigorous procedures have been developed to obtain these nanomaterials. The main assembly methods are based on those for obtaining single 2D

materials, namely the production through CVD, microexfoliation of layers and other techniques, such as hydrothermal methods and solution processing.<sup>52, 61</sup>

As described in the previous sections, the CVD technique consists on the sequential deposition of monolayers (or few layers) of different 2D materials on a substrate.<sup>58</sup> The deposition takes place following the decomposition of precursors at high temperatures, thus leading to better control of the growth of 2D crystals with good quality.<sup>66</sup>

The assembly from the exfoliation of the starting materials follows the same principle as the mechanical fragmentation techniques of graphene and TMDs. With the aid of adhesive tape, the 2D sheets are separated from the bulk and then deposited on a substrate.<sup>67</sup> However, the shortcomings of this process reside in the manual work required, as the operator plays a crucial role in the quality of the material. It should be noted that this method is time-consuming and quite vulnerable to contamination.<sup>52, 67</sup>

The assembly of 2D heterostructures according to hydrothermal (or solvothermal) methods is carried out in extreme conditions, with high temperatures and pressures. In a typical procedure, a mixture of chemical precursors is deposited in a reactor where the reaction takes place at elevated temperatures, in an oven.<sup>57</sup> After the reaction between the materials takes place, the mixture is removed from the oven and cooled to room temperature. Finally, the solution is filtered, and the process ends with drying of the newly formed heterostructure.<sup>62</sup> Compared to the previously exposed techniques, the hydrothermal assembly method proves to be practical and quick to perform. However, even with high yields, there are still obstacles to be overcome, such as the production of harmful by-products.<sup>57, 62</sup>

In order to achieve a practical and fast methodology with mild experimental conditions, the method of assembly through dispersion-processing has emerged as an interesting alternative.<sup>68</sup> As can be seen in Figure 5, the individual dispersions of TMD and graphene are mixed into a single dispersion, which can lead to self-assembly processes with a defined organization.<sup>52</sup> The dispersions of the starting materials can be prepared by liquid phase exfoliation or electrochemical intercalation. Exfoliation in the liquid phase is carried out using ultrasonic waves, where cavitation bubbles are produced. The impact of bubbles on the material offers a separation of individual sheets.<sup>61</sup> On the other hand, electrochemical intercalation uses ionic species as inter-layer separators, thus inducing greater spacing between the nanosheets.<sup>68</sup> Given the desired proportions, the heterostructure is achieved after solvent removal and drying.

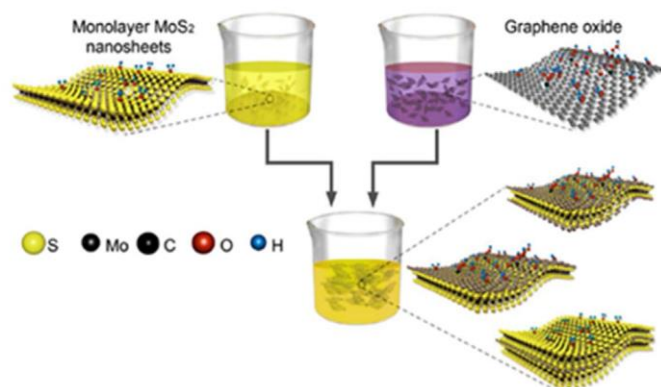


Figure 5. Schematic representation of an assembly method between graphene oxide and single-layer MoS<sub>2</sub> based on dispersion-processing. Adapted from ref.<sup>52</sup>

Overall, hydrothermal and dispersion-processing methods enable the fabrication of vdW heterostructures with stronger coupling between the two nanomaterials and high volumes of dispersed monolayers. Furthermore, these techniques are cost-effective and have good yields, and can be implemented in scale-up processes.<sup>61, 68</sup>

#### 1.4. Dispersion and Functionalization of Nanomaterials

Given the hydrophobic properties of carbon nanomaterials, surface modification is required for dispersion in aqueous medium. However, carbon nanomaterials can be wetted in organic solvents.<sup>22</sup> Although the dispersibility in organic solvents (e.g. dimethyl acetamide (DMA) and dimethylformamide (DMF)) aids in the separation of the aggregated material, this method can induce structural problems in the final nanomaterial.<sup>22, 69</sup>

To circumvent this issue, nanomaterials can be modified by functionalization procedures to improve solvent compatibility and reduce cluster aggregation. Functionalization of carbon materials can be divided into two main categories: i) chemical (covalent functionalization) and ii) physical (non-covalent functionalization).<sup>69</sup>

- Covalent functionalization

Covalent functionalization typically consists of the covalent linking of hydrophilic functional groups to the surface of the nanomaterial or to its terminal regions. Before the binding of functional groups, the material can be oxidized, which introduces defects on the surface (e.g. in carbon nanotubes and graphene).<sup>22, 70</sup> The oxidized carbon nanomaterials are then subject to chemical modifications with functional groups (e.g. thiol and amine groups).<sup>71</sup>

However, since the oxidation process uses strong acids (e.g. nitric acid and sulfuric acid), the generation of significant defects and damage of the graphitic structure can occur, which is negatively reflected in the electronic properties, namely by decreasing the electrical conductivity.<sup>69, 72</sup>

- Non-covalent functionalization

An alternative to the chemical modification of nanomaterials, like CNTs and graphene, is the non-covalent functionalization, which is a simpler and more practical procedure. The non-covalent functionalization process takes advantage of amphiphilic molecules such as surfactants, polymers, peptides, and nucleic acids.<sup>70, 71</sup> The main interactions are hydrophobic ones, occurring between the nonpolar nanomaterial and the nonpolar moieties of the amphiphilic molecules. Furthermore, delocalized  $\pi$ -electrons present in carbon nanomaterials can also promote the adsorption process on the respective surface.<sup>71</sup> Therefore, overall, the amphiphilic compounds may interact with the surface of nanomaterials through hydrophobic interactions, vdW forces,  $\pi$ - $\pi$  interactions or even electrostatic interactions.<sup>70</sup> Another advantage that non-covalent functionalization shows is the conservation of the nanomaterials properties. As there is no change in the  $sp_2$  structure in the case of carbon nanomaterials, the properties will also remain unchanged, which proves to be useful in the production of nanocomposites.<sup>22, 71</sup>

#### 1.4.1. Mechanical Dispersion Processes

Experimentally, the adsorption of amphiphilic molecules, such as surfactant and polymers, in the nanomaterial surface can be promoted by mechanical dispersion processes, such as high shear process (e.g., ball milling), or ultrasonication.<sup>4, 73</sup>

The dispersibility of carbon nanomaterials in water by non-covalent methods has been extensively studied.<sup>4, 74-77</sup> The mechanical exfoliation via ultrasonication of the CNT aggregates (or the graphene layers) is thought to occur via the mechanism depicted in Figure 6.<sup>4</sup> The process consists in the rupture of the vdW forces binding the nanotubes or graphene layers by supplying energy from the ultrasonic device.<sup>78</sup> The energy is transferred by ultrasonic waves that propagate in the aqueous medium. During this process, compression and expansion disturbances occur in the medium.<sup>79</sup> Consequently, the gradient movements generate bubbles (cavitation bubbles) that will be central in separating the singular components from the agglomerates. Successively, the bubble implodes, and high temperature and pressure generation occurs, favoring the release and collision of shock waves in the clusters, which will cause the exposure of previously hidden interior zones in the cluster.<sup>73, 79</sup>

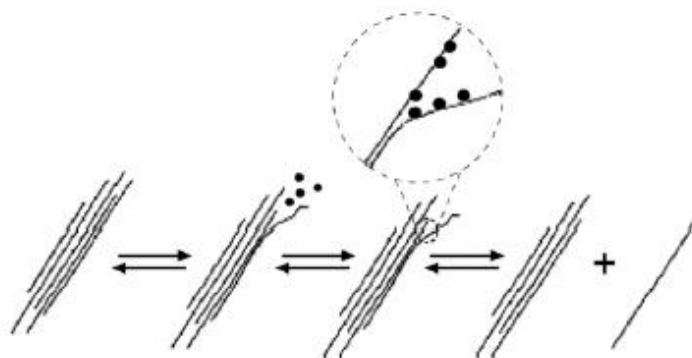


Figure 6. Sequential steps of the CNTs isolation process through sonication and surfactant functionalization, lines – CNTs, dots – dispersant agent.<sup>4</sup>

The dispersing agents will occupy the newly exposed regions, leading to the separation of the nanomaterials in the dispersion and preventing restacking of the isolated nanotubes, or in the case of graphene, of the two-dimensional layers.<sup>73</sup>

On the other hand, functionalization and disaggregation of clusters by ball milling also proves to be an affordable approach. The exfoliation of nanomaterials is dependent on the mechanical energy from the impact of balls (made of e.g. stainless steel or zirconium) on the respective material.<sup>80</sup> In a regulated and constant method, the stress induced by the impacts and friction of the balls causes the clusters to fragment.<sup>81</sup> For example, in the case of graphene, the imparted energy enables the fragmentation of the vdW forces between the different layers.<sup>82</sup> Like with ultrasound, after the aggregates have been reduced, the functionalization process is simplified by the exposure of new areas.<sup>81</sup>

For both processes, there is a need to carefully plan the experimental parameters, since the high energies involved can lead to breakage and defect formation in the lattice of the nanomaterials.<sup>73, 80</sup>

#### 1.4.2. Dispersant Agents

Amphiphilic molecules, such as surfactants and polymers, enable modification of the surface properties of various nanomaterials.<sup>76</sup> The colloidal stability present in dispersions is dependent on the electrostatic or steric repulsions induced by the adsorbed dispersing agents.<sup>77, 83</sup>

- Surfactants

Surfactants are molecules that contain two segments, the polar zone (headgroup), where the water soluble component is found (hydrophilic) and the nonpolar zone (tail) which exhibits hydrophobic behavior.<sup>84</sup> Due to this dualism, surfactants show two effects: i) adsorption and ii) self-assembly. Unimers, free surfactant molecules, tend to

adsorb onto the surface of the aqueous medium and form aggregates (micelles) in aqueous solutions.<sup>83</sup> Surfactants have a tendency of adsorption at the surface of a liquid by the polar heads. As the tails are hydrophobic, they are directed to the gas phase, thus promoting the reduction of surface tension.<sup>84</sup> On the other hand, self-assembly starts when the surfactant concentration present in the medium is higher than the critical micellar concentration (*cmc*), the minimum surfactant concentration above which micelles originate. Another factor that is related to micelle formation is the Krafft temperature ( $T_{Kr}$ ), which corresponds to the minimum temperature for the formation of these aggregates.<sup>83, 84</sup>

Within the wide range of available surfactants, a common classification is according to their charge. Therefore, surfactants can be classified as ionic (anionic and cationic), non-ionic and zwitterionic (surfactants with having both an anionic and a cationic region and hence overall neutral).<sup>83</sup> For hydrophobic surfaces, surfactants with a larger hydrocarbon chain display a greater adsorption tendency.<sup>74</sup> In the preparation of nanocomposites, surfactants will interact with the materials surfaces and interfacial regions between different materials. The adsorption of the surfactants will allow the conservation of the intrinsic properties and an optimization of the interactions between the different nanomaterials, in less restrictive and harmful conditions.<sup>85</sup>

- Polymers and polyelectrolytes:

Compared to surfactants, polymers have larger dimensions. Through polymerization processes, the monomers (basic units) link together to form the macromolecule.<sup>84</sup> Depending on the bonding method, polymers can exhibit linear, cross-linked, and branched structures. With respect to their ability as dispersing agents for nanomaterials, more specifically regarding carbon nanotubes, one of the proposed adsorption models in the dispersion of CNTs in aqueous solutions suggests that the polymers "wrap" around the nanotubes. Since polymers are macromolecules, the adsorbed region will be larger compared to the adsorbed area of a surfactant unimer.<sup>84</sup> After the "wrapping" by the polymer, the decorated CNTs will repel each other through steric repulsions preventing reaggregation. Another model considers a more random adsorption of the polymer on the CNTs surface, whereby the polymer chains still retain considerable lateral mobility.<sup>86</sup> This seems to be the case, in particular, of block copolymer such as Pluronic F127.

Recently, the combination of ionic surfactants with polymers has been addressed.<sup>87</sup> The combination between these two types of amphiphilic molecules can lead to synergism in the dispersion power of nanomaterials. The surfactant/polymer mixture can exhibit characteristics similar to polyelectrolytes.<sup>88</sup> Briefly, polyelectrolytes have a polymer backbone with a sequential distribution of charged functional groups (such as

quaternary ammonium or carboxylates). By coating ionic surfactants on the hydrocarbonated chains, the molecule will extend due to the repulsions between the ionic groups. Ultimately, higher surface adsorption will occur, promoting individualization of the carbon material.<sup>84, 88</sup>

## 1.5. Electrochemical-related Technologies

Electrocatalytic energy-related technologies are among the possible applications that carbon nanomaterials and TMDs can find.<sup>21</sup>

Given the energy-related concerns experienced in recent years, such as the growing energy supply demand and the environmental pollution associated with the fossil fuel derived energy, there has been an intensive research for less harmful and sustainable energetic alternatives.<sup>89</sup> The development of renewable energy conversion and storage technologies has gained significant interest in this demand. Among the applications where electrochemical processes can be employed, electrocatalytic energy conversion (e.g. fuel cells) and storage (e.g. metal-air batteries) devices stand out.<sup>90, 91</sup>

### 1.5.1. Metal-Air Batteries and Fuel Cells

- Metal-Air Batteries

As shown in Figure 7, metal-air batteries are electrochemical devices composed by an electrolyte, a metal anode and an air cathode, in which the active oxygen is accessed from the environment. A gas diffusion layer is used to allow O<sub>2</sub> diffusion through without interference from other gases. The metal anode can be composed by different metals, such as aluminum, lithium and zinc.<sup>90, 92</sup> The performance of the metal-air batteries is driven by the metal oxidation/reduction and by the electrocatalytic oxygen reactions.<sup>90</sup>

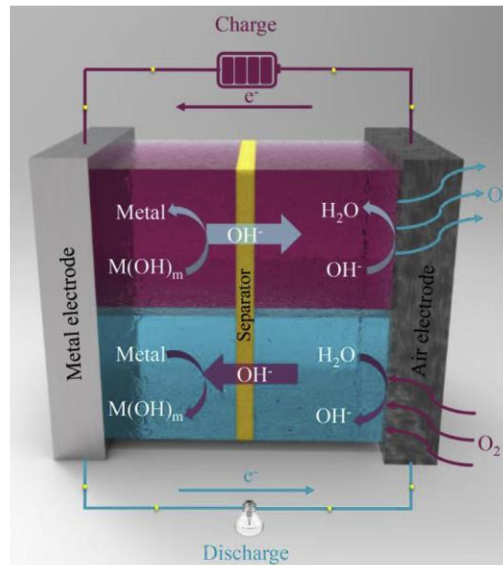
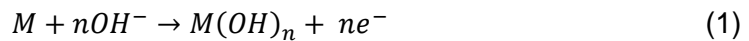
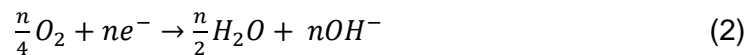


Figure 7. Illustration of a metal-air battery and its operation mode.<sup>92</sup>

The process begins with the diffusion of  $O_2$  into the electrolyte. During the discharge, the metal electrode is oxidized, releasing electrons. The oxidized metal ions react with the hydroxide groups, from the electrolyte to produce the metal hydroxide, according to equation (1)<sup>92</sup> ( $n$  corresponds to the valence number of the metal ion).



Then, the newly formed electrons are conducted to the air electrode and reacts with the  $O_2$  molecules to produce water, hydroxide ions and electrical energy (equation (2)).<sup>90, 92</sup>



The formation of  $OH^-$ , by equation (2) enables a new cycle to be repeated. The discharge and charge processes involved in the overall process are dependent, respectively, on the oxygen reduction reaction (ORR) and the oxygen evolution reaction (OER), whereby these reactions are critical for the device performance.<sup>91</sup>

- Fuel cells

Fuel cells are also an important target of study in the development of energy conversion technologies based on electrochemical processes.<sup>93</sup> Besides being sustainable, this technology is environmental friendly and exhibits high efficiency, making it very attractive. For example, in fuel cells that use hydrogen as fuel, the procedure consists on the  $H_2$  oxidation (hydrogen oxidation reaction, HOR) at the anode and simultaneous  $O_2$  reduction (oxygen reduction reaction, ORR) at the cathode, with production of electrical energy and water, as can be seen in Figure 8, right side.<sup>94</sup> This

application exhibits significant advantages, among them the inexistence of harmful anthropogenic gas emissions.<sup>95</sup>

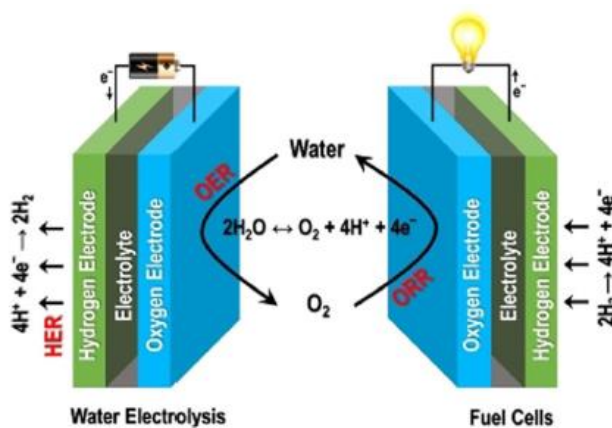
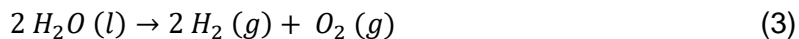


Figure 8. Illustration of a fuel cell (right), combined with an electrolyzer (left) and their operational scheme.

As shown in Figure 8, left side, an electrolytic cell can play the role of providing fuel (hydrogen) to the cell through the water splitting process.<sup>94</sup> This process is based on the hydrogen evolution reaction (HER), carried out at the cathode component of the electrolytic cell, and in the oxygen evolution reaction (OER) that takes place at the anode. The main products of the reaction correspond to  $H_2$  (the fuel) and  $O_2$ , as seen in equation (3).<sup>91, 94</sup>



When the electrolyzer is combined with the fuel cell in a single device, the generated  $H_2$  is subsequently oxidized and electrical energy can be continuously produced in the continuation of the electrochemical cycle.<sup>21</sup> Overall, the operation of these combined devices is highly based in the water cycle.<sup>21, 91, 94</sup> In particular, the oxygen reactions, OER and ORR, have a crucial role in the performance of the device.

### 1.5.2. Oxygen Reactions

The operation mechanism of the energy-related technologies presented above are highly dependent on the OER and ORR.<sup>92, 93</sup> Nonetheless, the kinetics of these reactions are very slow, and hence the performance of the devices may be compromised.<sup>21, 93</sup> A convenient solution to overcome this drawback is the use of electrocatalysts, i.e. catalysts that act on the electrode surface (or can even be the surface itself) in an electrochemical process.<sup>96, 97</sup>

Overall, ORR and OER are complex reactions, that involve several stages of adsorption/desorption of intermediated oxygen-rich chemical species (e.g. O\*, OH\* and OOH\*) at the electrocatalyst surface.<sup>98</sup>

- Electrocatalytic Oxygen Reduction Reaction

As shown in Table 1, in aqueous electrolytes (acidic or alkaline), ORR can occur in two distinct pathways: a direct and an indirect route.<sup>99</sup>

In the direct four-electron (4e<sup>-</sup>) pathway, O<sub>2</sub> is directly reduced to water (in acidic electrolytes) or hydroxyl groups in alkaline electrolytes. On the other hand, the indirect two-electron (2e<sup>-</sup>) pathway consists on the reduction of O<sub>2</sub> following two intermediated steps: in alkaline electrolytes, HO<sub>2</sub><sup>-</sup> is formed as an intermediate, while in acid electrolytes H<sub>2</sub>O<sub>2</sub> is generated as an intermediate and then subsequently reduced to water.<sup>3, 21, 94</sup>

Table 2. Reaction pathways of ORR in aqueous electrolytes, with the respective potentials (vs.RHE).<sup>94</sup>

Electrolyte	Reaction pathway
Alkaline	<u>4-electron pathway:</u>
	$O_2 + 4 e^- + 2H_2O \rightarrow 4 OH^- (E^0 = 0.401 V)$
	<u>2-electron pathway:</u>
	$O_2 + H_2O + 2 e^- \rightarrow HO_2^- + OH^- (E^0 = -0.605 V)$ $HO_2^- + H_2O + 2 e^- \rightarrow 3 OH^- (E^0 = 0.867 V)$
Acid	<u>4-electron pathway:</u>
	$O_2 + 4 e^- + 4 H^+ \rightarrow 2 H_2O (E^0 = 1.229 V)$
	<u>2-electron pathway:</u>
	$O_2 + 2 H^+ + 2 e^- \rightarrow H_2O_2 (E^0 = 0.695 V)$ $H_2O_2 + 2 H^+ + 2 e^- \rightarrow 2 H_2O (E^0 = 1.763 V)$

As can be seen in Table 2, after the adsorption of O<sub>2</sub> molecules, it is necessary to break the O=O bond for the reaction to start. From a molecular perspective, the bond is strong, possessing a binding energy of 498 kJ·mol<sup>-1</sup>.<sup>100, 101</sup> To overcome this barrier, high reduction potentials are applied; however, the potentials provided induce negative

effects on the devices. Decreased electrochemical performance is one of the most common problems observed.<sup>100</sup>

The redox behavior of the electrocatalysts can be analyzed by cyclic voltammetry (CV). To assess the performance of different electrocatalysts, it is crucial to analyze their kinetic electrocatalytic parameters. For this purpose, the parameters can be obtained directly, or according to supplementary equations, from linear sweep voltammetry (LSV) curves.<sup>101</sup>

With the performed tests, the electrocatalytic performance of the materials is measured. Typically, in ORR, the indicators used are: i) the onset potential ( $E_{\text{onset}}$ ); ii) the diffusion-limited current density ( $j_L$ ) and kinetic current density ( $j_k$ ); iii) the Tafel slope (TS) and iv) the number of electrons transferred per  $O_2$  molecule ( $n_{O_2}$ ).<sup>100, 101</sup> The  $E_{\text{onset}}$  can be defined as the potential where ORR starts.<sup>100</sup> When the reaction at the electrode reaches a state where it is fully controlled by mass transport, the current densities are designated diffusion-limited current densities (i.e. typically a plateau profile is obtained and  $j = j_L$ ).<sup>101</sup> The kinetic current density ( $j_k$ ) designates the current density when it has no mass-transfer limitations. The Tafel slope (TS) correlates with the electrocatalytic process that the electrocatalyst has undergone and the rate-determining step. TS can be calculated by plotting the overpotential  $\eta$  vs.  $\log j$  and according to the Tafel equation (Equation (4)) the value of TS is given:

$$\eta = a + b \log(j) \quad (4)$$

where the slope  $b$  is the TS.<sup>94, 100</sup> The overpotential is the difference between the theoretically applied potential and the experimentally observed potential.<sup>94</sup> Lastly, the number of electrons transferred per  $O_2$  molecule ( $n_{O_2}$ ) bring information about the selectivity of the electrocatalyst for the possible reduction pathways,  $2e^-$  or  $4e^-$ .<sup>93</sup>

Given the electrocatalytic parameters, a good ORR electrocatalyst should present more positive  $E_{\text{onset}}$  values, low TS values and selectivity for the reduction by the  $4e^-$  pathway.<sup>99</sup> Although the  $4e^-$  pathway is the most desirable one, in terms of a fuel cell application, electrocatalysts that are selective for the  $2e^-$  pathway can be useful for  $H_2O_2$  production. High long-term electrochemical stability and tolerance to fuel crossover (e.g., methanol) are also relevant properties that ORR electrocatalysts must demonstrate.<sup>21, 94</sup>

- Electrocatalytic Oxygen Evolution Reaction

OER can be seen as the reverse reaction of ORR. In this case, the oxidation of water occurs, thus producing  $O_2$ . As with ORR, OER can be performed on alkaline or acidic electrolytes.<sup>101</sup> As can be seen in Table 3, in alkaline electrolytes four hydroxide ions undergo oxidation forming one oxygen molecule. In acid electrolytes, two molecules of  $H_2O$  are oxidized into an  $O_2$  molecule.<sup>94</sup>

Table 3. Reaction pathways of OER in aqueous electrolytes.<sup>94</sup>

Electrolyte	Reaction pathway
Alkaline	$4 \text{ OH}^- \rightarrow 2 \text{ H}_2\text{O} + \text{ O}_2 + 4 \text{ e}^-$
Acid	$2 \text{ H}_2\text{O} \rightarrow 4 \text{ H}^+ + \text{ O}_2 + 4 \text{ e}^-$

The electrocatalytic OER evaluation is based on the study of parameters such as the Tafel slope, overpotential ( $\eta$ ) and exchange current density ( $j_0$ ).<sup>102</sup> In OER benchmarking,  $\eta$  must reach significant values when  $j = 10 \text{ mA}\cdot\text{cm}^{-2}$ , since this current density value corresponds to the 12.3 % efficiency observed in other photoelectrochemical water splitting applications.<sup>94, 101</sup> Exchange current density ( $j_0$ ) can be obtained when  $\eta = 0$  and represents the intrinsic electrocatalytic activity of the electrocatalyst at equilibrium conditions.<sup>98</sup> Desirably, an OER electrocatalyst should exhibit high values of  $j_0$  and low values of TS and  $\eta$ .<sup>94, 98</sup>

### 1.5.3. Benchmarking Electrocatalysts and Novel Electrocatalysts

The design of electrocatalysts for oxygen reactions is an elaborate task. For ORR, platinum nanoparticles supported on carbon black, specifically Vulcan, are used as the benchmark electrocatalyst (known as the Pt/C electrocatalyst).<sup>97</sup> However, despite providing high current densities and selectivity for the  $4\text{e}^-$  pathway, Pt/C lacks methanol crossover resistance and significant long-term electrochemical stability.<sup>96, 97</sup> In OER, the electrocatalysts used as benchmark are Iridium (IV) oxide ( $\text{IrO}_2$ ) and Ruthenium (IV) oxide ( $\text{RuO}_2$ ), due to their efficiency for the oxidation of  $\text{O}_2$ .<sup>102</sup> Overall, Pt/C,  $\text{IrO}_2$  and  $\text{RuO}_2$  electrocatalysts present a set of problems that makes their implementation in fuel cells, electrolyzers, and metal-air batteries, rather arduous. These electrocatalysts are known for their high price, scarcity, low stability and low activity towards the reverse reaction (e.g. Pt/C is not effective for OER), making them economically unfeasible.<sup>91, 93,</sup>

100

Given the major problems with state-of-the-art electrocatalysts, studies on the production of viable and sustainable electrocatalysts have emerged.<sup>99</sup> The development of alternative electrocatalysts must follow a practical and cost-effective procedure with earth abundant materials.<sup>95, 96</sup> Furthermore, the novel electrocatalysts can simultaneously behave as both ORR and OER electrocatalysts, thus classifying them as bifunctional electrocatalysts.<sup>96</sup>

Among the varied categories, the most relevant ORR and/or OER electrocatalysts reported are spinel compounds<sup>96, 97</sup> (class of metal oxides with an  $AB_2X_4$  formulation, e.g.  $Co_3O_4$  and  $Mn_3O_4$ ), metal organic frameworks<sup>94, 103</sup> (MOFs), polyoxometalates<sup>104, 105</sup> (POMs) and carbon nanomaterials.

As mentioned in sections 1.1 and 1.3, carbon nanomaterials and their nanocomposites exhibit appealing properties in the context of electrocatalytic applications. CNTs and graphene doped with heteroatoms such as nitrogen<sup>106-110</sup> and boron<sup>111, 112</sup> are good examples of good electrocatalysts for oxygen reactions. Among the various carbon materials, the use of heteroatom doped graphite<sup>113</sup>, doped carbon quantum-dots<sup>114, 115</sup>, carbon-nitride-based materials<sup>116</sup> and CNTs/graphene nanocomposites<sup>117-119</sup> are also prominent.

It is relevant to note that pristine TMDs are not commonly used in ORR/OER electrochemical studies. However, when they are combined with carbon nanomaterials, these structures become potential electrocatalysts.<sup>43, 120-122</sup>

## 1.6. Scope of this Work

The current work aimed at the development of nanocomposites through a ternary combination of 1D and 2D nanomaterials (carbon nanotubes, graphene and  $MoS_2$ ), and their respective electrocatalytic evaluation for ORR and OER. Previous work in our group by Ferreira *et al.* already showed the potential of using nanocomposites that combined  $MoS_2$  and MWNTs as electrocatalysts in the same type of oxygen reactions.<sup>85</sup> Our intention herein was to further develop these studies into more complex types of nanocomposites, looking for possible enhanced performance.

To this end, 2D nanocomposites of  $MoS_2$  and graphene nanoplatelets (GnPs) – ( $MoS_2@GnP$ ) – and their nanocomposites with multiwalled carbon nanotubes (MWNTs) – ( $MoS_2@GnP$ )@MWNT – were developed via physical functionalization. The structure of the 3D nanocomposites is based on a matrix composed of a rigorous mixture of GnPs and  $MoS_2$ , with the MWNTs lying between the various layers of the  $MoS_2@GnP$  heterostructure.

For the preparation of the hybrid materials two methodologies were adopted: (i) the surfactant-assisted liquid phase exfoliation (SALPE) and (ii) the mechanical exfoliation through ball milling. It is relevant to note that compared with the current literature, this work can be seen as a step forward, since the non-covalent functionalization using mild experimental conditions, employed for the production of the 3D nanocomposites, has not been much explored.

Furthermore, the prepared nanocomposites were morphologically and structurally characterized by scanning electron microscopy (SEM) and powder X-ray diffraction (PXRD). Their electrocatalytic activities for ORR and OER were evaluated by cyclic voltammetry, linear sweep voltammetry, and chronoamperometry assays, and tentatively correlated with their structural characteristics.

In the next sections of this dissertation, the experimental details related with the preparation, characterization and electrocatalytic application of the 2D and 3D nanocomposites are presented, as well as the main results obtained. Finally, the main conclusions of the performed work are highlighted, and some perspectives of future work are put forth.

# **Chapter 2**

## *Experimental Section*

## 2. Experimental Section

This chapter is divided into four sections where the materials and experimental conditions used will be detailed. The set of methodologies employed in the preparation of the different nanocomposites and the description of the characterization techniques will also be presented. Finally, the description of the experimental electrochemical studies will be given.

### 2.1. Materials, reagents and solvents

The compounds sodium cholate (SC, Sigma-Aldrich, > 99%), Triton<sup>TM</sup> X-100 (TX-100, Sigma-Aldrich, laboratory grade), cetyltrimethylammonium bromide (CTAB, Sigma-Aldrich, > 99%) and polyvinylpyrrolidone (PVP, Sigma-Aldrich, > 95%) were selected for the non-covalent functionalization of carbon nanomaterials and MoS<sub>2</sub>. These compounds were used as received.

The carbon materials (MWNTs and GnPs) and MoS<sub>2</sub> were also used as received. MWNTs (diameter = 8-15 nm and length = 10-50 μm) were purchased from Cheaptubes<sup>®</sup> with a purity grade > 95%. GnPs (Grade M-5) were purchased from XG<sup>®</sup>Sciences, with an oxygen content less than 1% and acid residues less than 0.5 wt%. MoS<sub>2</sub> was purchased from Sigma-Aldrich with a purity grade > 99%. For the nitrogen doping of GnPs, melamine (Alfa Aesar, 99 %) was used as received.

For the electrocatalytic studies, potassium hydroxide (KOH, Sigma-Aldrich, > 99.99 %), 2-propanol (Aldrich, 99.5 %), Nafion (Aldrich, 5 wt% in a mixture of lower aliphatic alcohols and water solution), methanol (VWR, anhydrous, maximum 0.002 % of H<sub>2</sub>O), Ruthenium(IV) oxide (RuO<sub>2</sub>, Aldrich, 99,9 %) and 20 wt.% Pt/C (HiSPEC<sup>®</sup> 3000, Alfa Aesar) were used as received. All solutions and dispersions were prepared using ultrapure water (Interface system, electrical resistivity 18.2 MΩ cm at 25 °C).

### 2.2. Nanocomposites Preparation

The preparation of the 2D MoS<sub>2</sub>@GnP and 3D (MoS<sub>2</sub>@GnP)@MWNT hybrid materials was based in surfactant-assisted liquid phase exfoliation (SALPE) and micromechanical exfoliation approaches, exploring several experimental procedures. These are designated as: (i) one-step dispersion method, (ii) two-step dispersion method and (iii) ball milling (Figure 9). In the one-step dispersion and ball milling procedures, two secondary methodologies were explored, according to the addition of surfactant during the preparation step of the 2D nanocomposite.

In all procedures, the prepared dispersions were tip-sonicated using a Sonics VC 505 ultrasonic homogenizer (500 W output power; 20 kHz processing frequency) with a 13 mm tip. The power transferred to the system was controlled and estimated by a calorimetric method, to maintain constant the experimental conditions of the sonication process and to ensure reproducible and repeatable procedures. Thus, the energy transferred by tip sonication to each dispersion containing GnPs and MoS<sub>2</sub> was fixed at 0.80 kJ·mg<sup>-1</sup>, using a vibration amplitude of 50 %. Given that the MWNTs could rupture at high energy densities, the energy transferred for the MWNTs dispersions and the mixed dispersions (which contained MoS<sub>2</sub>@GnP and MWNTs) was adjusted to 0.20 kJ·mg<sup>-1</sup>. The temperature of the dispersions was stabilized using an external thermostatic bath, set to a constant value, above the Krafft temperature ( $T_{kr}$ ) of the used surfactants. Finally, the position of the tip was fixed at 1 cm from the bottom of the flask.

In a first step, the layered nanomaterials, MoS<sub>2</sub> and GnPs, were combined into a 2D nanocomposite, MoS<sub>2</sub>@GnP. The obtained nanocomposite was then combined with MWNTs, to produce the 3D (MoS<sub>2</sub>@GnP)@MWNT hybrid material (more details in Sections 2.2.1, 2.2.2 and 2.2.3). Some of the experimental conditions applied were previously explored and optimized by our research group.<sup>74-77, 85</sup> The used surfactant concentration corresponds to the maximum dispersibility of the nanomaterial.<sup>75, 77, 85</sup> In the next sections, each adopted process is described in detail.

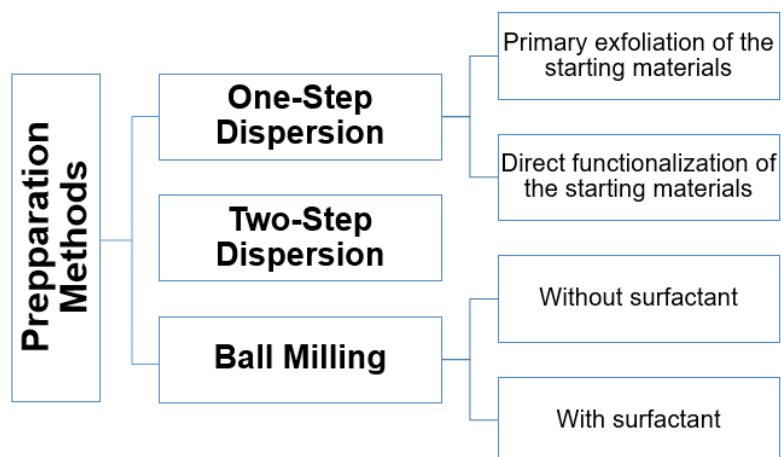


Figure 9. Different experimental procedures explored for the preparation of the MoS<sub>2</sub>@GnP and the (MoS<sub>2</sub>@GnP)@MWNT nanocomposites.

### 2.2.1. One-Step Dispersion

In this procedure, the GnPs and MoS<sub>2</sub> precursors were functionalized and exfoliated together in the same dispersion (*one-step dispersion*), using two different methodologies, as shown in Figure 10.

#### i) *Method a): Primary exfoliation of the starting materials*

By the methodology a), the GnPs and MoS<sub>2</sub> precursors simultaneously underwent a preliminary exfoliation in aqueous medium (without the presence of surfactant) using 20 mL of Milli-Q water and a total mass of 60 mg (MoS<sub>2</sub> and GnPs, 3 mg·mL<sup>-1</sup> of initial loading). The dispersion was tip-sonicated over 23 minutes, using a total energy of 0.8 kJ·mg<sup>-1</sup>, and then deposited on a cellulose acetate substrate inserted in a vacuum filtration system. Lastly, the as-synthesized material was dried overnight and labelled as **1S\_E** (Figure 10). To ensure that the nanomaterials remain dispersed through the electrostatic repulsions established between the layers, the zeta potential ( $\zeta$ ) of the dispersion was measured using an Anton Paar Litesizer<sup>TM</sup> 500, according to a previously methodology.<sup>123</sup> The dispersion of the 1S\_E sample showed a  $\zeta = -37$  mV, indicating that when the two 2D nanomaterials are dispersed in Milli-Q water they exhibit negative surface charge.

In the preparation of the respective 3D nanocomposite, firstly 60 mg of non-covalently functionalized MWNTs (initial loading of 3 mg·mL<sup>-1</sup>) were dispersed in 20 mL of an aqueous solution composed by CTAB (1 mmol·Kg<sup>-1</sup>) and PVP (1 % m/m). The dispersion was tip-sonicated for 9 minutes, delivering a total energy of 0.20 kJ·mg<sup>-1</sup>. After sonication, the dispersion was centrifuged (Centurion Scientific K241R) at 4000 g for 20 minutes. Then, an 18 mL aliquot of the supernatant was collected, taking care to not transfer the precipitate, consisting of larger MWNTs aggregates. The obtained dispersion was characterized by a combination of Ultraviolet Visible spectroscopy (UV-Vis) and thermogravimetric analysis (TGA), according to a previously methodology.<sup>75, 77</sup> The mass of MWNTs present in the supernatant was one third of the initial mass used in the initial dispersions. For the preparation of the initial 1D/2D nanocomposite, as the loading of the 2D nanocomposite did not suffer any mass loss, the mass ratio between (MoS<sub>2</sub>@GnP):MWNTs was fixed at the value of 3:1. The zeta potential for the MWNTs dispersion was already measured in a previous work by our research group ( $\zeta = +17$  mV), showing that the MWNTs are coated with the CTAB/PVP mixture.<sup>123</sup>

Before mixing of the MWNTs and MoS<sub>2</sub>@GnP dispersions, it was necessary to add SC to the latter dispersion. The SC added corresponded, for the total dispersion volume, to a concentration of 5 mmol·kg<sup>-1</sup>. Thereafter, equivalent volumes of the aforementioned

dispersions were mixed and sonicated. At the end, the aqueous phase was removed during vacuum filtration and the  $(\text{MoS}_2@\text{GnP})@\text{MWNT}$  nanocomposite obtained was rinsed with ethanol, to remove the excess of surfactant, and dried overnight. The final material was labelled as **1S\_E@MWNT** (Figure 10).

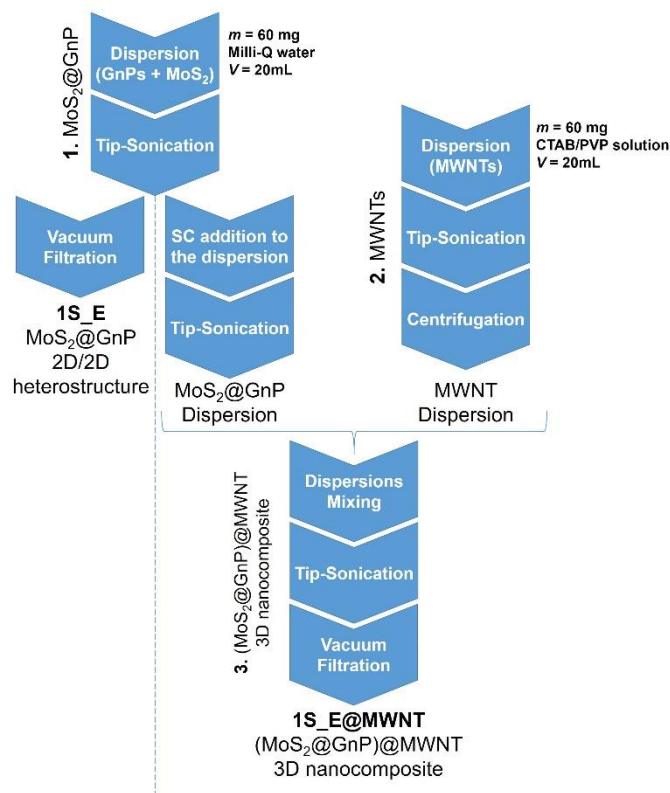


Figure 10. Flowchart of the sequential preparation order by method a) of the one-step dispersion procedure, with the alternative routes of the synthesis of the **1S\_E** and **1S\_E@MWNT** nanocomposites.

ii) *Method b) – Direct functionalization of the starting materials*

For the methodology b), the same procedure as described above for the preparation of **1S\_E** was used, with the only difference that an aqueous surfactant solution of SC (concentration of  $5 \text{ mmol}\cdot\text{kg}^{-1}$ ) was used as the initial dispersing medium. Furthermore, the sample was washed with ethanol before being dried overnight, to remove the excess of surfactant. The obtained material was labelled as **1S\_F** (Figure 11). The dispersion of the **1S\_F** sample also showed a negative value of zeta potential,  $-57 \text{ mV}$ , confirming the coating of the nanomaterials with the anionic SC molecules.

Additionally, to evaluate the influence of the building blocks on electrocatalytic performance, two nanocomposites similar to **1S\_F**, namely **1S\_F(9:1)** and **1S\_F(1:9)**, were synthesized. The first material was obtained by a mixture of  $54 \text{ mg}$  of GnPs and  $6 \text{ mg}$  of  $\text{MoS}_2$  and the latter with the inverse mass ratio.

The preparation of the respective 3D nanocomposite also followed the same procedure described for 1S\_E@MWNT material, with the exception that the MoS<sub>2</sub>@GnP dispersion did not undergo any additional steps before being mixed with the MWNTs dispersion. The final nanocomposite was named as **1S\_F@MWNT** (Figure 11). As for the laminar nanocomposite, the impact of the components for the electrocatalytic performance was also studied. To this end, a nanocomposite similar to 1S\_F@MWNT was obtained, with an inverse (MoS<sub>2</sub>@GnP):MWNTs ratio, which in this case was 1:3. The composite was named as **1S\_F@MWNT (1:3)**.

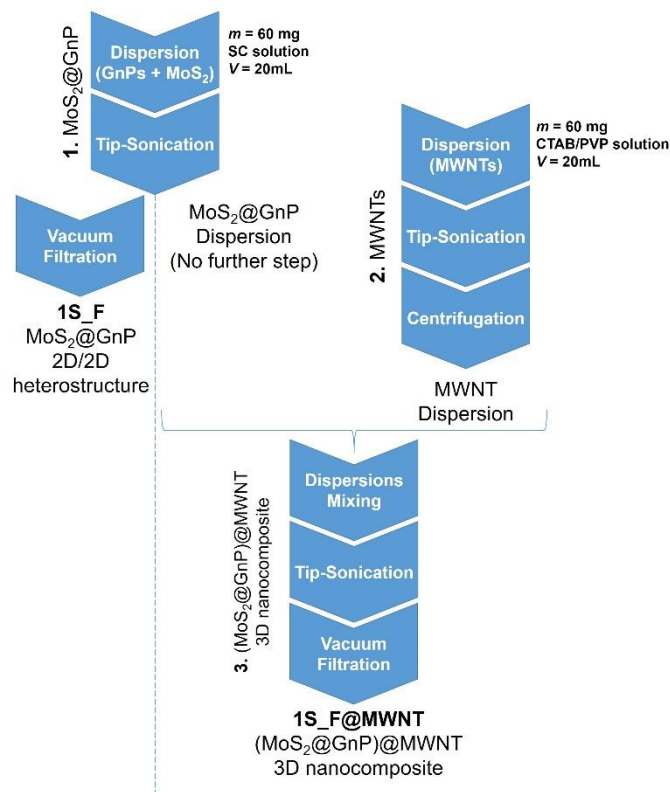


Figure 11. Flowchart of the sequential order preparation by method b) of the One-step dispersion procedure, with the alternative routes of the synthesis of the 1S\_F and 1S\_F@MWNT nanocomposites.

### 2.2.2. Two-Step Dispersion

This procedure was not subdivided into two methodologies because in order, to safeguard the restacking of GnPs and MoS<sub>2</sub>, the presence of surfactant in the two dispersions was indispensable since the first step. TX-100 and SC surfactants were used for the dispersion of GnPs and MoS<sub>2</sub>, respectively, and chosen in accordance with studies previously performed by our research group.<sup>75, 85</sup> Firstly, GnPs and MoS<sub>2</sub>

precursors were functionalized and exfoliated separately. Each dispersion contained 10 mL of the suitable surfactant aqueous solution (concentrations of  $5 \text{ mmol}\cdot\text{kg}^{-1}$ ) and 30 mg of material. Both dispersions underwent sonication over 11 minutes individually, total energy of  $0.80 \text{ kJ}\cdot\text{mg}^{-1}$ , and then the dispersions were mixed and tip-sonicated together for 23 minutes. The last dispersion was finally vacuum filtered and rinsed with ethanol. The obtained material was dried overnight and labelled as **2S** (Figure 12). The Two-step dispersion procedure served as a measure of the influence of the individual exfoliation of the two nanomaterials on the nanocomposite structure. Similarly, the zeta potential value was measured for the dispersion of sample 2S. In this case the dispersion showed  $\zeta = -34 \text{ mV}$ , also indicating the presence of a negative surface charge.

The respective 3D nanocomposite **2S@MWNT** was prepared by a similar procedure as previously mentioned in the one-step dispersion procedure (Figure 12). The  $\text{MoS}_2\text{@GnP}$  dispersion did not undergo any additional steps before mixing with the functionalized MWNTs.

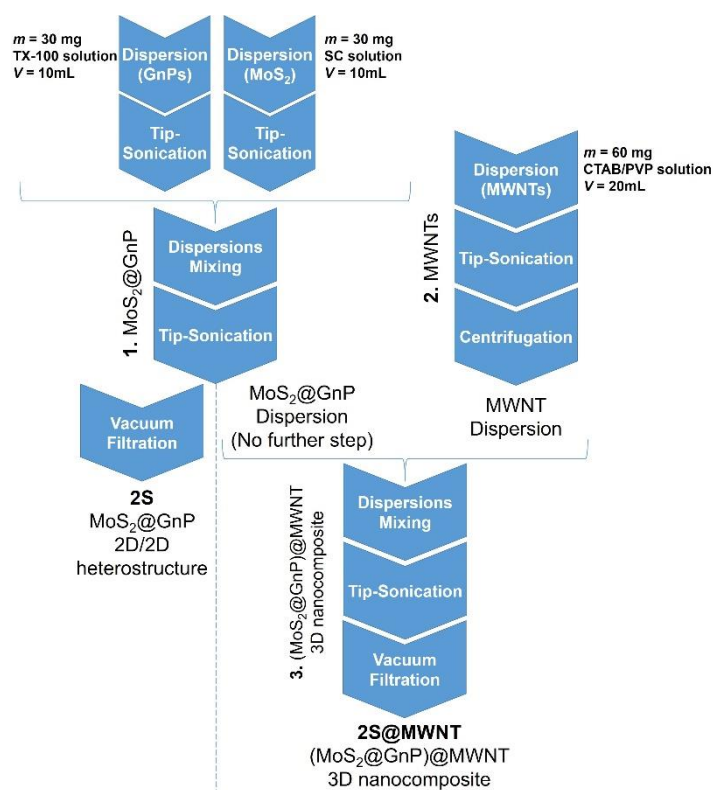


Figure 12. Flowchart of the sequential preparation order by the two-step dispersion procedure, with the alternative routes of the synthesis of the 2S and 2S@MWNT nanocomposites.

### 2.2.3. Ball Milling

The MoS<sub>2</sub>@GnP nanomaterial was also prepared by a dry mechanical approach using a ball mill (Retsch MM200). The main objective of this method was to obtain the MoS<sub>2</sub>@GnP nanomaterial through a solvent-free approach and in a higher amount. As shown in Figure 9, the Ball Milling method was also carried out along two methodologies.

i) *Method a): Ball Milling without surfactant*

The methodology a) was based on the direct mixture of the bulk starting materials without the presence of powder surfactant (**BM\_wos**, Figure 13). In a reactor with a volume of 25 mL, the bulk materials were mixed and exfoliated simultaneously for 5h at a constant frequency of 15 vibrations s<sup>-1</sup>.

For the 3D nanocomposite, in a first step, using a 25 mL reactor, simultaneous grinding and mixing of the MWNTs with the surfactant powder CTAB and the polymer PVP took place for 5 h at a constant frequency of 15s<sup>-1</sup>. At the end, the solid obtained was collected. Noteworthy, like in the production of the 2D nanocomposite, the amount of the surfactant and polymer added corresponded to the same concentration used in the dispersions prepared in section 2.2.1 ii) (CTAB and PVP, 1 mmol·kg<sup>-1</sup> and 1 % m/m, respectively). In a second step, the BM\_wos 2D heterostructure was mixed with SC in the ball mill, using similar conditions. Finally, the two obtained functionalized powders (CTAB/PVP-functionalized MWNTs and SC-functionalized 2D heterostructures) were mixed again in the ball mill to obtain the 3D nanocomposite **BM\_wos@MWNT** (Figure 13).

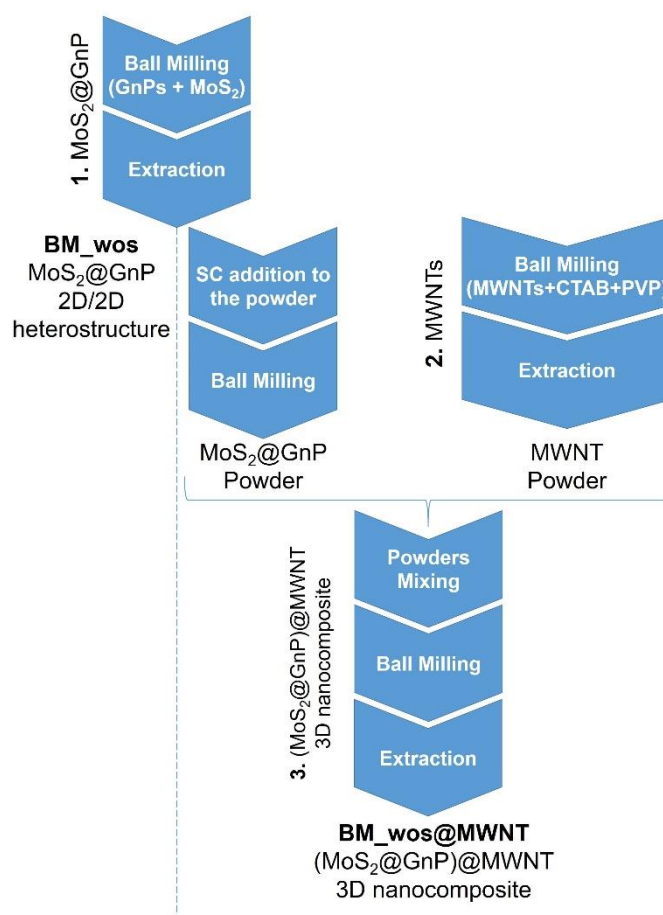


Figure 13. Flowchart of the sequential preparation order by method a) of the ball milling procedure, with the alternative routes of the synthesis of the BM\_wos and BM\_wos@MWNT nanocomposites.

ii) *Method b): Ball Milling with surfactant*

In the methodology b), the preparation of the composite in the ball mill was performed in the presence of SC surfactant (**BM\_ws**, Figure 14). MoS<sub>2</sub>, GnPs and SC were mixed directly into the reactor, keeping the remain experimental conditions similar to those described for BM\_wos. The amount of surfactant added corresponded to that needed to obtain a concentration of 5 mmol·kg<sup>-1</sup>, considering the amount of MoS<sub>2</sub>@GnP present in the reactor. At the end of the experiment, the material obtained was collected.

For the preparation of the respective (MoS<sub>2</sub>@GnP)@MWNT composite, the CTAB/PVP-functionalized MWNTs counterpart was prepared as described for method a), and the as-obtained BM\_ws 2D heterostructure was directly mixed with functionalized MWNTs, in the ball mill, keeping the remain experimental conditions (**BM\_ws@MWNT**, Figure 14).

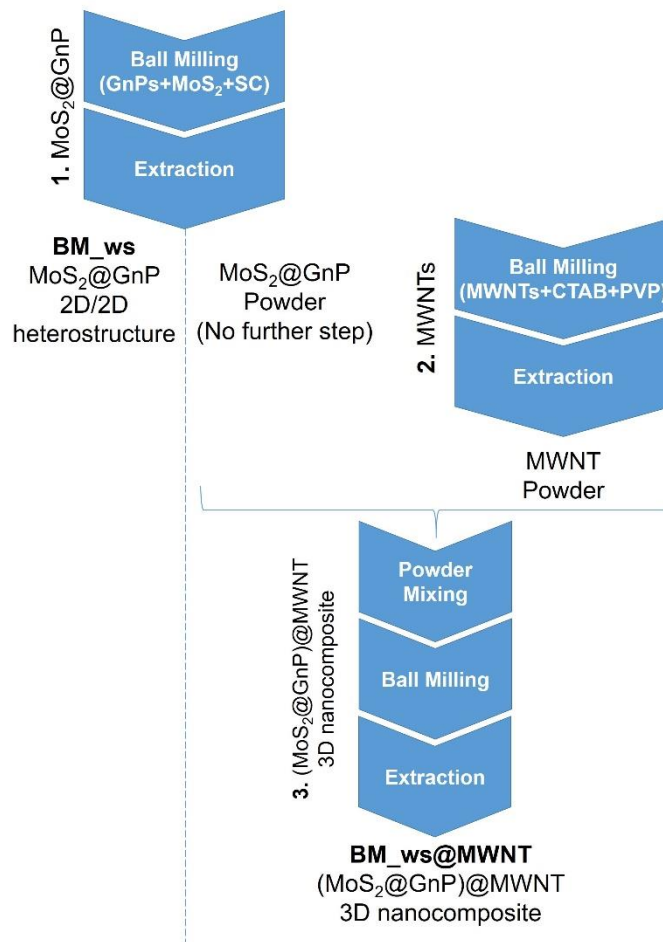


Figure 14. Flowchart of the sequential preparation order by method b) of the ball milling procedure, with the alternative routes of the synthesis of the  $\text{BM}_{\text{ws}}$  and  $\text{BM}_{\text{ws}}@\text{MWNT}$  nanocomposite.

#### 2.2.4. Preparation of $\text{MoS}_2@\text{N-GnP}$ and $(\text{MoS}_2@\text{N-GnP})@\text{MWNT}$ materials

The preparation of composites with nitrogen-doped GnPs was also performed. Firstly, N-doped GnPs (N-GnPs) were prepared according to a procedure based on ref.<sup>24</sup>. Briefly, 0.60 g of GnPs were mixed with 0.26 g of melamine using a ball mill for a period of 5 h with a constant frequency of  $15 \text{ s}^{-1}$ . The obtained material was annealed at  $600 \text{ }^\circ\text{C}$  during 1 h (under a  $\text{N}_2$  flow and with a heating rate of  $10 \text{ }^\circ\text{C}\cdot\text{min}^{-1}$ ).

The preparation of the nanocomposites  $\text{MoS}_2@\text{N-GnP}$  and  $(\text{MoS}_2@\text{N-GnP})@\text{MWNT}$  was based on methodology b) of the one-step dispersion procedure, thus maintaining the experimental conditions for the combination of  $\text{MoS}_2$  with N-GnPs and  $\text{MoS}_2@\text{N-GnP}$  with MWNTs. The respective obtained nanomaterials were named as **1S\_F(N-GnP)**, **1S\_F(N-GnP)@MWNT (1:3)** and **1S\_F(N-GnP)@MWNT (3:1)**.

## 2.3. Characterization Techniques

Scanning electron microscopy (SEM) and powder X-ray diffraction (P-XRD), were used for the morphological and structural characterization of the materials produced.

SEM is a very attractive method for both qualitative and quantitative characterizations of materials. First, SEM excels at producing three-dimensional images of surfaces of a variety of materials (both organic and inorganic) and visualizing/analyzing regions on the nanometer and micrometer scale.<sup>124</sup> The process of obtaining micrographs is based on the generation of a fine beam of electrons from the electron gun, which with the aid of condenser lenses and scanning coils, will induce an impact on the sample surface. The secondary and backscattered electron detectors collect the electrons from the sample and record their energy and intensity. At the end, the intensity distributions of the recorded signals form the magnified image of a section of the sample.<sup>124, 125</sup>

The SEM characterization was performed in a scanning electron microscope, *FEI Quanta 400FE*, at Centro de Materiais da Universidade do Porto (CEMUP), with a secondary electron beam and energies of 15 kV. The samples were analyzed at magnifications between 5000x and 100000x. The analysis of the nanocomposites obtained by the ball milling procedures was carried out by studying the samples deposited on silicon substrates. For this purpose, drops of an aqueous dispersion containing the material of interest were deposited on preheated substrates. With due care, the solvent was evaporated after adding the drops.

On the other hand, for the nanocomposites prepared through one-step dispersion and two-step dispersion procedures, the cross sections of the different materials were analyzed. Liquid nitrogen was used to induce the sample fracture and to obtain intact cross sections. For that, after being rinsed with ethanol, each sample was immediately immersed in liquid nitrogen.

P-XRD is an important technique in the structural characterization of various materials, presenting the advantage of to be a non-destructive technique. X-ray diffraction lies in the elastic scattering of X-ray photons by atoms in a structure. The process occurs when an X-ray photon collides with one of the electrons of the absorbing element, thus changing direction. The scattered X-rays that are in the same phase cause constructive interference.<sup>126</sup> The interplanar distance,  $d$ , can be obtained by measuring the angle at which the diffracted rays leave the sample using the Bragg's law (equation (5)):<sup>126</sup>

$$n\lambda = 2d \sin \theta \quad (5)$$

where  $n$  is the order of reflection,  $\lambda$  is the wavelength of the X-rays, and  $\theta$  is the angle between the incident beam and the normal to the reflected plane of the lattice. The results

obtained correspond to graphical representations of the detected X-ray diffraction intensity as a function of  $2\theta$ .<sup>126, 127</sup> The analysis of the results was based on the comparison of the diffractograms between the starting materials and the synthesized nanocomposites.

The P-XRD (Powder X-ray Diffraction) characterization was performed at CICECO, Aveiro Institute of materials, Universidade de Aveiro, on an X-ray diffractometer, Rigaku, Geigerflex, with a monochromatized  $\text{Cu}_{K\alpha}$  radiation ( $\lambda = 1.5406 \text{ \AA}$ , 45 Kv, 40 mA). The data was recorded with a  $0.026^\circ$  step size, at 96 s/step.

## 2.4. Electrochemical studies

For all electrochemical studies, an Autolab PGSTAT 302N potentiostat/galvanostat (EcoChimie B.V.), controlled by Nova v2.0 software, was used. A three-electrode electrochemical cell was used, based on a glassy carbon rotating disk electrode (RDE, 3 mm of diameter, Metrohm) or a rotating ring disk electrode (RRDE, Metrohm) of glassy carbon disk (5 mm of diameter) with a platinum ring (375  $\mu\text{m}$  of diameter) as working electrode, an Ag/AgCl (3 mol·dm<sup>-3</sup> KCl, Metrohm) reference electrode and a carbon rod (2 mm of diameter, Metrohm, for ORR studies) or a Pt wire (Goodfellow, diameter of 0.6 mm,  $l = 0.5 \text{ m}$ , > 99.99%), for OER studies) as counter electrode. All experiments used a KOH solution (0.1 mol·dm<sup>-3</sup>, 125 mL) as supporting electrolyte and were carried out at room temperature.

Before the working electrode modification, its surface was polished/cleaned. Typically, polishing was performed on a microcloth polishing pad (BAS Bioanalytical Systems Inc.), using diamond pastes (MetaDi II, Buehler) with three different particle sizes - 6, 3 and 1  $\mu\text{m}$  - and aluminum oxide of particle size 0.3  $\mu\text{m}$  (Buehler). The polishing pastes were used sequentially, from the pastes with the largest particle size to the smallest. After polishing, the working electrode was rinsed with water.

For the RDE (or RRDE) modification, a suitable dispersion of each material was prepared. Briefly, 1 mg of the sample of interest was measured and dispersed in a mixture consisting of 125  $\mu\text{L}$  of ultrapure water (Interface system), 125  $\mu\text{L}$  of isopropanol and 20  $\mu\text{L}$  of Nafion, using an ultrasonic bath (Fisherbrand FB11201) until a homogeneous ink was formed. Then, three 2.5  $\mu\text{L}$  drops were deposited on the RDE surface and allowed to dry under air flux. For the analyzed samples, loadings in the range of 452 to 6260  $\mu\text{g}\cdot\text{cm}^{-2}$  were obtained.

From the Nernst equation, equation (6), all the experimental potential values  $E$  vs. Ag/AgCl ( $E_{\text{Ag/AgCl}}$ ) used in this work were converted to  $E$  vs. RHE (reversible hydrogen

electrode,  $E_{RHE}$ ), taking  $E^{\circ}_{Ag/AgCl} = 0.1976$  V (at 25 °C). This conversion was used to facilitate comparisons with the literature values.

$$E_{RHE} = E_{Ag/AgCl} + 0.059pH + E^{\circ}_{Ag/AgCl} \quad (6)$$

#### 2.4.1. ORR studies

The supporting electrolyte was saturated for 30 min with nitrogen or oxygen before each experiment. Electrochemical analysis was performed by cyclic voltammetry (CV) and linear sweep voltammetry (LSV). The scan rate was fixed at 0.005 V·s<sup>-1</sup> for both techniques, and for the LSVs the electrode rotation speed varied between 400 and 3000 rpm. The currents measured in N<sub>2</sub>-saturated solutions were subtracted from the currents measured in O<sub>2</sub>-saturated solutions. The potential used for the CV and LSV assays ranged from 0.1 to -0.65 V vs. Ag/AgCl.

Using the data of the LSVs, electrochemical parameters such as the onset potential ( $E_{onset}$ ) and diffusion-limiting current density ( $j_L$ ) values were extracted. Here, the  $E_{onset}$ , *i.e.* the potential at which O<sub>2</sub> reduction starts, was calculated by two different methods: i) assuming that it corresponds to 5 % of the diffusion-limiting current density; and ii) assuming that it corresponds to the potential at which the slope of the voltammogram exceeds the value of 0.1 mA·cm<sup>-2</sup>.<sup>85, 97</sup>

Additionally, analysis of the obtained LSVs, using the Koutecky-Levich (K-L) equation (equation 7), allowed the estimation of the number of electrons transferred per molecule of O<sub>2</sub>,  $n_{O_2}$ , during the oxygen reduction process.<sup>85</sup>

$$\frac{1}{j} = \frac{1}{j_L} + \frac{1}{j_k} = \frac{1}{B\omega^{1/2}} + \frac{1}{j_k} \quad (7)$$

In equation (7)  $j$  corresponds to the current density measured,  $j_L$  is defined as the diffusion-limiting current density,  $j_k$  is the kinetic current density and  $\omega$  is the angular velocity. From the parameter  $B$  (variable related to the diffusion limiting current density), extracted from the K-L plot slopes, and equation (8) the value of  $n_{O_2}$  was determined.

$$B = 0.2n_{O_2}F(D_{O_2})^{2/3}\nu^{-1/6}C_{O_2} \quad (8)$$

In equation (8)  $F$ , the Faraday constant, is equal to 96485 C·mol<sup>-1</sup>,  $D_{O_2}$  is the O<sub>2</sub> diffusion coefficient (1.95×10<sup>-5</sup> cm<sup>2</sup>·s<sup>-1</sup>),  $\nu$  represents the electrolyte kinematic viscosity (8.977×10<sup>-3</sup> cm<sup>2</sup>·s<sup>-1</sup>) and  $C_{O_2}$  is the bulk concentration of O<sub>2</sub> (1.15×10<sup>-3</sup> mol·dm<sup>-3</sup>).<sup>85</sup> The value indicated for each parameter was based on the electrolyte used in the experiments, 0.1 mol·dm<sup>-3</sup> KOH, and the constant 0.2 was used according with rotation speeds expressed in rpm.

Complementarily, for the nanocomposites that exhibited promising electrocatalytic activity, long-term electrochemical stability and methanol tolerance tests were performed through chronoamperometry measurements. For this purpose, the electrocatalytic stability was evaluated, during 50,000 s in a O<sub>2</sub>-saturated electrolyte, applying a constant potential value of  $E = -0.45$  V vs. Ag/AgCl and a constant rotation rate of 1600 rpm. The methanol resistance tests were also performed under similar experimental conditions. However, the elapsed time was 2500 s, with injection of 2.5 mL of methanol (0.5 mol·dm<sup>-3</sup>) into the electrolyte when 1000 s of reaction time was reached.

Lastly, within the wide range of ORR electrocatalytic analyses, the hydrogen peroxide (H<sub>2</sub>O<sub>2</sub>) production was also measured, following the same principles of the previously presented electrode system setup, but using the RRDE as working electrode. The RRDE disk was scanned at a scan rate of 0.005 V·s<sup>-1</sup> in the potential range from 0.1 to -0.65 V vs. Ag/AgCl at 1600 rpm, while the Pt ring was kept at a constant potential of  $E = 0.2$  V vs. Ag/AgCl, to ensure the oxidation of the newly formed H<sub>2</sub>O<sub>2</sub>.

According to equation (9) it was possible to determine the percentage of H<sub>2</sub>O<sub>2</sub> (%H<sub>2</sub>O<sub>2</sub>) formed during the ORR process:

$$\%H_2O_2 = 200 \times \frac{i_R/N}{i_D+i_R/N} \quad (9)$$

where the disk and ring currents are, respectively,  $i_D$  and  $i_R$ .  $N$  is the current collection efficiency of the platinum ring, which is in this case equal to 0.25.

#### 2.4.2. OER studies

In the electrochemical OER studies, prior to each test, the supporting electrolyte solution KOH (0.1 mol·dm<sup>-3</sup>, 125 mL) was N<sub>2</sub>-saturated. A scan rate of 0.005 V·s<sup>-1</sup> and rotational speed of 1600 rpm were applied to the working electrode. The potential ranged from 0.0 to 0.8 V vs. Ag/AgCl at 1600 rpm. OER analyses were performed by acquiring LSVs curves, where the circuit uncompensated resistances ( $R_u$ ) were estimated according to  $i$ -interrupt tests. From the calculated  $R_u$  value, new LSV compensation tests were performed, considering 90 % of the  $R_u$  value.

# **Chapter 3**

## *Results and Discussion*

## 3. Results and Discussion

### 3.1. Materials characterization

#### 3.1.1. Scanning Electron Microscopy

The morphological properties of the pristine starting materials - MWNTs, MoS<sub>2</sub>, GnPs and N-GnPs – and of the prepared nanocomposites were evaluated by SEM. In the next subsections the results obtained for the starting materials, the 2D and the 3D nanocomposites are shown.

##### 3.1.1.1. Starting materials

The morphological properties of the building materials, namely the MWNTs, MoS<sub>2</sub>, GnPs and N-GnPs (Figure 15) were initially analyzed. It can be observed that the MWNTs are arranged in dense agglomerates (Figure 15 **a**). MoS<sub>2</sub> and GnPs (Figure 15 **b** and **c**) have a sheet-like morphology and exhibit agglomerates of several layers which randomly intersect each other. In Figure 15 **d**, the effect of the N-doping process (ball milling and thermal treatment) in the morphology of N-GnPs is clear, with a compression and reduction of the nanoplatelets size in comparison with the pristine GnPs.

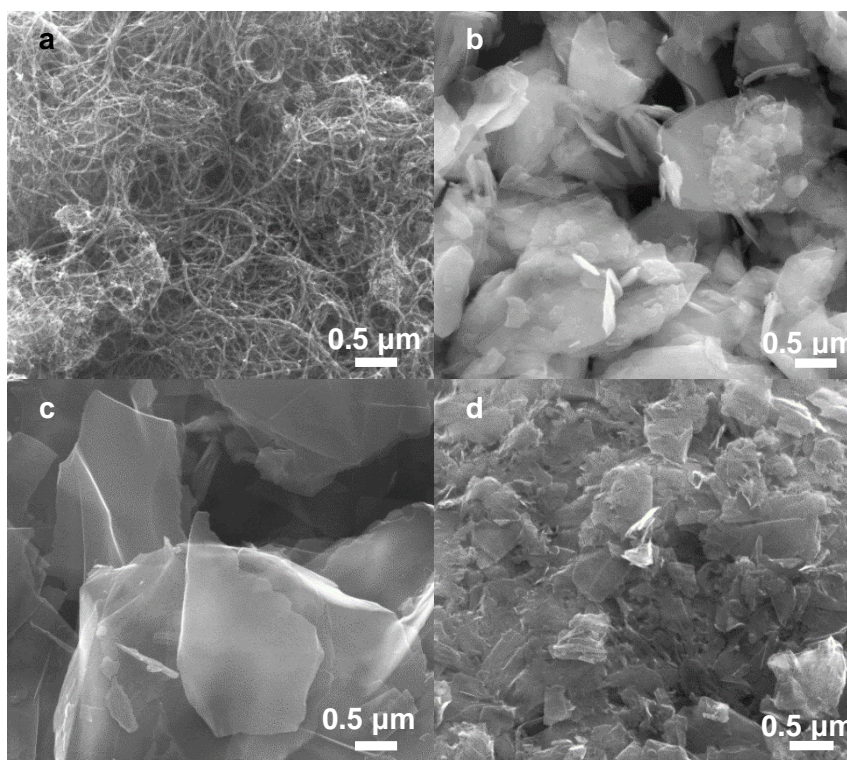


Figure 15. SEM micrographs, obtained at 50,000x magnification of: **a** MWNTs; **b** MoS<sub>2</sub>; **c** GnPs and **d** N-GnPs.

### 3.1.1.2. MoS<sub>2</sub>@GnP nanocomposites

As mentioned in section 2.3, the morphological studies were based on the comparison of different cross-sections for the materials obtained by the one-step dispersion and two-step dispersion procedures. For the samples obtained by the ball milling procedure, a top view perspective was used for the analyses.

Firstly, the micrographs of 1S\_E and 1S\_F materials are shown in Figures 16 **a**, **b** and **c**, **d**, respectively. In both cases, the combination of the two nanomaterials produced a structure without a defined orientation, with particles randomly distributed. However, the sheet edges are apparently more defined and exposed for sample 1S\_F compared to sample 1S\_E. Since the edges are the most reactive sites of these materials, exposing them may provide a beneficial effect in activating the oxygen reactions.<sup>43, 121, 128</sup>

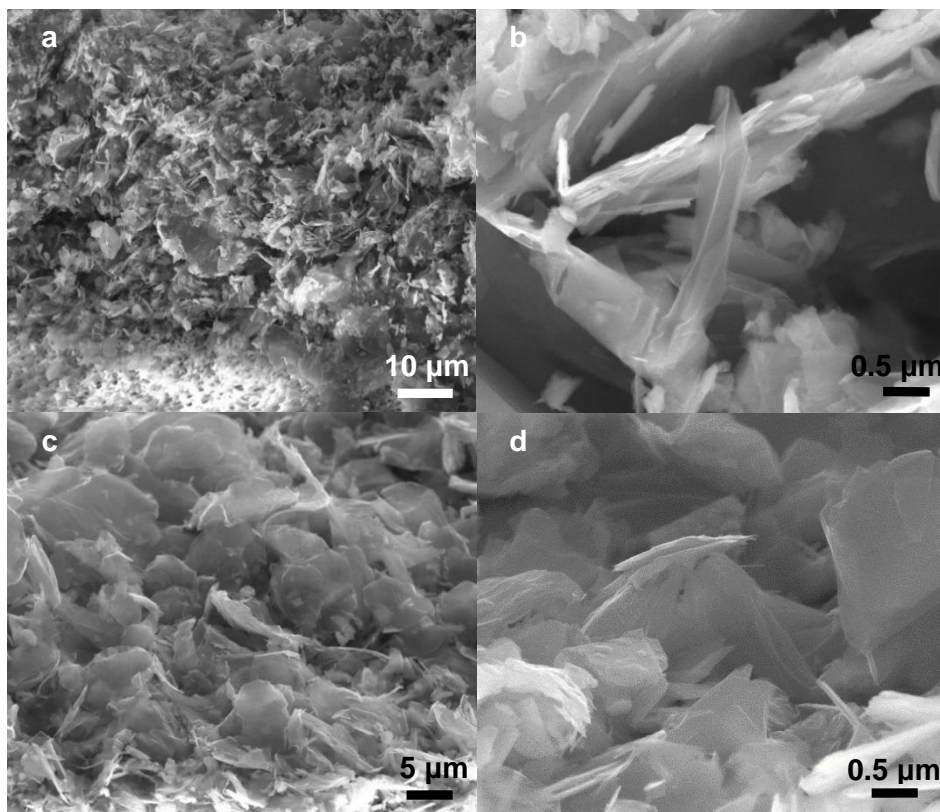


Figure 16. SEM micrographs of the cross sections of: **a** and **b** – 1S\_E (**a** 3000x magnification; **b** 50000x magnification); **c** and **d** – 1S\_F (**c** 5000x magnification; **d** 50000x magnification).

Sample 2S also demonstrated an unappreciable orientation, with a random arrangement of the nanoplatelets of the two nanomaterials, Figure 17.

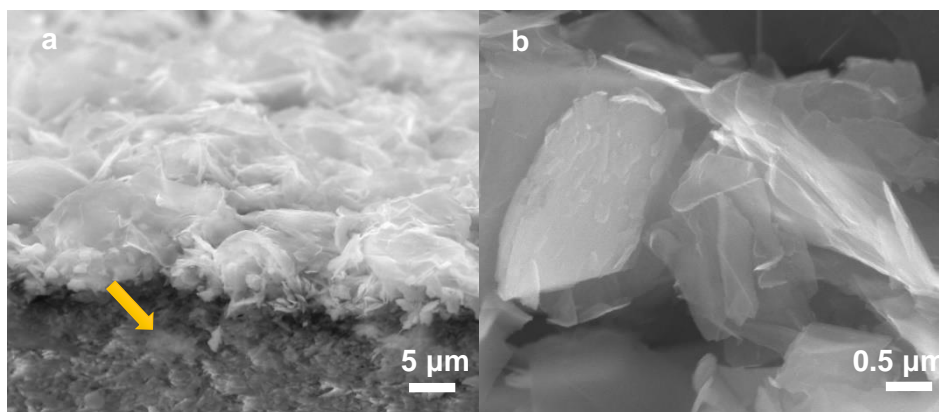


Figure 17. SEM micrographs of the cross sections of 2S **a** 5000x magnification (yellow arrow corresponds to the cellulose acetate substrate); **b** 50000x magnification).

Within the studies carried out for the  $\text{MoS}_2@\text{GnP}$  nanocomposites, the influences of the initial loading of the starting materials and of the nitrogen atom doping in the GnPs were evaluated. As will be described in the electrochemical studies, the use of mass ratios different than 1:1 ( $\text{GnPs}:\text{MoS}_2$ ) did not contribute to the improvement of the electrocatalytic performance (see section 3.2.1.1); thus, the morphological study for these nanocomposites was not performed.

On the other hand, the hybrid material consisting of  $\text{MoS}_2$  and N-GnPs was analyzed by SEM (Figure 18). Compared to 1S\_F (Figure 16 **c** and **d**), the 1S\_F(N-GnP) nanocomposite shows smaller sheets packed together in an apparently continuous structure. The reduction in the size of the nanoplatelets may have resulted from the doping process via ball milling, as shown in Figure 15 **c** and **d**.

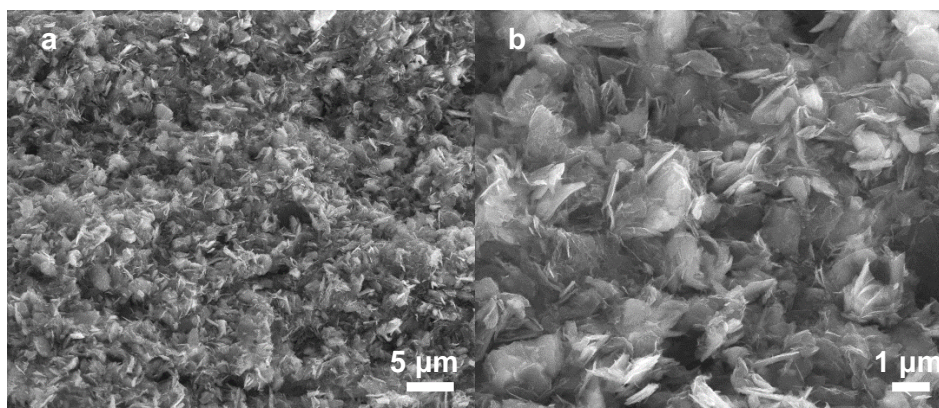


Figure 18. SEM micrographs of the cross sections of 1S\_F(N-GnP) (**a** 5000x magnification; **b** 20000x magnification).

For the BM\_wos and BM\_ws materials, the SEM micrographs are presented, respectively, in Figures 19 **a**, **b** and **c**, **d**.

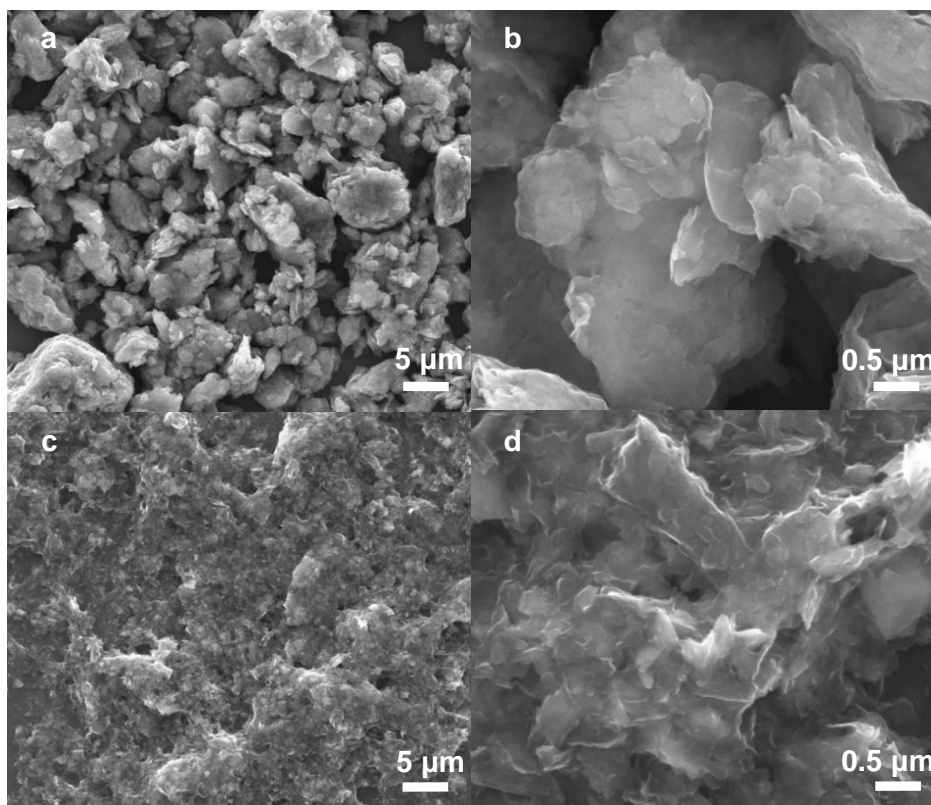


Figure 19. SEM micrographs of: **a** and **b** – BM\_wos (**a** 5000x magnification; **b** 50000x magnification); **c** and **d** – BM\_ws (**c** 3000x magnification; **d** 50000x magnification).

Figure 19 shows that the presence of the surfactant SC affects the morphology of the hybrid material, as the clusters are more compacted and less individualized when compared with the BM\_wos sample.

### 3.1.1.3. (MoS<sub>2</sub>@GnP)@MWNT nanocomposites

The results obtained for the first series of 3D nanocomposites showed an impact of the preparation method on the structuring of the materials. In the composites built using methods a) and b) of the one-step dispersion procedure, an interaction of the 2D heterostructure with the carbon nanotubes took place (Figure 20).

From the micrographs, one observed that the MWNTs are arranged between the basal planes of the heterostructure sheets. Additionally, the 2D layers are better organized, with the sheets lying predominantly in a horizontal orientation and vertically stacked. Carbon nanotubes can prevent the restacking of the 2D sheets, thus promoting the exposure of new active sites and the edges of the sheets.

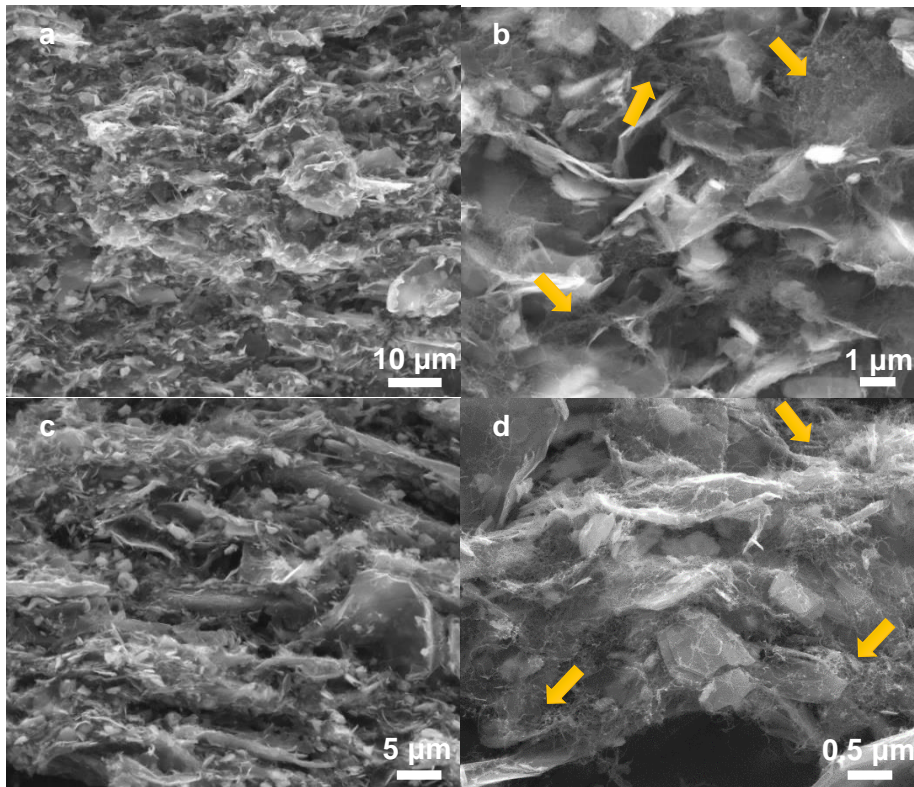


Figure 20. SEM micrographs of the cross sections of: **a** and **b** – 1S\_E@MWNT (**a** 3000x magnification; **b** 20000x magnification); **c** and **d** – 1S\_F@MWNT (**c** 5000x magnification; **d** 50000x magnification); (yellow arrows – visible MWNT networks).

Imaging of the 2S@MWNT material similarly confirmed the presence of MWNTs between the layers. Dense networks of MWNTs but a less defined structuration are observed for this sample. Nevertheless, this type of lower degree of organization could be positive for the electrocatalytic properties.

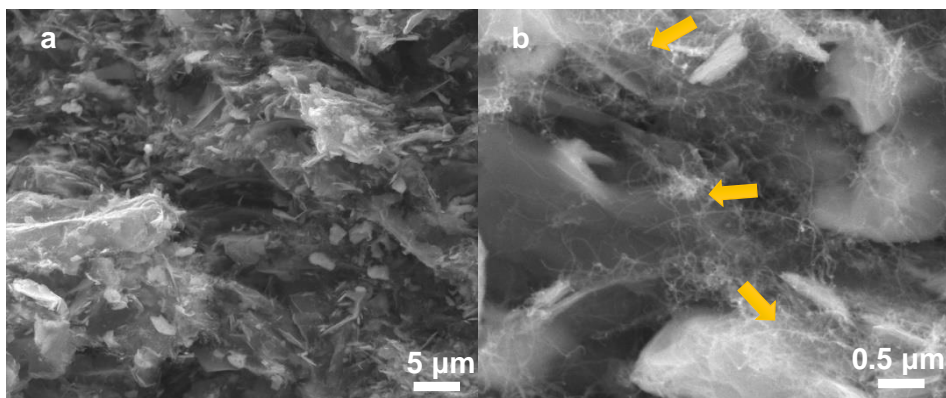


Figure 21. SEM micrographs of the cross sections of 2S@MWNT (**a** 5000x magnification; **b** 50000x magnification); (yellow arrows – visible MWNT networks).

Comparing the structures of the three materials 1S\_E@MWNT, 1S\_F@MWNT and 2S@MWNT, a more defined parallel vertical stacking of the laminar composite sheets is observed for sample 1S\_F@MWNT (Figure 20 c). Thus, method b) of the one-step dispersion procedure was selected as a potentially useful method for preparing the 3D nanocomposite in liquid phase.

The 3D nanocomposites were addressed regarding the effect of mass ratio and N-doping of the GnPs. Firstly, to evaluate the influence of the mass ratio between components on these nanocomposites, a new material (MoS<sub>2</sub>@GnP)@MWNT was prepared. Thus, a ratio of 1:3 (MoS<sub>2</sub>@GnP:MWNTs) was used, and the sample was labelled as 1S\_F@MWNT (1:3). The respective results can be seen in Figure 22. In 1S\_F@MWNT (1:3) material, dense networks of MWNTs are observable between the basal planes of the heterostructure. Furthermore, the vertical stacking of the GnP@MoS<sub>2</sub> particles is still visible, with the MWNTs apparently preventing the restacking, as observed in Figure 22 b.

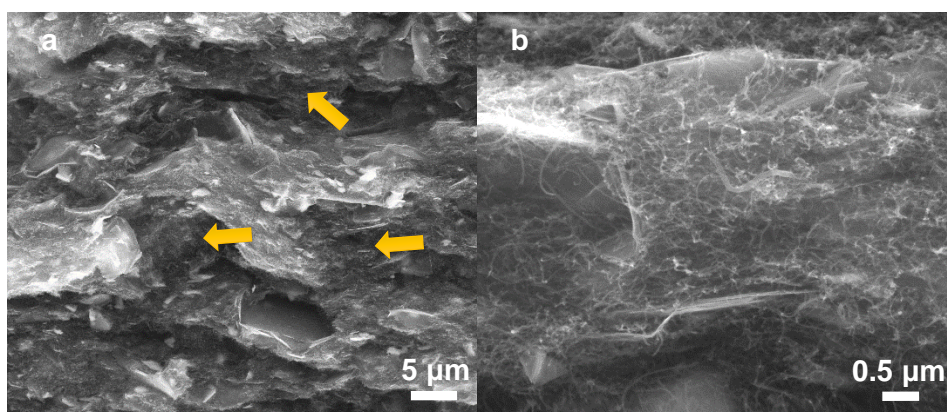


Figure 22. SEM micrographs of the cross sections of 1S\_F@MWNT (1:3) (a 5000x magnification; b 50000x magnification); (yellow arrows – visible MWNT networks).

In the context of the N-doping of the GnPs, two nanocomposites were prepared, with the only difference being the ratio of the components MoS<sub>2</sub>@GnP and MWNTs, (1:3) and (3:1). These materials were labelled 1S\_F(N-GnP)@MWNT (1:3) and 1S\_F(N-GnP)@MWNT (3:1), respectively.

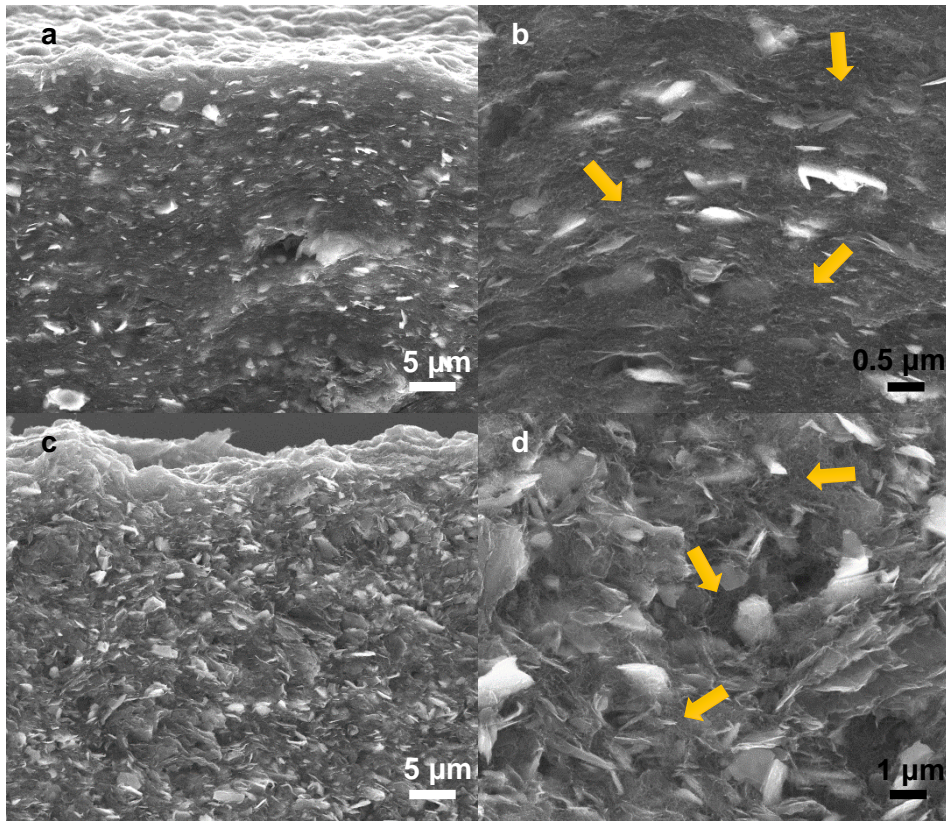


Figure 23. SEM micrographs of the cross sections of: **a** and **b** – 1S\_F(N-GnP)@MWNT (1:3) (**a** 5000x magnification; **b** 20000x magnification); **c** and **d** – 1S\_F(N-GnP)@MWNT (3:1) (**c** 5000x magnification; **d** 100000x magnification); (yellow arrows – visible MWNT networks).

The micrographs obtained confirmed the incorporation of the MWNTs in a regular formation, with the 2D layers being involved by the MWNTs. Sample 1S\_F(N-GnP)@MWNT (1:3) showed a more pronounced hierarchical structuration than 1S\_F(N-GnP)@MWNT (3:1), however the latter presents more exposed layers.

Figure 24 shows that the 3D materials obtained via ball milling, BM\_wos and BM\_ws, have a more compact and disorganized morphology compared to the composites built using the dispersion methodologies. Both samples show no significant differences between each other, and overall, the MWNTs are crumpled in the MoS<sub>2</sub>@GnP particles.

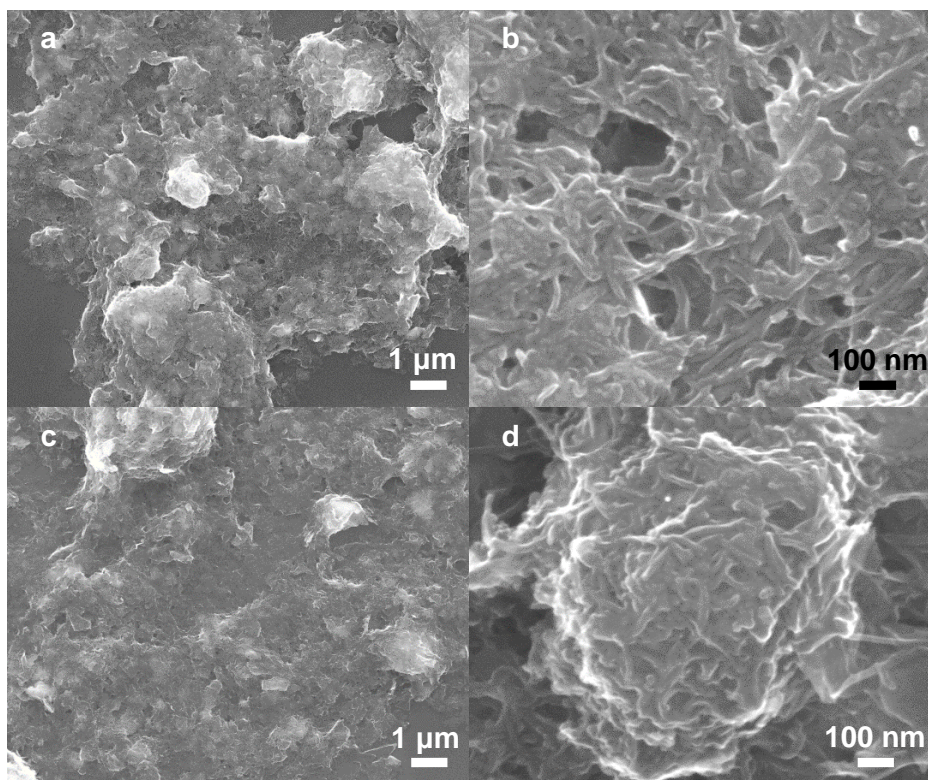


Figure 24. SEM micrographs of: **a** and **b** – BM\_wos@MWNT (**a** 20000x magnification; **b** 200000x magnification); **c** and **d** – BM\_ws@MWNT (**c** 20000x magnification; **d** 200000x magnification).

### 3.1.2. P-XRD characterization

To assess the chemical composition of the samples, characterization by P-XRD was performed. Fig. 25 shows the P-XRD patterns of the starting materials and of selected MoS<sub>2</sub>@GnP and (MoS<sub>2</sub>@GnP)@MWNT nanocomposites.

For GnPs, the diffractogram obtained shows two peaks, an intense peak at 26.5 ° and other at 54.7°, which are characteristics of graphene-type materials and ascribed to the refractive Miller indices (002) and (004), respectively (JCPDS card no. 04-013-0293).<sup>129</sup> Using Bragg's law, it was possible to determine the value of the GnPs layer-to-layer *d*-spacing, 0.34 nm. For MoS<sub>2</sub>, peaks at  $2\theta = 14.4^\circ, 32.7^\circ, 39.6^\circ, 44.2^\circ, 49.8^\circ, 58.4^\circ$  were identified and attributed to the planes (002), (100), (103), (006), (105) and (110), respectively (JCPDS card no. 37-1492).<sup>81, 121</sup> The diffraction peak at 14.4° indicates a layer-to-layer *d*-spacing of 0.62 nm for MoS<sub>2</sub>. Regarding MWNTs a small peak was identified at 26.0° referring to plane (002) (JCPDS card no. 75-1621).<sup>43, 130</sup>

Figure 25 shows a diffraction peak at 26.5° for the N-GnPs. The peak was identified as the (002) plane of graphene-type materials and the *d*-spacing was calculated as 0.34 nm, similarly to that obtained for pristine GnPs. This confirms that the structure of the nanomaterial was preserved after the ball milling process and thermal treatment.

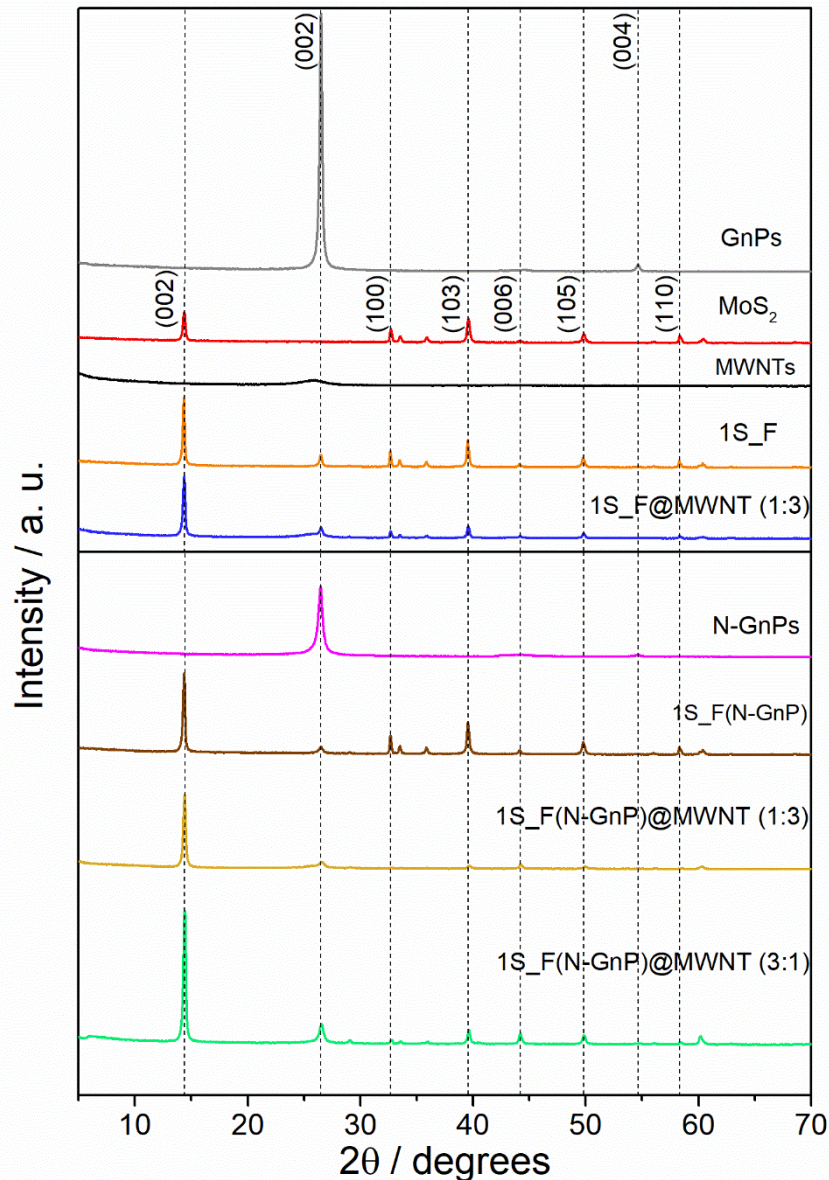


Figure 25. P-XRD patterns of: GnPs; MoS<sub>2</sub>; MWNTs; N-GnPs; 1S\_F; 1S\_F@MWNT (1:3); 1S\_F(N-GnP); 1S\_F(N-GnP) @MWNT (1:3) and 1S\_F(N-GnP) @MWNT (3:1).

For all the prepared nanocomposites, the characteristic peaks of MoS<sub>2</sub> were observed. Regarding the GnPs, only the peak correspondent to the (002) plane was identified. In the 3D nanocomposites, the peak at 26.5 ° has the contribution of both GnPs and MWNTs, since the MWNTs alone displayed a small peak around 26 ° ((002) plane). Additionally, the nanocomposites retained the position of the diffraction peaks for MoS<sub>2</sub> and graphene. Particularly, the peaks of the (002) planes maintained the initial position in the nanocomposites (MoS<sub>2</sub> - 14.4 °, GnPs - 26.5 °), which suggests that there is conservation of the interlayer distance of the GnPs and MoS<sub>2</sub> layers. In summary, the XRD patterns confirmed the presence and the retention of the inherent peaks of the

starting components, indicating that the building of the nanocomposites allowed to preserve the individual properties of the 1D and 2D building blocks.

## 3.2. Electrocatalytic activity for the oxygen reactions

In line with one of the main goals of this project, the ORR and OER electrocatalytic activities were evaluated for all the prepared nanomaterials. The extracted information allowed the selection of the most promising nanocomposites, as well as the evaluation of the influence of the preparation method and experimental parameters (namely, nanomaterials mass ratios and nitrogen doping) on the electrocatalytic performance.

The results of ORR and OER electrocatalytic activities will be divided into two sections corresponding to the 2D - MoS<sub>2</sub>@GnP - and 3D - (MoS<sub>2</sub>@GnP)@MWNT - nanocomposites. Each section will be divided in three subsections to discuss the impact of the different preparation methods, mass ratios between the building blocks, and the nitrogen atom doping of GnPs on the electrocatalytic response.

### 3.2.1. ORR electrocatalytic activity

The ORR electrocatalytic studies were based on the analysis of CVs and LSVs obtained in N<sub>2</sub>- and O<sub>2</sub>-saturated 0.1 mol·dm<sup>-3</sup> KOH solution. All materials tested did not demonstrated any electrochemical process in N<sub>2</sub>-saturated supporting electrolyte in the potential window explored (cf. Appendix, section A.1, Figures 40-45).

#### 3.2.1.1. MoS<sub>2</sub>@GnP nanocomposites

##### I. *Influence of the preparation methods*

In Figures 26 **a** and **b** the CVs and LSVs corresponding to the initial components MoS<sub>2</sub> and GnPs and to the 2D/2D heterostructures 1S\_E, 1S\_F, 2S, BM\_wos and BM\_ws are presented.

As can be observed in CVs, the materials exhibit a cathodic peak when the supporting electrolyte was O<sub>2</sub>-saturated, and it was possible to extract the potential of the cathodic peak ( $E_{pc}$ ) values. GnPs, MoS<sub>2</sub>, 1S\_E, 1S\_F and 2S exhibit cathodic peaks at, respectively,  $E_{pc} = 0.64, 0.61, 0.64, 0.65$  and  $0.64$  V vs. RHE. The materials obtained by the ball milling method showed the cathodic peak unfolded. The BM\_wos sample showed two cathodic peaks at  $0.64$  and  $0.76$  V vs. RHE and the BM\_ws at  $E_{pc} = 0.67$  and  $0.77$  V vs. RHE. As no cathodic peaks were observed when the electrolyte was N<sub>2</sub>-saturated, the peaks identified were assigned to the O<sub>2</sub> reduction and suggested that all tested materials are electrocatalytically active for the ORR. The  $E_{pc}$  values measured

were less positive than the value achieved for Pt/C reference (in this work,  $E_{pc} = 0.75$  V vs. RHE).

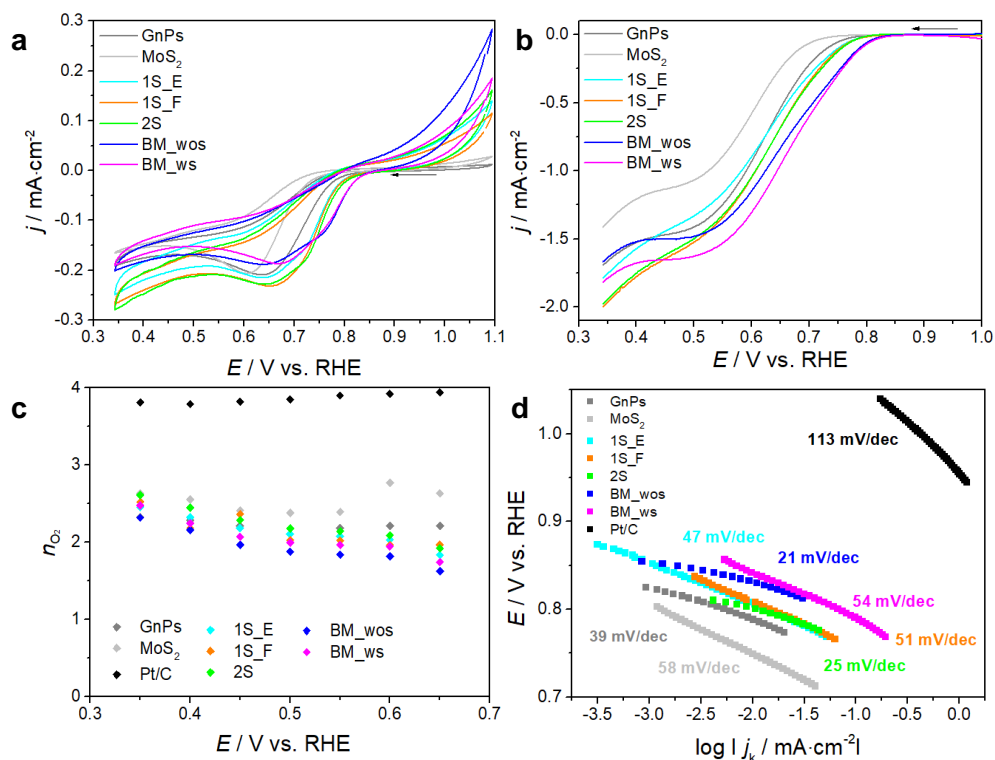


Figure 26. ORR electrocatalytic results for building blocks ( $\text{MoS}_2$  and  $\text{GnP}$ s),  $\text{MoS}_2@GnP$  nanocomposites (1S\_E, 1S\_F, 2S, BM\_wos and BM\_ws), and Pt/C: **a** CVs ( $\text{O}_2$ -saturated  $0.1 \text{ mol}\cdot\text{dm}^{-3}$  KOH,  $\nu = 0.005 \text{ V}\cdot\text{s}^{-1}$ ); **b** LSVs ( $\text{O}_2$ -saturated  $0.1 \text{ mol}\cdot\text{dm}^{-3}$  KOH,  $\nu = 0.005 \text{ V}\cdot\text{s}^{-1}$ ,  $\omega = 1600 \text{ rpm}$ ); **c**  $n_{\text{O}_2}$  estimated at different potential values; **d** Tafel plots with the respective TS values.

Figure 26 **b** shows the LSVs obtained for the considering materials and in Table 4 are summarized the parameters extracted from them:  $j_L$  and  $E_{\text{onset}}$  values. The 2D nanocomposites showed  $j_L$  values from  $-1.67$  to  $-2.00 \text{ mA}\cdot\text{cm}^{-2}$ , with the materials 1S\_F and 2S showing the higher values. The nanomaterials obtained through the one-step dispersion and two step dispersion procedures showed similar onset potentials, ( $E_{\text{onset}(j=0.1 \text{ mA}\cdot\text{cm}^{-2})} = 0.75 \text{ V vs. RHE}$ ), while the BM\_wos and BM\_ws presented a  $E_{\text{onset}(j=0.1 \text{ mA}\cdot\text{cm}^{-2})}$  value of  $0.79 \text{ V vs. RHE}$ .

Although, these values are lower than those obtained for Pt/C reference ( $j_L = -5.18 \text{ mA}\cdot\text{cm}^{-2}$  and  $E_{\text{onset}(j=0.1 \text{ mA}\cdot\text{cm}^{-2})} = 1.05 \text{ V vs. RHE}$ ), the combination of  $\text{GnP}$ s with  $\text{MoS}_2$  allowed to obtain  $\text{MoS}_2@GnP$  nanocomposites with improved electrocatalytic performances when compared with the starting materials, as indicated by the higher current densities and more positive  $E_{\text{onset}}$  values obtained.

Table 4. ORR electrocatalytic parameters obtained:  $j_L$ ,  $E_{\text{onset}}$ , and  $\tilde{n}_{\text{O}_2}$  values, for pristine MoS<sub>2</sub>, GnPs, N-GnPs, MoS<sub>2</sub>@GnP nanocomposites (1S\_E, 1S\_F, 2S, BM\_wos, BM\_ws, 1S\_F(9:1), 1S\_F(1:9) and 1S\_F(N-GnP)) and Pt/C.

Sample	$j_L / \text{mA}\cdot\text{cm}^{-2}$	$E_{\text{onset}} / \text{V vs. RHE}$		$\tilde{n}_{\text{O}_2}$
		5 % of $j_{\text{max}}$	$j = 0.1 \text{ mA}\cdot\text{cm}^{-2}$	
GnPs	-1.69	0.74	0.73	2.23
MoS <sub>2</sub>	-1.41	0.70	0.68	2.54
1S_E	-1.79	0.75	0.75	2.14
1S_F	-2.00	0.75	0.75	2.15
2S	-2.00	0.75	0.75	2.24
BM_wos	-1.67	0.79	0.79	1.94
BM_ws	-1.82	0.79	0.79	2.06
1S_F(9:1)	-1.47	0.77	0.76	1.97
1S_F(1:9)	-1.80	0.76	0.76	2.13
N-GnPs	-2.79	0.90	0.95	2.67
1S_F(N-GnP)	-2.53	0.81	0.82	3.00
Pt/C	-5.18	1.02	1.05	3.86

The graphical representations of the estimated number of electrons transferred per O<sub>2</sub> molecule ( $n_{\text{O}_2}$ ) at different potential values and the calculated Tafel plots are depicted Figure 26 **c** and **d**, respectively. The values of  $n_{\text{O}_2}$  for each material were estimated through the Koutecky–Levich (K–L) plots, using the LSVs obtained at different rotation rates (cf. Appendix, section A.2 - Figure 46 and section A.3 - Figure 52, for the LSVs and K-L plots, respectively). Regarding the LSVs obtained at different rotation rates, the increase in  $j_L$  with the rotation rate reveals that the electron transfer reaction is limited by diffusion in all samples. All the prepared MoS<sub>2</sub>@GnP nanocomposites exhibited a similar tendency between them, with the increase of  $n_{\text{O}_2}$  values as the potential became less positive (Figure 26 **c**). This tendency indicates that, for these materials, the  $n_{\text{O}_2}$  values are dependent of the applied potential. According with Table 4, the average number of electrons transferred per O<sub>2</sub> molecule ( $\tilde{n}_{\text{O}_2}$ ) for the 2D nanocomposites are in the range from 1.94 to 2.24 electrons, *i.e.* are close to 2 electrons, thus suggesting that in these nanocomposites the ORR occurs by the indirect 2-electron reduction pathway. The

results indicated that, in general, the  $\tilde{n}_{O_2}$  values for the nanocomposites are slightly lower than those obtained for the starting materials ( $\tilde{n}_{O_2} = 2.23$  and  $2.54$  electrons for GnPs and MoS<sub>2</sub>, respectively). Despite this fact, the nanocomposites exhibited higher  $j_L$  and  $E_{onset}$  values. Thus, a fine tuning of the preparation procedure of the hybrid materials may help in the optimization of the  $n_{O_2}$  parameter. As expected, the benchmarking Pt/C electrocatalyst demonstrated the highest  $\tilde{n}_{O_2}$  value ( $3.86$  electrons), thus pointing to a higher selectivity for the direct 4-electron pathway than the prepared nanocomposites.

Through the LSVs represented in Figure 26 **b** it was possible to perform the representation of the Tafel plots and the respective extraction of TS, Figure 26 **d**. In the range from  $0.70$  to  $0.88$  V vs. RHE, the TS obtained for GnPs, MoS<sub>2</sub>, 1S\_E, 1S\_F, 2S, BM\_wos, BM\_ws and Pt/C were  $39$ ,  $58$ ,  $47$ ,  $51$ ,  $25$ ,  $21$ ,  $54$  and  $113$  mV·dec<sup>-1</sup>, respectively. The low TS values obtained for the nanocomposites suggest that the global reaction rate is highly dependent on the conversion step of the intermediate specie MOO<sup>-</sup> to MOOH on the surface, with M corresponding to an empty site on the material surface.<sup>85, 131</sup> On the other hand, the Pt/C showed a higher value, which indicates a different reaction mechanism, where the reaction rate should be determined by the consumption of the MOOH species or by the first discharge step.<sup>131</sup>

Overall, the nanocomposites obtained by the different methodologies tested showed similar electrocatalytic parameters, indicating a minor influence of the preparation method on the ORR electrocatalytic performance. Considering the morphologies of the obtained materials, the ORR electrochemical results and the simplicity of the fabrication method, the method b) of the one-step dispersion procedure was selected for the fabrication of further nanocomposites used in this work. Thus, the evaluation of the influence of other parameters (i.e., mass ratio of the initial components and heteroatom doping of GnPs) on the ORR electroactivity was performed for MoS<sub>2</sub>@GnP nanocomposites prepared following the same preparation method used for 1S\_F.

## II. *Influence of different mass ratios between building blocks*

To evaluate the influence of the mass ratio between building blocks, two novel nanocomposites from the 1S\_F family were fabricated: one having a mass ratio of 90 % GnPs and 10 % MoS<sub>2</sub>, designated as 1S\_F(9:1) and the other with the inverse mass ratio, named 1S\_F(1:9). Noteworthy, the original nanocomposite, named only as 1S\_F, was synthesized using 50 % of GnPs and 50 % of MoS<sub>2</sub>, thus presenting a mass ratio of 1:1. The results obtained are shown in Figure 27 and Table 4. According with CVs obtained in O<sub>2</sub>-saturated electrolyte, the 1S\_F(9:1) material displayed two cathodic

peaks at 0.65 and 0.75 V vs. RHE, while the 1S\_F(1:9) showed two peaks at 0.60 and 0.72 V vs. RHE. The LSVs obtained revealed that, in comparison with original 1S\_F, the 1S\_F(9:1) and 1S\_F(1:9) nanocomposites displayed lower  $j_L$  values (-1.47 and -1.80 mA·cm<sup>-2</sup>, respectively), while the  $E_{\text{onset}}(j = 0.1 \text{ mA}\cdot\text{cm}^{-2})$  values were similar (0.76 V vs. RHE). Concerning the estimated  $\tilde{n}_{\text{O}_2}$ , a small decrease in the values was found compared to the 1S\_F material,  $\tilde{n}_{\text{O}_2} = 1.97$  and 2.13 for 1S\_F(9:1) and 1S\_F(1:9), respectively (cf. Appendix, section A.2 - Figure 47 and section A.3 - Figure 53, for the LSVs obtained at different rotation rates and K-L plots, respectively). Furthermore, both nanocomposites exhibited selectivity towards the indirect 2-electron O<sub>2</sub> reduction pathway. The 1S\_F(9:1) and 1S\_F(1:9) nanocomposites showed TS of 51 and 52 mV·dec<sup>-1</sup>, very similar to that of 1S\_F (52 mV·dec<sup>-1</sup>), also suggesting that no variation in the ORR catalytic mechanism occurred with the change of the components proportions. Overall, no relevant improvement was observed, thus seemingly pointing to a lack of correlation between the ORR electrocatalytic performance and the mass ratio of components used in the preparation of the 1S\_F nanocomposite. Therefore, the mass ratio MoS<sub>2</sub>:GnPs was fixed at 1:1 for further studies.

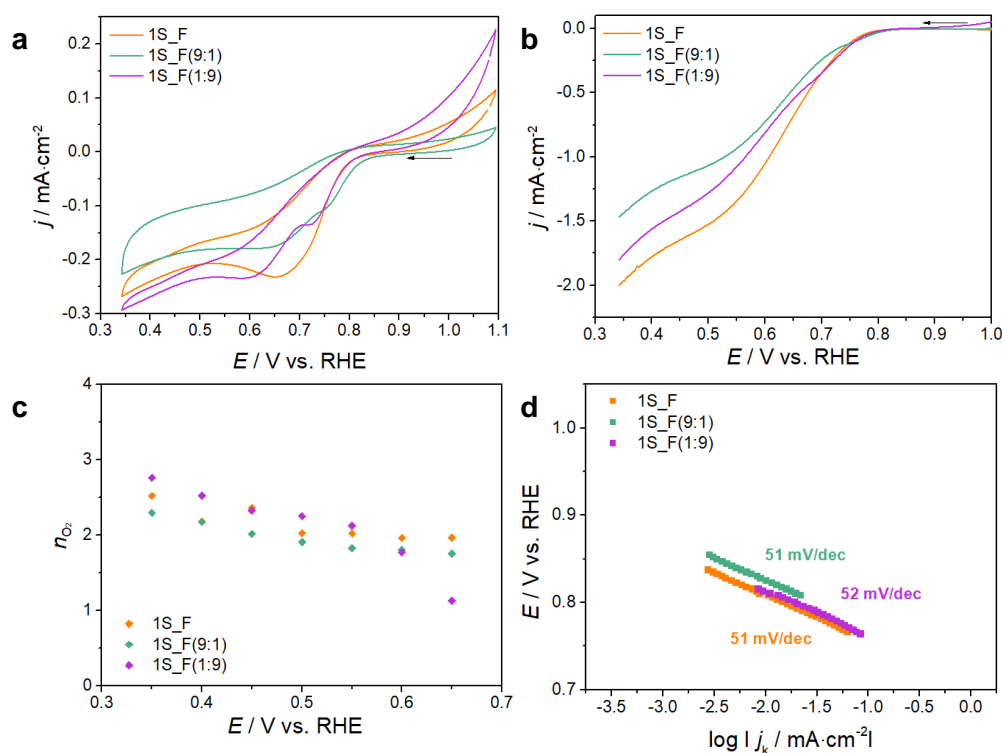


Figure 27. ORR electrocatalytic results for 1S\_F, 1S\_F(9:1) and 1S\_F(1:9) MoS<sub>2</sub>@GnP nanocomposites: **a** CVs (O<sub>2</sub>-saturated 0.1 mol·dm<sup>-3</sup> KOH,  $\nu = 0.005 \text{ V}\cdot\text{s}^{-1}$ ); **b** LSVs (O<sub>2</sub>-saturated 0.1 mol·dm<sup>-3</sup> KOH,  $\nu = 0.005 \text{ V}\cdot\text{s}^{-1}$ ,  $\omega = 1600 \text{ rpm}$ ); **c**  $n_{\text{O}_2}$  estimated at different potential values; **d** Tafel plots with the respective TS values.

### III. Influence of nitrogen doping on GnPs

As mentioned in section 1.1.3, the heteroatom doping of carbon nanomaterials can be beneficial, enhancing their catalytic properties. Therefore, in order to improve the electrocatalytic performance resultant from the MoS<sub>2</sub> and GnPs combination, GnPs were doped with melamine as a precursor of nitrogen atoms. The nanocomposite synthesized from the N-doped GnPs was designated as 1S\_F(N-GnP). The main results of this assessment are shown in Figure 28 and Table 4.

It is expected that the nitrogen doping contributed positively to enhance the electrocatalytic performance of the original GnPs, since doped carbon nanomaterials typically have a higher reactivity.<sup>108-110</sup> When the electrolyte was O<sub>2</sub>-saturated, cathodic peak at 0.79 V vs. RHE was identified for the N-GnPs. Compared to pristine GnPs, N-GnPs showed an increase in current density (from  $j_L = -1.69$  to  $-2.79$  mA·cm<sup>-2</sup>), the onset potential shifted to more positive values (from 0.73 to 0.95 V vs. RHE) and the  $\tilde{n}_{O_2}$  values increased from 2.23 to 2.67 electrons (cf. Appendix, section A.2 - Figure 48 **a** and section A.3 - Figure 54 **a**, for the LSVs obtained at different rotation rates and K-L plots, respectively). N-GnPs showed higher TS values (109 mV·dec<sup>-1</sup>) when compared with pristine GnPs, implying that the reaction rate will be determined by the consumption of the MOOH species on the surface or the first discharge step, more similarly with the Pt/C reference. Overall, the N-doping allowed to improve the ORR electrocatalytic performance of the GnPs.

Furthermore, the N-doping of GnPs also contributed for the development of MoS<sub>2</sub>@GnP nanocomposites with more promising performances. Briefly, the 1S\_F(N-GnP) showed two cathodic peaks at 0.65 V and 0.74 V vs. RHE (in CVs obtained in O<sub>2</sub>-saturated electrolyte), a current density of  $j_L = -2.53$  mA·cm<sup>-2</sup> and a  $E_{\text{onset}(j = 0.1 \text{ mA}\cdot\text{cm}^{-2})} = 0.82$  V vs. RHE (according with the obtained LSVs), a  $\tilde{n}_{O_2} = 3.00$  electrons and a TS = 72 mV·dec<sup>-1</sup>. The value of  $\tilde{n}_{O_2} = 3.00$  electrons achieved (cf. Appendix, section A.2 - Figure 48 **b** and section A.3 - Figure 54 **b**, for the LSVs obtained at different rotation rates and K-L plots, respectively) suggests that the O<sub>2</sub> reduction reaction follows a mixed 2- and 4-electron reduction pathways in this nanocomposite.<sup>85</sup>

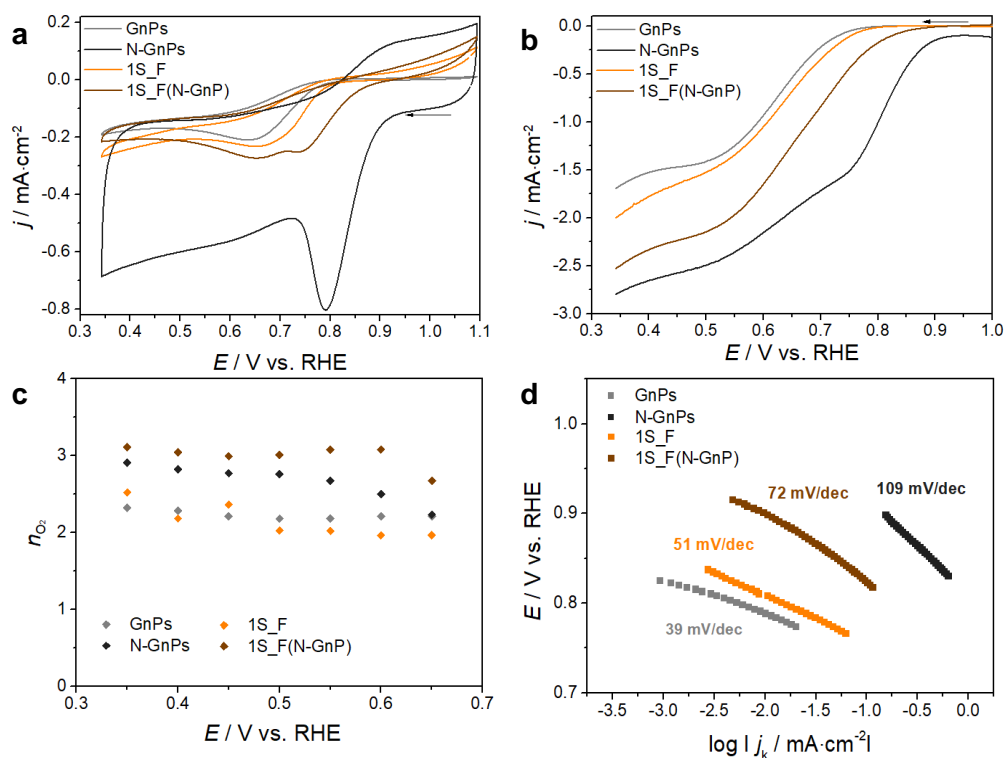


Figure 28. ORR electrocatalytic results for the building blocks GnPs and N-GnPs and MoS<sub>2</sub>@GnP nanocomposites 1S\_F and 1S\_F(N-GnP): **a** CVs (O<sub>2</sub>-saturated 0.1 mol·dm<sup>-3</sup> KOH,  $\nu = 0.005 \text{ V}\cdot\text{s}^{-1}$ ); **b** LSVs (O<sub>2</sub>-saturated 0.1 mol·dm<sup>-3</sup> KOH,  $\nu = 0.005 \text{ V}\cdot\text{s}^{-1}$ ,  $\omega = 1600 \text{ rpm}$ ); **c**  $n_{\text{O}_2}$  estimated at different potential values; **d** Tafel plots with the respective TS values.

### 3.2.1.2. (MoS<sub>2</sub>@GnP)@MWNT nanocomposites

#### I. Influence of the preparation method

The study of the ORR electrocatalytic activity for the 3D nanocomposites similarly started with the analysis of the impact of the preparation method on the electrocatalytic performance. The set of results corresponding to the (MoS<sub>2</sub>@GnP)@MWNT nanocomposites are presented in Figure 29 and Table 5, together with the results obtained for MWNTs and Pt/C.

From the CVs obtained, it was observed that all the 3D nanocomposites exhibited ORR electrocatalytic activity in O<sub>2</sub>-saturated solutions, similar to the 2D nanocomposites. The ORR cathodic peak appears at  $E_{\text{pc}} = 0.78, 0.73, 0.71, 0.68, 0.55$  and  $0.62 \text{ V vs. RHE}$  for MWNT, 1S\_E@MWNT, 1S\_F@MWNT, 2S@MWNT, BM\_wos@MWNT and BM\_ws@MWNT, respectively. As in the case of the 2D MoS<sub>2</sub>@GnP counterparts, all the obtained  $E_{\text{pc}}$  values are less positive than the  $E_{\text{pc}}$  of Pt/C ( $E_{\text{pc}} = 0.75 \text{ V}$ ). In comparison with the results for the 2D nanocomposites, there is a significant positive shift in the  $E_{\text{pc}}$  values for the 3D materials except for the nanocomposites obtained by the ball milling preparation method (BM\_wos@MWNT and BM\_ws@MWNT).

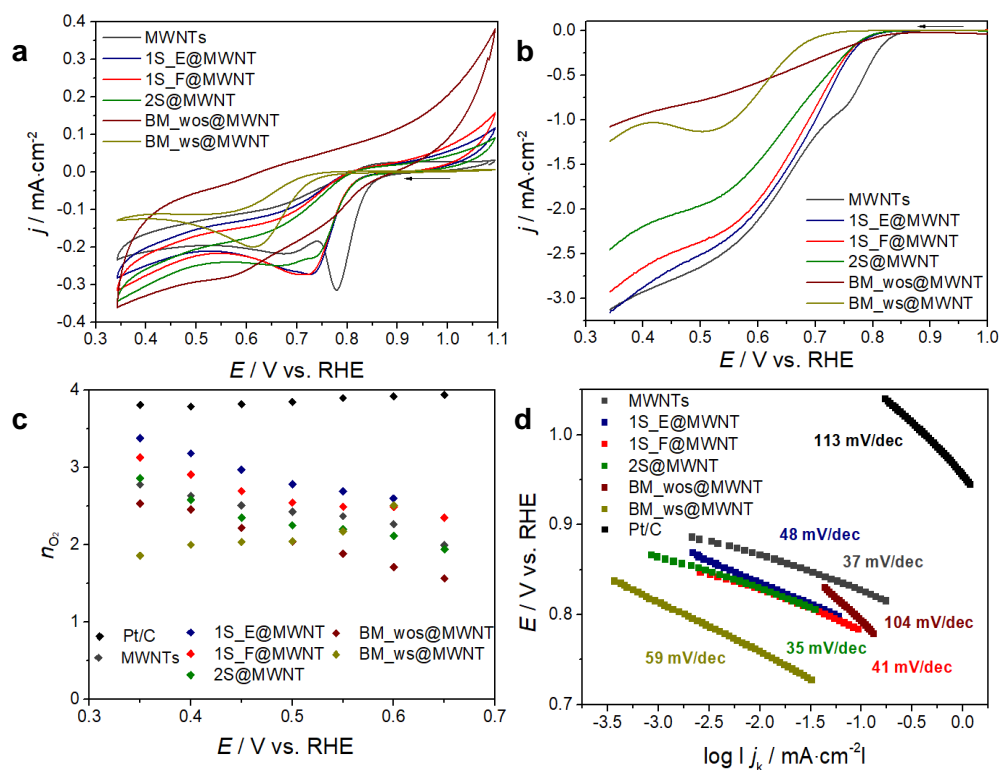


Figure 29. ORR electrocatalytic results for MWNTs, (MoS<sub>2</sub>@GnP)@MWNT nanocomposites (1S\_E@MWNT, 1S\_F@MWNT, 2S, BM\_wos@MWNT and BM\_ws@MWNT), and Pt/C: **a** CVs (O<sub>2</sub>-saturated 0.1 mol·dm<sup>-3</sup> KOH,  $\nu = 0.005$  V·s<sup>-1</sup>); **b** LSVs (O<sub>2</sub>-saturated 0.1 mol·dm<sup>-3</sup> KOH,  $\nu = 0.005$  V·s<sup>-1</sup>,  $\omega = 1600$  rpm); **c**  $n_{O_2}$  estimated at different potential values; **d** Tafel plots with the respective TS values.

Through Table 5, it can be observed that the incorporation of MWNTs improved the ORR catalytic performance of the MoS<sub>2</sub>@GnP heterostructures. In this study, the 3D materials produced by the one step dispersion (method a) and b)) and the two step dispersion procedures presented more positive  $E_{onset}$  values and higher values of  $j_L$  and  $\tilde{n}_{O_2}$  (cf. Appendix, section A.2 - Figure 49 and section A.3 - Figure 55, for the LSVs obtained at different rotation rates and K-L plots, respectively).

Within the three nanocomposites obtained by the one-step dispersion and two-step dispersion paths, the 1S\_E@MWNT and 1S\_F@MWNT nanocomposites can be highlighted. Both exhibit  $j_L \approx 3.00$  mA·cm<sup>-2</sup>, similar  $E_{onset}$  values ( $E_{onset}(j = 0.1 \text{ mA}\cdot\text{cm}^{-2}) = 0.79$  and 0.78 V vs. RHE for 1S\_E@MWNT and 1S\_F@MWNT, respectively) and  $\tilde{n}_{O_2}$  values close to 3. The  $n_{O_2}$  values are dependent on the applied potential and, likewise for the 2D nanocomposites (section 3.2.1.1), there is an increase of  $n_{O_2}$  values as the potential becomes less positive.

The TS (Figure 29 d) for MWNTs, 1S\_E@MWNT, 1S\_F@MWNT, 2S@MWNT, BM\_wos@MWNT and BM\_ws@MWNT are 37, 48, 41, 35, 104 and 59 mV·dec<sup>-1</sup>,

respectively. Except for the BM\_wos@MWNT material, the results pointed to a similar reaction mechanism between them.

Table 5. ORR electrocatalytic parameters obtained:  $j_L$ ,  $E_{\text{onset}}$ , and  $\tilde{n}_{\text{O}_2}$ , for MWNTs, (MoS<sub>2</sub>@GnP)@MWNT nanocomposites (1S\_E@MWNT, 1S\_F@MWNT, 2S, BM\_wos@MWNT and BM\_ws@MWNT, 1S\_F@MWNT (1:3), 1S\_F(N-GnP)@MWNT (1:3) and 1S\_F(N-GnP)@MWNT (3:1)) and Pt/C.

Sample	$j_L / \text{mA}\cdot\text{cm}^{-2}$	$E_{\text{onset}} / \text{V vs. RHE}$		$\tilde{n}_{\text{O}_2}$
		5 % of $j_{\text{max}}$	$j = 0.1 \text{ mA}\cdot\text{cm}^{-2}$	
MWNTs	-3.13	0.82	0.83	2.43
1S_E@MWNT	-3.16	0.77	0.79	2.85
1S_F@MWNT	-2.95	0.77	0.78	2.66
2S@MWNT	-2.45	0.78	0.78	2.33
BM_wos@MWNT	-1.08	0.82	0.79	2.06
BM_ws@MWNT	-1.24	0.71	0.69	2.10
1S_F@MWNT (1:3)	-3.61	0.81	0.83	2.88
1S_F(N-GnP)@MWNT (1:3)	-3.23	0.81	0.82	2.70
1S_F(N-GnP)@MWNT (3:1)	-3.75	0.85	0.86	3.15
Pt/C	-5.18	1.02	1.05	3.86

It is relevant to note that although the MWNTs have, overall, a better electrocatalytic performance than the prepared nanocomposites, the 1S\_E@MWNT and 1S\_F@MWNT materials showed  $j_L$  values close to the values obtained for the MWNTs, while exhibiting higher  $\tilde{n}_{\text{O}_2}$  values and, hence, there was an improvement towards the 4-electron mechanism of ORR. A fine tuning of the building method could be the key to improve further these results.

Considering the obtained results, it can be concluded that the production of the nanocomposite (MoS<sub>2</sub>@GnP)@MWNT via ball milling is not a suitable option for an improved ORR electrocatalytic activity. There was no positive effect with the presence of MWNTs in BM\_wos@MWNT and BM\_ws@MWNT materials. On the other hand, the preparation via SALPE (one-step dispersion and two-step dispersion procedures) seems to be an adjustable route to enhance the performance of these complex nanocomposites. Thus, similar to the preparation of the MoS<sub>2</sub>@GnP materials, method b) of the one-step dispersion procedure was selected for the preparation of further 3D materials in this

work, due to the promising results exhibited by the 1S\_F@MWNT material and because it is a cost-effective and time-saving methodology.

## II. *Influence of different mass ratios between building blocks*

Examination of the mass ratio influence in the overall ORR electrocatalytic performance was also performed for the 3D nanocomposites. In this case, the original materials of (MoS<sub>2</sub>@GnP)@MWNT were originated from a 3:1 ratio of (MoS<sub>2</sub>@GnP):MWNTs. Here, a nanocomposite with an inverse mass ratio was prepared and named 1S\_F@MWNT (1:3). The results obtained are depicted in Figure 30 and Table 5.

According with the CVs obtained in O<sub>2</sub>-saturated electrolyte, 1S\_F@MWNT (1:3) showed an ORR cathodic peak at 0.75 V vs. RHE (Figure 30 a). The use of a 1:3 mass ratio of MoS<sub>2</sub>@GnP:MWNTs contributed to a significant increase in diffusion currents and a more positive onset potential ( $j_L = -3.61 \text{ mA}\cdot\text{cm}^{-2}$  and  $E_{\text{onset}(j = 0.1 \text{ mA}\cdot\text{cm}^{-2})} = 0.83 \text{ vs. RHE}$ ), in comparison with the original 1S\_F@MWNT. The estimated  $\tilde{n}_{\text{O}_2}$  for the new nanocomposite is also close to 3 ( $\tilde{n}_{\text{O}_2} = 2.88$ ), and the tendency of the obtained  $n_{\text{O}_2}$  values with the applied potential was more constant when compared with the 1S\_F@MWNT material (cf. Appendix, section A.2 - Figure 50 and section A.3 - Figure 56, for the LSVs obtained at different rotation rates and K-L plots, respectively).

While the 1S\_F@MWNT composite showed a lower performance than the MWNTs, the new 3D nanocomposite showed a slightly improved ORR activity. The results obtained are in agreement with what might be expected, since increasing the quantity of MWNTs should in principle lead to an overall enhancement of the electrocatalytic performance. It is relevant to note that the performance not only equaled that of the MWNTs, but also slightly exceeded it in some parameters, such as  $j_L$  and  $\tilde{n}_{\text{O}_2}$ .

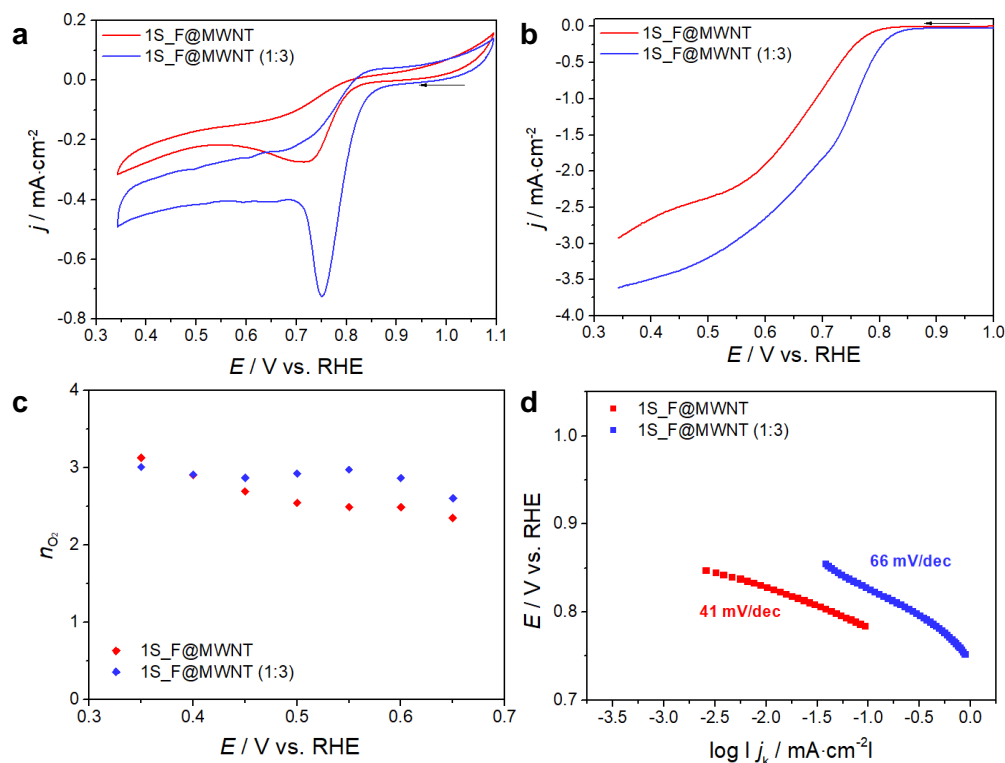


Figure 30. ORR electrocatalytic results for the  $(\text{MoS}_2@\text{GnP})@\text{MWNT}$  nanocomposites ( $1\text{S\_F@MWNT}$  and  $1\text{S\_F@MWNT (1:3)}$ ): **a** CVs ( $\text{O}_2$ -saturated  $0.1 \text{ mol}\cdot\text{dm}^{-3}$  KOH,  $\nu = 0.005 \text{ V}\cdot\text{s}^{-1}$ ); **b** LSVs ( $\text{O}_2$ -saturated  $0.1 \text{ mol}\cdot\text{dm}^{-3}$  KOH,  $\nu = 0.005 \text{ V}\cdot\text{s}^{-1}$ ,  $\omega = 1600 \text{ rpm}$ ); **c**  $n_{\text{O}_2}$  estimated at different potential values; **d** Tafel plots with the respective TS values.

Nonetheless, a careful rationalization of the proportion of these two components is necessary, since it was reported that an excess amount of MWNTs may induce a reduction in the electrocatalytic performance. For a nanocomposite formed by  $\text{MoS}_2$  and MWNTs, Lee *et al.*<sup>43</sup> reported that the addition of CNTs improves the ORR catalytic activity. However, a linear correlation between the CNTs loading and the ORR performance was not observed, and a decline in electrocatalytic behavior was observed after reaching an optimization peak.

### III. Influence of nitrogen doping on GnPs

The last optimization addressed was the insertion of N-GnPs into the three-dimensional structure. Since a beneficial effect was demonstrated with the N-doping of GnPs in the 2D nanocomposites, a 3D nanocomposite was produced, analogous to the promising  $1\text{S\_F@MWNT (1:3)}$  but using N-GnPs instead of pristine GnPs. This material was named as  $1\text{S\_F@MWNT(N-GnP) (1:3)}$ .

Contrary to expectations, the N-doping of GnPs did not contribute significantly to enhance the electrocatalytic  $\text{O}_2$  reduction process of the  $1\text{S\_F@MWNT(N-GnP) (1:3)}$  nanocomposite (Figure 31 and Table 5). As shown in Figure 31 **a**, a cathodic peak was

identified for the 1S\_F@MWNT(N-GnP) (1:3) material at 0.74 V vs. RHE. Overall, for this material the electrocatalytic parameters remains similar to those achieved for the analogous non-doped GnPs (1S\_F@MWNT (1:3),  $j_L = -3.23 \text{ mA}\cdot\text{cm}^{-2}$ ,  $E_{\text{onset}(j=0.1 \text{ mA}\cdot\text{cm}^{-2})} = 0.83 \text{ V vs. RHE}$  and  $\tilde{n}_{\text{O}_2} = 2.70$  electrons), indicating a similar ORR electrocatalytic activity (cf. Appendix, section A.2 - Figure 51 **a** and section A.3 - Figure 57 **a**, for the LSVs obtained at different rotation rates and K-L plots, respectively). A possible explanation for that is the higher amount of MWNTs relatively to the amount of MoS<sub>2</sub>@N-GnPs counterpart used. In these conditions, the impact of the doping may have been mitigated by the higher fraction of MWNTs, overshadowing the effect for this 3D nanocomposite. Therefore, a new nanocomposite with N-GnPs but an inverse mass ratio (3:1), similar to the 3D materials fabricated initially, was tested. This nanocomposite was classified as 1S\_F(N-GnP)@MWNT (3:1).

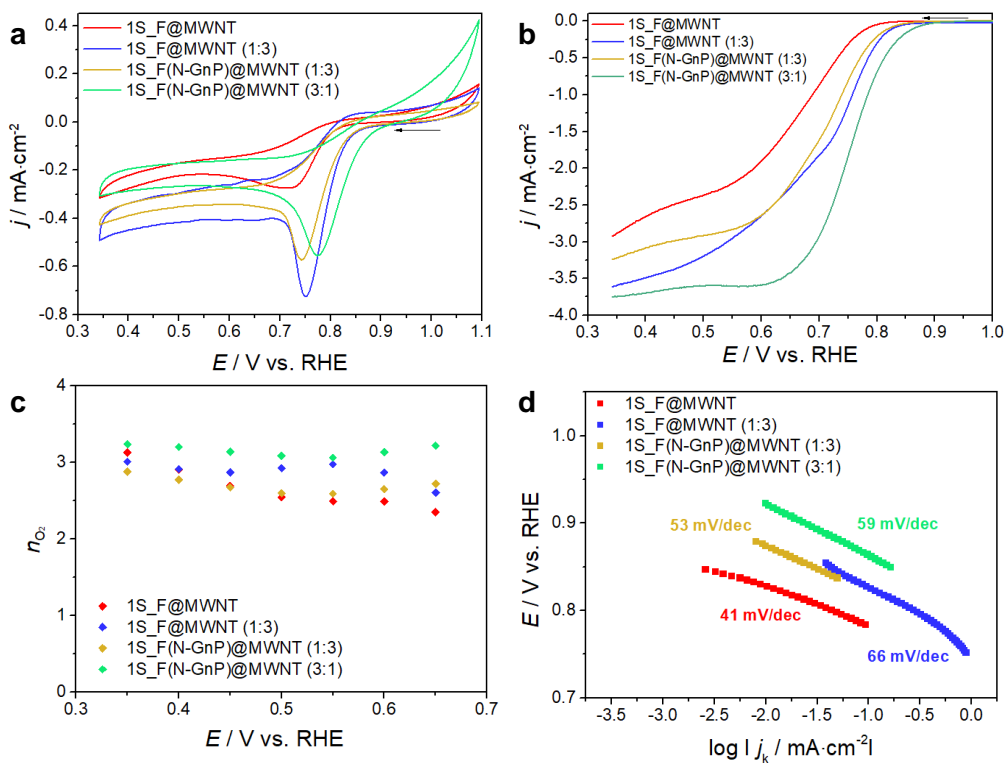


Figure 31. ORR electrocatalytic results for the (MoS<sub>2</sub>@GnP)@MWNT nanocomposites (1S\_F@MWNT, 1S\_F@MWNT (1:3), 1S\_F(N-GnP)@MWNT (1:3) and 1S\_F(N-GnP)@MWNT (3:1)): **a** CVs (O<sub>2</sub>-saturated 0.1 mol·dm<sup>-3</sup> KOH,  $\nu = 0.005 \text{ V}\cdot\text{s}^{-1}$ ); **b** LSVs (O<sub>2</sub>-saturated 0.1 mol·dm<sup>-3</sup> KOH,  $\nu = 0.005 \text{ V}\cdot\text{s}^{-1}$ ,  $\omega = 1600 \text{ rpm}$ ); **c**  $n_{\text{O}_2}$  estimated at different potential values; **d** Tafel plots with the respective TS values.

In this case, the CV obtained in O<sub>2</sub>-saturated electrolyte for the 1S\_F(N-GnP)@MWNT (3:1) material displayed a cathodic peak at 0.77 V vs. RHE. In addition,

the N-doping of GnPs allowed an increase in current densities ( $j_L = -3.75 \text{ mA}\cdot\text{cm}^{-2}$ ) and the shift of  $E_{\text{onset}}(j = 0.1 \text{ mA}\cdot\text{cm}^{-2})$  to more positive values (to 0.86 V vs. RHE). The estimated  $n_{\text{O}_2}$  were almost independent of the applied potential, and the  $\tilde{n}_{\text{O}_2}$  value increased to 3.15, getting closer to the value obtained for Pt/C (cf. Appendix, section A.2 - Figure 51 **a** and section A.3 - Figure 57 **b**, for the LSVs obtained at different rotation rates and K-L plots, respectively). The results suggested that there is indeed a beneficial effect of N-doping on GnPs for the ORR electrocatalytic activity. Compared with the non-doped counterpart 1S\_F@MWNT, the 1S\_F(N-GnP)@MWNT (3:1) nanocomposite exhibited a remarkable ORR electrocatalytic behavior. These results are encouraging and pave the way for future optimizations of these 3D nanocomposites, considering the ideal direct 4-electron reduction pathway.

### 3.2.1.2. Chronoamperometry assays

The analysis of ORR electrocatalytic long-term stability and resistance to methanol was also performed. These two factors are also important for the selection of a promising electrocatalyst, since poor stability and strong sensitivity to methanol can induce complications in the electrocatalytic performance of the catalyst, mainly considering a practical application. Figure 32 shows the  $i$ - $t$  response curves obtained during the long-term stability and methanol resistance assays. The materials 1S\_F, 1S\_F(N-GnP), 1S\_F@MWNT (1:3) and 1S\_F(N-GnP)@MWNT (3:1) were selected considering their similar preparation method (in this case, method b) of the one-step dispersion procedure) and due to the most promising electrocatalytic performance obtained.

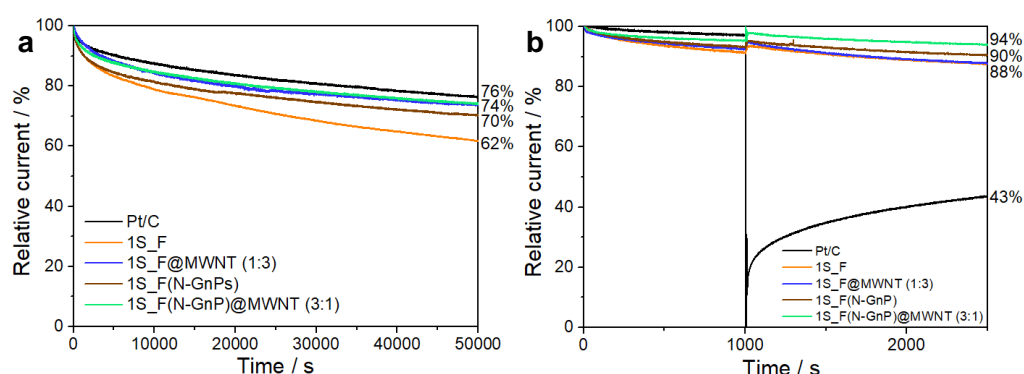


Figure 32.  $i$ - $t$  response curves obtained during **a** the stability studies and **b** the methanol resistance tests for selected 2D MoS<sub>2</sub>@GnP nanocomposites (1S\_F and 1S\_F(N-GnP)) and 3D (MoS<sub>2</sub>@GnP)@MWNT nanocomposites (1S\_F@MWNT (1:3) and 1S\_F(N-GnP)@MWNT (3:1)), and for Pt/C reference.  $E_{\text{applied}} = 0.54 \text{ V}$  vs. RHE and  $\omega = 1600 \text{ rpm}$  during 50000 s, in O<sub>2</sub>-saturated 0.1 mol·dm<sup>-3</sup> KOH; in **b** addition of 0.5 mol·dm<sup>-3</sup> methanol at 1000 s.

Concerning the long-term electrochemical stability assay, after a period of 50000 s, all the tested materials showed current retentions between 62 % and 74 %. Among the laminar nanocomposites, the doping of GnPs allowed an improvement in the overall stability, with a current retention increase from 68 % (for 1S\_F) to 70 % (for 1S\_F(N-GnP)). The presence of MWNTs improved the stability of the aforementioned nanocomposites, presenting a current retention of 74 % for the 3D materials 1S\_F@MWNT (1:3) and 1S\_F(N-GnP)@MWNT (3:1). It is relevant to note that the N-doping of GnPs had only a slight influence on the 3D nanocomposite, suggesting that the stability of these three-dimensional materials is mainly ruled by MWNTs. Pt/C was the material with a higher current retention, 76 %, however the nanocomposites displayed values close to this benchmark electrocatalyst.

Regarding methanol resistance, the results presented in Figure 32 **b**, showed that all the prepared materials did not experienced an abrupt decrease in current retentions after the methanol addition, keeping 88 % of current for 1S\_F and 1S\_F@MWNT (1:3), 90 % for 1S\_F(N-GnP) and 94 % for 1S\_F(N-GnP)@MWNT (3:1). However, with the Pt/C reference a significant drop in current retention was observable with the methanol addition (43 % of current retention), which indicates its known high selectivity for the methanol oxidation that in turn subdues the ORR.<sup>94, 96</sup> The prepared nanocomposites showed higher current retentions than Pt/C, suggesting a better ORR selectivity and lower sensitivity for methanol crossover. Thus, the analyzed electrocatalysts can be more suitable for methanol-based fuel cells than the Pt/C.

Lastly, the measurement of H<sub>2</sub>O<sub>2</sub> production (%H<sub>2</sub>O<sub>2</sub>) was evaluated for these samples using the bipotentiostatic mode. The obtained LSVs at the RRDE ring and disk, as well as the percentages of H<sub>2</sub>O<sub>2</sub> formed with the applied potential are shown in Figure 33. In increasing order, the maximum % H<sub>2</sub>O<sub>2</sub> values obtained were 24 % for 1S\_F(N-GnP), 26 % for 1S\_F(N-GnP)@MWNT (3:1), 46 % for 1S\_F and 53 % for 1S\_F@MWNT (1:3).

Ideally, the results obtained by this method should correlate with the  $\tilde{n}_{O_2}$  values obtained through K-L plots, *i.e.*, materials that have a selectivity for an indirect 2-electron pathway should present higher % of H<sub>2</sub>O<sub>2</sub> production than a material with a selectivity for the direct 4-electron pathway. However, in this case, the calculated values are not consistent with what was previously estimated by the K-L plots.

Although the nanocomposites with non-doped GnPs (1S\_F(N-GnP) and 1S\_F(N-GnP)@MWNT (3:1)) showed higher H<sub>2</sub>O<sub>2</sub> production percentages than the nanocomposites with the N-GnPs (1S\_F and 1S\_F@MWNT (1:3)), a similar tendency could not be observed when there was addition of MWNTs. In this case, the results suggest that there is an increase on the % H<sub>2</sub>O<sub>2</sub> production values for the 3D nanocomposites, when compared to the laminar composites. As noted in section 3.2.1.1, through K-L plots, the 3D nanocomposites showed higher  $\tilde{n}_{O_2}$  values than those presented for the laminar composites. Thus, the three-dimensional materials should have lower % of H<sub>2</sub>O<sub>2</sub> produced, since they seemed to be less selective for the indirect 2-electron pathway.

The inconsistencies may be explained by the issues presented by this measurement method. The RRDE measurement method depends on some experimental factors, such as the morphology of the sample and the properties of the electrode itself.<sup>132</sup>

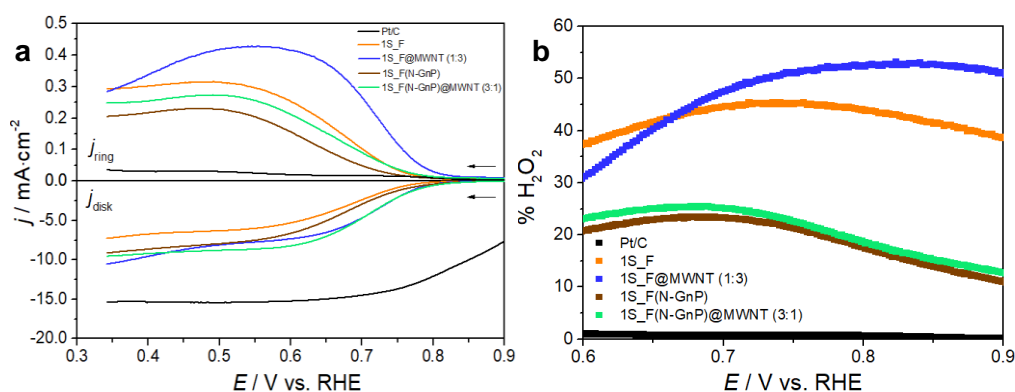


Figure 33. **a** RRDE voltammograms of the MoS<sub>2</sub>@GnP nanocomposites (1S\_F and 1S\_F(N-GnP)), (MoS<sub>2</sub>@GnP)@MWNT (1S\_F@MWNT (1:3) and 1S\_F(N-GnP)@MWNT (3:1)) and Pt/C (O<sub>2</sub>-saturated 0.1 mol·dm<sup>-3</sup> KOH,  $\nu = 0.005$  V·s<sup>-1</sup>, 1600 rpm). **b** Variation of the calculated percentages of H<sub>2</sub>O<sub>2</sub> formed with the applied potential.

### 3.2.2. OER electrocatalytic performance

The OER electrocatalytic performance was evaluated for all fabricated materials. The tests were based on LSV studies, performed at  $\nu = 0.005$  V·s<sup>-1</sup> and 1600 rpm in N<sub>2</sub>-saturated KOH 0.1 mol·dm<sup>-3</sup> electrolyte. The benchmark electrocatalyst used was RuO<sub>2</sub>. Similar to the ORR assays, the results were compiled into two sections regarding the two types of nanocomposites studied (MoS<sub>2</sub>@GnP and (MoS<sub>2</sub>@GnP)@MWNT), each one subdivided into three additional sections.

### 3.2.2.1. MoS<sub>2</sub>@GnP nanocomposites

#### I. Influence of the preparation methods

Figure 34 shows the LSVs and TS plots for the building blocks and the initially prepared laminar nanocomposites. For all the prepared materials, the current density values did not reached the target value of  $j = 10 \text{ mA}\cdot\text{cm}^{-2}$ , thus not making it possible to compare the materials activities according to the values of  $\eta$ , as typically appear in literature.<sup>97</sup> Therefore it was assumed the value of  $j$  at  $E = 1.8 \text{ V}$  vs. RHE ( $j_{1.8}$ ) as parameter to compare the performance of the prepared materials. The obtained values of  $j_{1.8}$  are presented in Table 6.

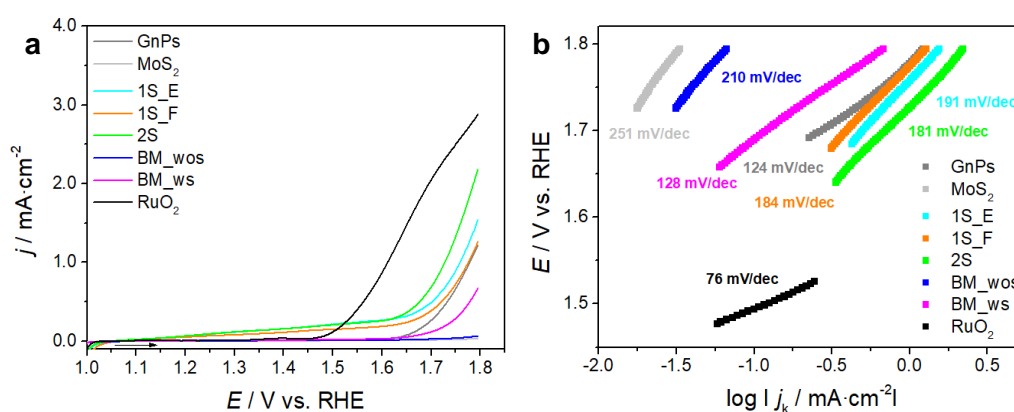


Figure 34. OER electrocatalytic results for the building blocks (pristine MoS<sub>2</sub> and GnPs), MoS<sub>2</sub>@GnP nanocomposites (1S\_E, 1S\_F, 2S, BM\_wos and BM\_ws), and RuO<sub>2</sub>: **a** LSVs (N<sub>2</sub>-saturated 0.1 mol·dm<sup>-3</sup> KOH,  $v = 0.005 \text{ V}\cdot\text{s}^{-1}$ ,  $\omega = 1600 \text{ rpm}$ ); **b** Tafel plots with the respective TS values.

It can be observed that pristine MoS<sub>2</sub> presented the worst OER activity, with  $j_{1.8} = 0.03 \text{ mA}\cdot\text{cm}^{-2}$ . For the MoS<sub>2</sub>@GnP nanocomposites, a small OER electrocatalytic activity was observed, mainly for nanocomposites prepared by the ball milling method BM\_wos and BM\_ws, with  $j_{1.8}$  values of 0.07 and 0.67 mA·cm<sup>-2</sup>, respectively. Furthermore, the calculated TS for the tested materials lie between 124 and 251 mVdec<sup>-1</sup>, which are significantly higher than the obtained for the RuO<sub>2</sub> reference (76 mV·dec<sup>-1</sup>). These results indicate a weak OER kinetics of these materials, with the hinder activation of the oxidation mechanism of O<sub>2</sub> molecules and a global low OER electrocatalytic performance (a good electrocatalyst should demonstrate low TS values).

Table 6. OER electrocatalytic parameters,  $j_{1.8}$  and TS, for the building blocks (MoS<sub>2</sub>, GnPs and N-GnPs), MoS<sub>2</sub>@GnP nanocomposites (1S\_E, 1S\_F, 2S, BM\_wos, BM\_ws, 1S\_F(9:1), 1S\_F(1:9) and 1S\_F(N-GnP)), and RuO<sub>2</sub> reference.

Sample	$j_{1.8} / \text{mA}\cdot\text{cm}^{-2}$	TS / $\text{mV}\cdot\text{dec}^{-1}$
GnPs	1.22	124
MoS <sub>2</sub>	0.03	251
1S_E	1.54	191
1S_F	1.26	184
2S	2.18	181
BM_wos	0.07	210
BM_ws	0.67	128
1S_F(9:1)	0.67	215
1S_F(1:9)	0.67	180
N-GnPs	5.39	218
1S_F(N-GnP)	1.48	221
RuO <sub>2</sub>	2.88	76

In summary, it was found that the starting materials and the prepared MoS<sub>2</sub>@GnP nanocomposites showed poor OER electrocatalytic activity. As in the ORR electrochemical studies, method b) of the one-step dispersion procedure was retained as the base procedure for the preparation of the next nanocomposites used in this work.

## II. Influence of different mass ratios between building blocks

The 1S\_F(9:1) and 1S\_F(1:9) nanocomposites were addressed in OER electrocatalytic studies (Figure 35 and Table 6). For both materials, a similar value of  $j_{1.8}$  (0.67 mA·cm<sup>-2</sup>) and high TS values were observed. As in the ORR electrocatalytic assays, the use of higher amounts of one component did not contribute to the enhancement of the electrocatalytic performance.

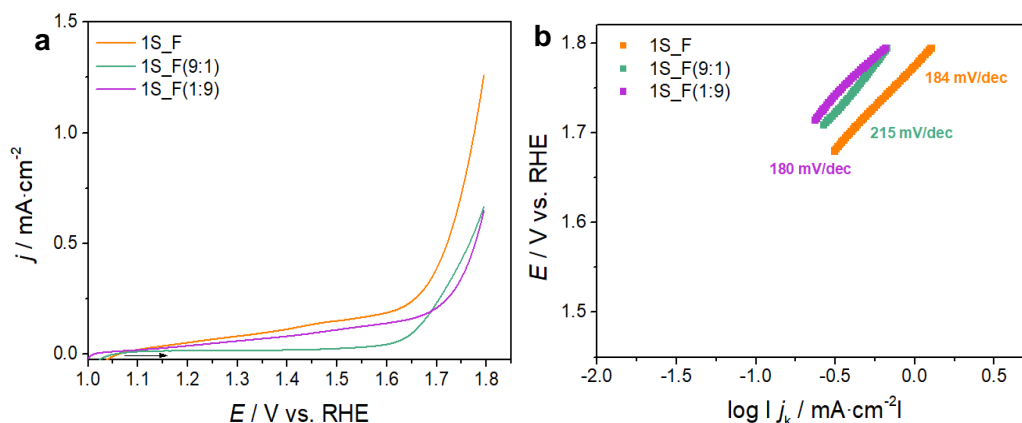


Figure 35. OER electrocatalytic results for the MoS<sub>2</sub>@GnP nanocomposites (1S\_F, 1S\_F(9:1) and 1S\_F(1:9)): **a** LSVs (N<sub>2</sub>-saturated 0.1 mol·dm<sup>-3</sup> KOH,  $\nu = 0.005 \text{ V}\cdot\text{s}^{-1}$ ,  $\omega = 1600 \text{ rpm}$ ); **b** Tafel plots with the respective TS values.

### III. Influence of nitrogen doping on GnPs

The LSVs and Tafel plots of the assays regarding the influence of N-doping of GnPs are shown in Figure 36 and Table 6.

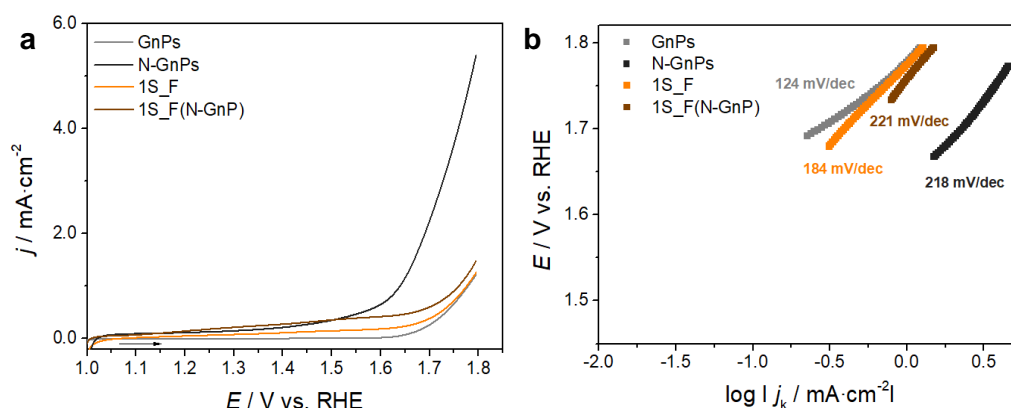


Figure 36. OER electrocatalytic results for the building blocks (GnP and N-GnP) and MoS<sub>2</sub>@GnP nanocomposites (1S\_F and 1S\_F(N-GnP)): **a** LSVs (N<sub>2</sub>-saturated 0.1 mol·dm<sup>-3</sup> KOH,  $\nu = 0.005 \text{ V}\cdot\text{s}^{-1}$ ,  $\omega = 1600 \text{ rpm}$ ); **b** Tafel plots with the respective TS values.

Despite not leading outstanding current densities, the N-doping improved the OER electrocatalytic behavior of the pristine GnPs, increasing the value of  $j_{1.8}$  from 1.22 to 5.39 mA·cm<sup>-2</sup>. However, the positive impact was not satisfactory for the 1S\_F(N-GnP) nanocomposite ( $j_{1.8} = 1.48 \text{ mA}\cdot\text{cm}^{-2}$ ).

The interaction of N-GnPs with MoS<sub>2</sub> appeared to be beneficial in the ORR tests, as it facilitated the unfolding of the reduction reaction compared to the nanocomposite with non-doped GnPs. However, this effect was not observed for OER.

### 3.2.2.2. (MoS<sub>2</sub>@GnP)@MWNT nanocomposites

#### I. Influence of the preparation methods

The initial 3D nanocomposites did not exhibit either current density values greater than 10 mA·cm<sup>-2</sup>, so the  $j_{1.8}$  values were used as a comparison parameter (Figure 37 and Table 7).

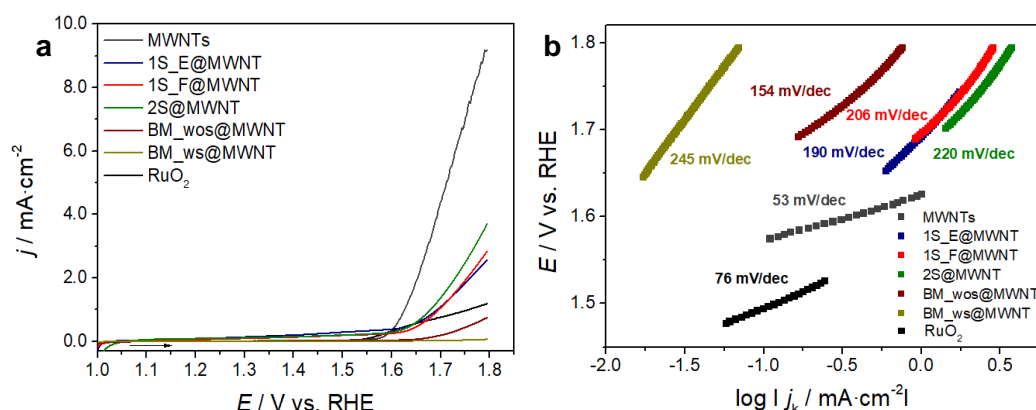


Figure 37. OER electrocatalytic results for the MWNTs, (MoS<sub>2</sub>@GnP)@MWNT nanocomposites (1S\_E@MWNT, 1S\_F@MWNT, 2S, BM\_wos@MWNT and BM\_ws@MWNT), and RuO<sub>2</sub>: **a** LSVs (N<sub>2</sub>-saturated 0.1 mol·dm<sup>-3</sup> KOH,  $\nu = 0.005 \text{ V}\cdot\text{s}^{-1}$ ,  $\omega = 1600 \text{ rpm}$ ); **b** Tafel plots with the respective TS values.

Table 7. OER electrocatalytic parameters,  $j_{1.8}$  and TS, for MWNTs, (MoS<sub>2</sub>@GnP)@MWNT nanocomposites (1S\_E@MWNT, 1S\_F@MWNT, 2S, BM\_wos@MWNT and BM\_ws@MWNT, 1S\_F@MWNT (1:3), 1S\_F(N-GnP)@MWNT (1:3) and 1S\_F(N-GnP)@MWNT (3:1)), and RuO<sub>2</sub> reference.

Sample	$j_{1.8} / \text{mA}\cdot\text{cm}^{-2}$	TS / mV·dec <sup>-1</sup>
MWNTs	9.18	53
1S_E@MWNT	2.57	190
1S_F@MWNT	2.84	206
2S@MWNT	3.71	220
BM_wos@MWNT	0.75	154
BM_ws@MWNT	0.07	245
1S_F@MWNT (1:3)	7.57	109
1S_F(N-GnP)@MWNT (1:3)	7.98	86
1S_F(N-GnP)@MWNT (3:1)	25.0	67
RuO <sub>2</sub>	2.88	76

As can be seen in Table 7, the (MoS<sub>2</sub>@GnP)@MWNT materials demonstrated higher  $j_{1.8}$  values than the starting MoS<sub>2</sub>@GnP nanocomposites ( $j_{1.8(1S\_E@MWNT)} = 1.54 \text{ mA}\cdot\text{cm}^{-2}$ ,  $j_{1.8(1S\_F@MWNT)} = 1.26 \text{ mA}\cdot\text{cm}^{-2}$ ,  $j_{1.8(2S@MWNT)} = 2.18 \text{ mA}\cdot\text{cm}^{-2}$ ,  $j_{1.8(\text{BM\_wos@MWNT})} = 0.07 \text{ mA}\cdot\text{cm}^{-2}$ ,  $j_{1.8(\text{BM\_ws@MWNT})} = 0.67 \text{ mA}\cdot\text{cm}^{-2}$ ). However, the  $j_{1.8}$  values of the 3D nanocomposites were lower than those of pristine MWNTs ( $j_{1.8} = 9.18 \text{ mA}\cdot\text{cm}^{-2}$ ). It is worth noting that for the BM\_wos@MWNT and BM\_ws@MWNT nanocomposites the activity is even lower, also suggesting the need for optimization of the preparation method by ball milling of this type of materials. As previously verified for ORR, the MWNTs contributed to the development of the OER electrocatalytic activity of the 2D composites, although the effect was still quite low.

The calculated TS for the tridimensional nanocomposites ranged from 154 to 220  $\text{mV}\cdot\text{dec}^{-1}$ . As such, the results indicate that the initial (MoS<sub>2</sub>@GnP)@MWNT nanocomposites displayed slow kinetics towards OER.

## II. Influence of different mass ratios between building blocks

The impact of mass ratio was also examined for OER. The corresponding results for 1S\_F@MWNT and 1S\_F@MWNT (1:3) materials can be seen in Figure 38 and Table 7. The composite with a mass ratio of 1:3 (MoS<sub>2</sub>@GnP:MWNTs) provided a relevant increase in OER activity, with an increase in  $j$  values ( $j_{1.8} = 7.57 \text{ mA}\cdot\text{cm}^{-2}$ ) and a reduction in TS values (TS = 109  $\text{mV}\cdot\text{dec}^{-1}$ ). Since the MWNTs outperformed the MoS<sub>2</sub>@GnP nanocomposites, the use of a higher amount of this component may have been a key factor.

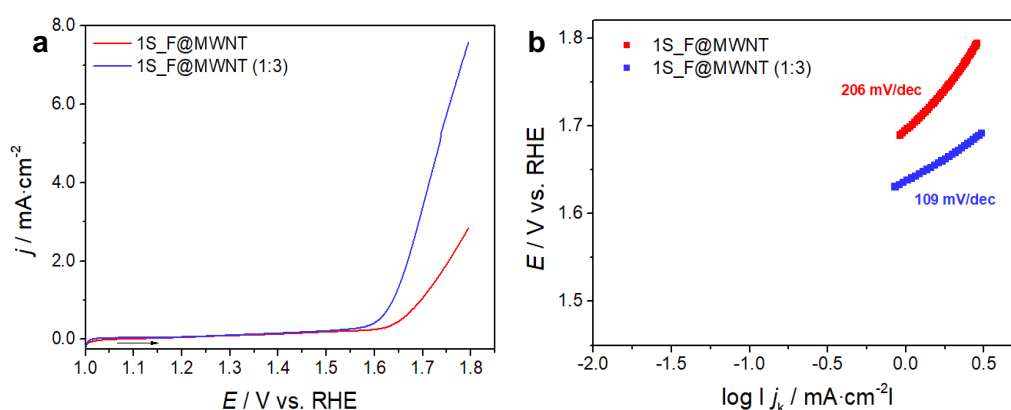


Figure 38. OER electrocatalytic results for the (MoS<sub>2</sub>@GnP)@MWNT nanocomposites (1S\_F@MWNT and 1S\_F@MWNT (1:3)): **a** LSVs (N<sub>2</sub>-saturated 0.1 mol·dm<sup>-3</sup> KOH,  $\nu = 0.005 \text{ V}\cdot\text{s}^{-1}$ ,  $\omega = 1600 \text{ rpm}$ ); **b** Tafel plots with the respective TS values.

### III. Influence of nitrogen doping on GnPs

Lastly, the 3D nanocomposites consisting of MoS<sub>2</sub>@N-GnP and MWNTs, 1S\_F(N-GnP)@MWNT (1:3) and 1S\_F(N-GnP)@MWNT (3:1) were analyzed for OER (Figure 39 and Table 7).

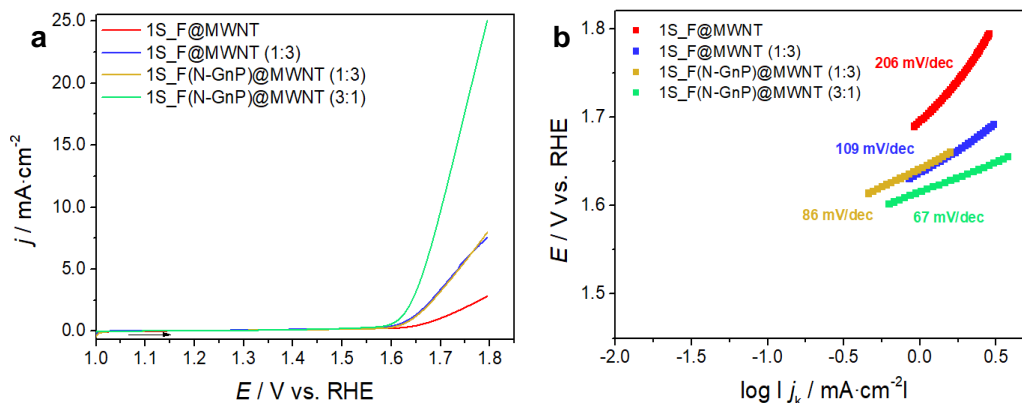


Figure 39. OER electrocatalytic results for the (MoS<sub>2</sub>@GnP)@MWNT nanocomposites (1S\_F@MWNT (1:3), 1S\_F(N-GnP)@MWNT (1:3) and 1S\_F(N-GnP)@MWNT (3:1)): **a** LSVs (N<sub>2</sub>-saturated 0.1 mol·dm<sup>-3</sup> KOH,  $\nu = 0.005 \text{ V}\cdot\text{s}^{-1}$ ,  $\omega = 1600 \text{ rpm}$ ); **b** Tafel plots with the respective TS values.

As observed in the ORR performance analysis, the 1S\_F(N-GnP)@MWNT (1:3) material did not show better performance than the 1S\_F@MWNT (1:3) nanocomposite. On the other hand, a noticeable synergistic effect was identified in the 1S\_F(N-GnP)@MWNT (3:1) electrocatalyst. The material showed more significant properties as an OER electrocatalyst since it has high  $j_{1.8}$  values ( $j_{1.8} = 25.0 \text{ mA}\cdot\text{cm}^{-2}$ ) and a low TS ( $67 \text{ mV}\cdot\text{dec}^{-1}$ ). Given that the current densities exceeded the  $10 \text{ mA}\cdot\text{cm}^{-2}$  barrier, it was possible to calculate the overpotential for 1S\_F(N-GnP)@MWNT (3:1), which was found to be  $\eta_{10 \text{ mA}\cdot\text{cm}^{-2}} = 0.47 \text{ V}$ .

### 3.3. Overview of the electrocatalytic properties of the nanocomposites

Table 8 highlights the results of the materials that showed improved ORR catalytic activity among the prepared and tested MoS<sub>2</sub>@GnP and (MoS<sub>2</sub>@GnP)@MWNT nanocomposites.

In view of the results obtained, five aspects can be highlighted:

**i)** the combination of MoS<sub>2</sub> and GnPs resulted in higher ORR electrocatalytic activity than the demonstrated by each component individually;

- ii) the incorporation of MWNTs improved the ORR electrocatalytic performance of the 3D heterostructure;
- iii) regarding the mass ratio used in the 3D nanocomposites, the use of a higher amount of carbon nanotubes is beneficial when undoped carbon materials are combined;
- iv) the N-doping of GnPs improved the performance of the MoS<sub>2</sub>@GnP nanocomposite;
- v) for the effect of the GnPs N-doping to be prominent in the 3D nanocomposites, the content of MWNTs should be smaller than that of 2D counterpart.

Table 8. ORR electrocatalytic parameters for the most promising materials prepared:  $j_L$ ,  $E_{\text{onset}}$ , and  $\tilde{n}_{\text{O}_2}$ , for the MoS<sub>2</sub>@GnP nanocomposites (1S\_F and 1S\_F(N-GnP)), (MoS<sub>2</sub>@GnP)@MWNT (1S\_F@MWNT (1:3) and 1S\_F(N-GnP)@MWNT (3:1)) and Pt/C.

Sample	$j_L / \text{mA}\cdot\text{cm}^{-2}$	$E_{\text{onset}} / \text{V vs. RHE}$		$\tilde{n}_{\text{O}_2}$
		5 % of $j_{\text{max}}$	$j = 0.1 \text{ mA}\cdot\text{cm}^{-2}$	
1S_F	-2.00	0.75	0.75	2.15
1S_F@MWNT (1:3)	-3.61	0.81	0.83	2.88
1S_F(N-GnP)	-2.53	0.81	0.82	3.00
1S_F(N-GnP)@MWNT (3:1)	-3.75	0.85	0.86	3.15
Pt/C	-5.18	1.02	1.05	3.86

As shown in Table 9, the results obtained for ORR are within the range of values reported for electrocatalysts with similar composition (MoS<sub>2</sub> and carbon nanomaterials).<sup>42, 43, 85, 118, 121</sup> It should also be highlighted that in this study the samples were prepared under milder conditions compared with the examples generally present in literature.

Table 9. Framing with the results reported in current literature regarding nanocomposites prepared from MoS<sub>2</sub> and carbon nanomaterials and applied as ORR electrocatalysts.

Electrocatalyst	Preparation method	$E_{\text{onset}} / \text{V vs. RHE}$ ( $j = 0.1 \text{ mA}\cdot\text{cm}^{-2}$ )	$\tilde{n}_{\text{O}_2}$	Ref.
MoS <sub>2</sub> /MWNTs	Solvothermal	0.64	≈ 4.00	43
MoS <sub>2</sub> /N-Graphene <sup>+</sup>	Solution processing	0.83	3.75 – 3.90	121
N-Graphene/MWNTs <sup>*</sup>	Solvothermal	0.83	≈ 4.00	118
N-Graphene/N-MWNTs <sup>°</sup>	Hydrothermal	0.81	3.30 – 3.70	42
GnPs@MWNTs	Electrostatic-driven solution processing	0.76	2.60	123
MoS <sub>2</sub> @MWNTs	Electrostatic-driven solution processing	0.74	2.87	85
1S_F		0.75	2.15	
1S_F@MWNT (1:3)	Electrostatic-driven solution processing	0.77	2.88	Present Work
1S_F(N-GnP)		0.82	3.00	
1S_F(N-GnP)@MWNT (3:1)		0.86	3.15	

Note: Nitrogen-containing precursors – <sup>+</sup> hydrazine hydrate, <sup>\*</sup> biuret, <sup>°</sup> ammonia.

Regarding the catalytic OER performance, the results of the respective materials are summarized in Table 10. The MoS<sub>2</sub>@GnP nanocomposites provided low current densities compared to the 3D nanocomposites. Even though they are electrocatalysts of minor significance in OER, the rigorous combination of the three components optimized the initially demonstrated performance. The nanocomposite 1S\_F(N-GnP)@MWNT (3:1) showed a favorable OER activity, being a promising candidate as a bifunctional electrocatalyst towards OER and ORR

These composites have not been commonly studied for OER. However, a comparative analysis of the results reported by Ferreira *et al.* can be made.<sup>85</sup> For a nanocomposite composed of MoS<sub>2</sub> and MWNTs, values of  $\eta_{10 \text{ mA}\cdot\text{cm}^{-2}} = 0.55 \text{ V}$ ,  $\text{TS} = 82 \text{ mV}\cdot\text{dec}^{-1}$  and  $j_{1.8} = 11.9 \text{ mA}\cdot\text{cm}^{-2}$  were observed. For the 1S\_F(N-GnP)@MWNT (3:1), the nanocomposite with the most promising OER performance among the materials tested, the obtained results were slightly better than the described above. This clearly indicated the advantage of the nanocomposite preparation with the N-GnP counterpart and of the optimization of the nanocomposite preparation processes explored. Although it was possible to gain insight on the variables that lead to the improvement of the

electrocatalytic activity, it is also crucial to pave the way for further optimization on the nanocomposites preparation process and a fine-tuning on the materials properties.

Table 10. OER electrocatalytic parameters,  $j_{1.8}$  and TS, for MoS<sub>2</sub>@GnP nanocomposites (1S\_F and 1S\_F(N-GnP)), (MoS<sub>2</sub>@GnP)@MWNT (1S\_F@MWNT (1:3) and 1S\_F(N-GnP)@MWNT (3:1)) and RuO<sub>2</sub>.

Sample	$j_{1.8} / \text{mA}\cdot\text{cm}^{-2}$	TS / $\text{mV}\cdot\text{dec}^{-1}$
1S_F	1.26	184
1S_F(N-GnP)	1.48	221
1S_F@MWNT (1:3)	7.57	109
1S_F(N-GnP)@MWNT (3:1)	25.0	67
RuO <sub>2</sub>	2.88	76

# **Chapter 4**

*Conclusions and Future Perspectives*

## 4. Conclusions and Future Perspectives

In this work, two sets of nanocomposites were pursued, the first consisting of MoS<sub>2</sub> and GnPs and the second of a ternary combination of the binary nanocomposite with MWNTs. The hybrid materials were obtained through experimental procedures using mild conditions, namely surfactant-assisted liquid phase exfoliation (one-step dispersion and two-step dispersion procedures) and mechanical exfoliation (using ball milling). The morphology, structure and electrocatalytic behavior for ORR and OER were evaluated for the different nanocomposites prepared. In addition, the influence of the preparation method, the effect of the mass ratio of the nanocomposite components and the impact of the doping of GnPs with nitrogen atoms were also evaluated.

SEM morphological studies proved the influence of the preparation methodology on the structuring of the material and, for the 3D nanocomposites, it was revealed that MWNTs interacted with the MoS<sub>2</sub>@GnP counterpart. Additionally, for the 3D nanocomposites, it was found that the use of different mass ratios of the individual components also changed the morphological properties of the material. The use of GnPs doped with nitrogen was beneficial for the organization of both types of hybrid materials.

The P-XRD analysis allowed to identify the characteristic peaks of the starting nanomaterials in the diffractograms of the nanocomposites assembled, indicating their successful preparation. Furthermore, the results also indicated that the preparation process of the nanocomposites allowed to conserve the structure of the individual components.

The composites were studied as alternative electrocatalysts for both oxygen reactions, ORR and OER. In a first approach, the preliminary results showed that the assembly procedure did not have a significant impact on the electrocatalytic performance of either the 2D or 3D nanocomposites. Overall, the MoS<sub>2</sub>@GnP heterostructures showed a higher electrocatalytic activity than the individually components. The respective activity was enhanced when MWNTs were added to the nanocomposite. Regarding the mass ratio of nanomaterials tested, it was found that for the 2D heterostructures, a ratio of 1:1 was the more beneficial for the electrocatalytic properties. On the other hand, for the 3D materials, the use of a greater amount of MWNTs lead to an improvement in the triggering of the oxygen reactions. The N-doping of GnPs was also beneficial to the overall ORR and OER performance of the nanocomposites.

In ORR assays, the most promising nanocomposites prepared (1S\_F, 1S\_F(N-GnP), 1S\_F@MWNT (1:3) and 1S\_F(N-GnP)@MWNT (3:1)) showed  $j_L$  values in the range of -2.00 to -3.75 mA·cm<sup>-2</sup> and  $E_{\text{onset}}$  values between 0.75 and 0.86 V vs. RHE. Except for the heterostructure formed by MoS<sub>2</sub> and non-doped GnPs (1S\_F), the mentioned

materials reached  $\tilde{n}_{\text{O}_2}$  values close to 3, indicating that the reduction reaction proceeds according to a mixed 2- and 4-electron mechanism. Chronoamperometry studies indicated good long-term electrochemical stability and methanol tolerance. For OER, the samples did not show promising results, with  $j$  values below  $10 \text{ mA}\cdot\text{cm}^{-2}$ . However, the 1S\_F(N-GnP)@MWNT (3:1) nanocomposite improved the OER electrocatalytic activity, yielding values of  $j_{1.8}$ , TS and  $\eta_{10 \text{ mA}\cdot\text{cm}^{-2}}$  of  $25.0 \text{ mA}\cdot\text{cm}^{-2}$ ,  $67 \text{ mV}\cdot\text{dec}^{-1}$  and  $0.47 \text{ V}$ , respectively.

The current work contributes to lay the foundations of the development of hierarchical 3D structures as potential oxygen reaction electrocatalysts (ORR/OER), resorting to simple and cost-effective fabrication methods.

As future work, it will be necessary to deepen the materials characterization in some key aspects, namely by X-ray photoelectron spectroscopy (XPS), in order to confirm the N-doping of the GnPs and to better understand the materials composition, mainly in nanocomposites with N-GnPs. In addition, it would be relevant to prepare and evaluate the electrocatalytic performance of the nanocomposite analogous to 1S\_F(N-GnP)@MWNT (3:1) but without the presence of  $\text{MoS}_2$  (only N-GnP@MWNT nanocomposite), to study the real influence of the presence of the  $\text{MoS}_2$  on the electrocatalytic properties. Thus, it will also be important to investigate if the N-doping interferes with the interactions between  $\text{MoS}_2$  and the N-GnPs. As an alternative possibility, the doping of MWNTs with nitrogen atoms can also be pursued in an attempt to improve the electrocatalytic activity of the resultant nanocomposites.

Another aspect that can be explored is the mixing method of the  $\text{MoS}_2$ @GnP and MWNTs dispersion counterparts during the preparation stage. In this work, for the one-step dispersion and two-step dispersion procedures employed, both dispersions were mixed before being simultaneously deposited on the substrate. A possible alternative is to perform a sequential deposition of the dispersions, according to an adapted “layer-by-layer” method.<sup>123</sup> This method might prove beneficial for the structuring of the 3D nanocomposite, since it can enable a better control of the layers arrangements.

## References

1. Terrones, M., Science and technology of the twenty-first century: Synthesis, properties and applications of carbon nanotubes. *Ann. Rev. Mater. Res.* **2003**, *33*, 419-501.
2. Zhang, J.; Terrones, M.; Park, C. R.; Mukherjee, R.; Monthieux, M.; Koratkar, N.; Kim, Y. S.; Hurt, R.; Frackowiak, E.; Enoki, T.; Chen, Y.; Chen, Y. S.; Bianco, A., Carbon science in 2016: Status, challenges and perspectives. *Carbon* **2016**, *98*, 708-732.
3. Dai, L.; Xue, Y.; Qu, L.; Choi, H.-J.; Baek, J.-B., Metal-free catalysts for oxygen reduction reaction. *Chem. Rev.* **2015**, *115* (11), 4823-4892.
4. Vaisman, L.; Wagner, H. D.; Marom, G., The role of surfactants in dispersion of carbon nanotubes. *Adv. Colloid Interface Sci.* **2006**, *128*, 37-46.
5. Kroto, H. W.; Heath, J. R.; O'Brien, S. C.; Curl, R. F.; Smalley, R. E., C60: Buckminsterfullerene. *Nature* **1985**, *318* (6042), 162-163.
6. Iijima, S., Helical microtubules of graphitic carbon. *Nature* **1991**, *354* (6348), 56-58.
7. Novoselov, K. S.; Geim, A. K.; Morozov, S. V.; Jiang, D.; Zhang, Y.; Dubonos, S. V.; Grigorieva, I. V.; Firsov, A. A., Electric field effect in atomically thin carbon films. *Science* **2004**, *306* (5696), 666-669.
8. Qiu, L.; Yang, X. W.; Gou, X. L.; Yang, W. R.; Ma, Z. F.; Wallace, G. G.; Li, D., Dispersing carbon nanotubes with graphene oxide in water and synergistic effects between graphene derivatives. *Chem.-Eur. J.* **2010**, *16* (35), 10653-10658.
9. Tung, V. C.; Chen, L. M.; Allen, M. J.; Wassei, J. K.; Nelson, K.; Kaner, R. B.; Yang, Y., Low-temperature solution processing of graphene-carbon nanotube hybrid materials for high-performance transparent conductors. *Nano Lett.* **2009**, *9* (5), 1949-1955.
10. Yoo, E.; Kim, J.; Hosono, E.; Zhou, H.; Kudo, T.; Honma, I., Large reversible Li storage of graphene nanosheet families for use in rechargeable lithium ion batteries. *Nano Lett.* **2008**, *8* (8), 2277-2282.
11. Dai, L. M.; Chang, D. W.; Baek, J. B.; Lu, W., Carbon nanomaterials for advanced energy conversion and storage. *Small* **2012**, *8* (8), 1130-1166.
12. Yazid, M.; Sidik, N. A. C.; Mamat, R.; Najafi, G., A review of the impact of preparation on stability of carbon nanotube nanofluids. *Int. Commun. Heat Mass Transf.* **2016**, *78*, 253-263.
13. Zhou, Y.; Fang, Y.; Ramasamy, R. P., Non-covalent functionalization of carbon nanotubes for electrochemical biosensor development. *Sensors* **2019**, *19* (2), 392.

14. De Volder, M. F. L.; Tawfick, S. H.; Baughman, R. H.; Hart, A. J., Carbon nanotubes: Present and future commercial applications. *Science* **2013**, 339 (6119), 535-539.
15. Vidu, R.; Rahman, M.; Mahmoudi, M.; Enachescu, M.; Poteca, T. D.; Opris, I., Nanostructures: a platform for brain repair and augmentation. *Front. Syst. Neurosci.* **2014**, 8 (91).
16. Saifuddin, N.; Raziah, A. Z.; Junizah, A. R., Carbon nanotubes: A review on structure and their interaction with proteins. *J. Chem.* **2013**, 2013, 18.
17. Thess, A.; Lee, R.; Nikolaev, P.; Dai, H. J.; Petit, P.; Robert, J.; Xu, C. H.; Lee, Y. H.; Kim, S. G.; Rinzler, A. G.; Colbert, D. T.; Scuseria, G. E.; Tomanek, D.; Fischer, J. E.; Smalley, R. E., Crystalline ropes of metallic carbon nanotubes. *Science* **1996**, 273 (5274), 483-487.
18. Journet, C.; Maser, W. K.; Bernier, P.; Loiseau, A.; delaChapelle, M. L.; Lefrant, S.; Deniard, P.; Lee, R.; Fischer, J. E., Large-scale production of single-walled carbon nanotubes by the electric-arc technique. *Nature* **1997**, 388 (6644), 756-758.
19. Brukh, R.; Mitra, S., Mechanism of carbon nanotube growth by CVD. *Chem. Phys. Lett.* **2006**, 424 (1), 126-132.
20. Geim, A. K.; Novoselov, K. S., The rise of graphene. *Nat. Mater.* **2007**, 6 (3), 183-191.
21. Jin, H. Y.; Guo, C. X.; Liu, X.; Liu, J. L.; Vasileff, A.; Jiao, Y.; Zheng, Y.; Qiao, S. Z., Emerging two-dimensional nanomaterials for electrocatalysis. *Chem. Rev.* **2018**, 118 (13), 6337-6408.
22. Georgakilas, V.; Otyepka, M.; Bourlinos, A. B.; Chandra, V.; Kim, N.; Kemp, K. C.; Hobza, P.; Zboril, R.; Kim, K. S., Functionalization of graphene: covalent and non-covalent approaches, derivatives and applications. *Chem. Rev.* **2012**, 112 (11), 6156-6214.
23. Lin, Z.; Ye, X. H.; Han, J. P.; Chen, Q.; Fan, P. X.; Zhang, H. J.; Xie, D.; Zhu, H. W.; Zhong, M. L., Precise control of the number of layers of graphene by picosecond laser thinning. *Sci Rep* **2015**, 5, 1-7.
24. Jarrais, B.; Guedes, A.; Freire, C., Heteroatom-doped carbon nanomaterials as metal-free catalysts for the reduction of 4-Nitrophenol. *ChemistrySelect* **2018**, 3 (6), 1737-1748.
25. Zhu, H. Y.; Gan, X.; McCreary, A.; Lv, R. T.; Lin, Z.; Terrones, M., Heteroatom doping of two-dimensional materials: From graphene to chalcogenides. *Nano Today* **2020**, 30, 100829.

26. Duan, J. J.; Chen, S.; Jaroniec, M.; Qiao, S. Z., Heteroatom-doped graphene-based materials for energy-relevant electrocatalytic processes. *ACS Catal.* **2015**, *5* (9), 5207-5234.
27. Wang, X. W.; Sun, G. Z.; Routh, P.; Kim, D. H.; Huang, W.; Chen, P., Heteroatom-doped graphene materials: syntheses, properties and applications. *Chem. Soc. Rev.* **2014**, *43* (20), 7067-7098.
28. Rangraz, Y.; Heravi, M. M., Recent advances in metal-free heteroatom-doped carbon heterogonous catalysts. *RSC Adv.* **2021**, *11* (38), 23725-23778.
29. Li, J. C.; Hou, P. X.; Liu, C., Heteroatom-doped carbon nanotube and graphene-based electrocatalysts for oxygen reduction reaction. *Small* **2017**, *13* (45), 1702002.
30. Mak, K. F.; Shan, J., Photonics and optoelectronics of 2D semiconductor transition metal dichalcogenides. *Nat. Photonics* **2016**, *10* (4), 216-226.
31. Manzeli, S.; Ovchinnikov, D.; Pasquier, D.; Yazyev, O. V.; Kis, A., 2D transition metal dichalcogenides. *Nat. Rev. Mater.* **2017**, *2* (8), 15.
32. Lv, R.; Robinson, J. A.; Schaak, R. E.; Sun, D.; Sun, Y. F.; Mallouk, T. E.; Terrones, M., Transition metal dichalcogenides and beyond: Synthesis, properties, and applications of single- and few-layer nanosheets. *Acc. Chem. Res.* **2015**, *48* (1), 56-64.
33. Chhowalla, M.; Shin, H. S.; Eda, G.; Li, L. J.; Loh, K. P.; Zhang, H., The chemistry of two-dimensional layered transition metal dichalcogenide nanosheets. *Nat. Chem.* **2013**, *5* (4), 263-275.
34. Sha, R.; Bhattacharyya, T. K., MoS<sub>2</sub>-based nanosensors in biomedical and environmental monitoring applications. *Electrochim. Acta* **2020**, *349*, 16.
35. Kim, J.; Lee, E.; Mehta, G.; Choi, W., Stable and high-performance piezoelectric sensor via CVD grown WS<sub>2</sub>. *Nanotechnology* **2020**, *31* (44), 7.
36. Yun, Q. B.; Li, L. X.; Hu, Z. N.; Lu, Q. P.; Chen, B.; Zhang, H., Layered transition metal dichalcogenide-based nanomaterials for electrochemical energy storage. *Adv. Mater.* **2020**, *32* (1), 29.
37. Su, D. S.; Schlogl, R., Nanostructured carbon and carbon nanocomposites for electrochemical energy storage applications. *ChemSusChem* **2010**, *3* (2), 136-168.
38. Nasibulin, A. G.; Pikhitsa, P. V.; Jiang, H.; Brown, D. P.; Krasheninnikov, A. V.; Anisimov, A. S.; Queipo, P.; Moisala, A.; Gonzalez, D.; Lientschnig, G.; Hassanien, A.; Shandakov, S. D.; Lolli, G.; Resasco, D. E.; Choi, M.; Tomanek, D.; Kauppinen, E. I., A novel hybrid carbon material. *Nat. Nanotechnol.* **2007**, *2* (3), 156-161.
39. Pu, J. B.; Mo, Y. F.; Wan, S. H.; Wang, L. P., Fabrication of novel graphene-fullerene hybrid lubricating films based on self-assembly for MEMS applications. *Chem. Commun.* **2014**, *50* (4), 469-471.

40. Huang, J. R.; Her, S. C.; Yang, X. X.; Zhi, M. N., Synthesis and characterization of multi-walled carbon nanotube/graphene nanoplatelet hybrid film for flexible strain sensors. *Nanomaterials* **2018**, *8* (10).
41. Tung, V. C.; Chen, L. M.; Allen, M. J.; Wassei, J. K.; Nelson, K.; Kaner, R. B.; Yang, Y., Low-Temperature solution processing of graphene-carbon nanotube hybrid materials for high-performance transparent conductors. *Nano Lett* **2009**, *9* (5), 1949-1955.
42. Chen, P.; Xiao, T. Y.; Qian, Y. H.; Li, S. S.; Yu, S. H., A nitrogen-doped graphene/carbon nanotube nanocomposite with synergistically enhanced electrochemical activity. *Adv. Mater.* **2013**, *25* (23), 3192-3196.
43. Lee, C.; Ozden, S.; Tewari, C. S.; Park, O. K.; Vajtai, R.; Chatterjee, K.; Ajayan, P. M., MoS<sub>2</sub>-Carbon nanotube porous 3D network for enhanced oxygen reduction reaction. *ChemSusChem* **2018**, *11* (17), 2960-2966.
44. Jian, X. L.; Li, H. B.; Li, H.; Li, Y. X.; Shang, Y. Y., Flexible and freestanding MoS<sub>2</sub>/rGO/CNT hybrid fibers for high-capacity all-solid supercapacitors. *Carbon* **2021**, *172*, 132-137.
45. Sun, T. H.; Liu, X. H.; Li, Z. P.; Ma, L. M.; Wang, J. Q.; Yang, S. R., Graphene-wrapped CNT@MoS<sub>2</sub> hierarchical structure: synthesis, characterization and electrochemical application in supercapacitors. *New J. Chem.* **2017**, *41* (15), 7142-7150.
46. Pan, F. S.; Wang, J. Q.; Yang, Z. Z.; Gu, L.; Yu, Y., MoS<sub>2</sub>-graphene nanosheet-CNT hybrids with excellent electrochemical performances for lithium-ion batteries. *RSC Adv.* **2015**, *5* (95), 77518-77526.
47. Kim, Y.; Park, T.; Na, J.; Yi, J. W.; Kim, J.; Kim, M.; Bando, Y. S.; Yamauchi, Y.; Lin, J. J., Layered transition metal dichalcogenide/carbon nanocomposites for electrochemical energy storage and conversion applications. *Nanoscale* **2020**, *12* (16), 8608-8625.
48. Sun, H.; You, X.; Deng, J. E.; Chen, X. L.; Yang, Z. B.; Ren, J.; Peng, H. S., Novel graphene/carbon nanotube composite fibers for efficient wire-shaped miniature energy devices. *Adv. Mater.* **2014**, *26* (18), 2868-2873.
49. Qiu, L.; Yang, X.; Gou, X.; Yang, W.; Ma, Z.-F.; Wallace, G.; Li, D., Dispersing carbon nanotubes with graphene oxide in water and synergistic effects between graphene derivatives. *Chem.-Eur. J.* **2010**, *16*, 10653-8.
50. Novoselov, K. S.; Jiang, D.; Schedin, F.; Booth, T. J.; Khotkevich, V. V.; Morozov, S. V.; Geim, A. K., Two-dimensional atomic crystals. *Proc. Natl. Acad. Sci. U. S. A.* **2005**, *102* (30), 10451-10453.

51. Li, L.; Han, W.; Pi, L. J.; Niu, P.; Han, J. B.; Wang, C. L.; Su, B.; Li, H. Q.; Xiong, J.; Bando, Y.; Zhai, T. Y., Emerging in-plane anisotropic two-dimensional materials. *InfoMat* **2019**, *1* (1), 54-73.
52. Azadmanjiri, J.; Srivastava, V. K.; Kumar, P.; Sofer, Z.; Min, J. K.; Gong, J., Graphene-Supported 2D transition metal dichalcogenide van der waals heterostructures. *Appl. Mater. Today* **2020**, *19*, 33.
53. Geim, A. K.; Grigorieva, I. V., Van der Waals heterostructures. *Nature* **2013**, *499* (7459), 419-425.
54. Novoselov, K. S.; Mishchenko, A.; Carvalho, A.; Neto, A. H. C., 2D materials and van der Waals heterostructures. *Science* **2016**, *353* (6298), 7.
55. Furchi, M. M.; Pospischil, A.; Libisch, F.; Burgdorfer, J.; Mueller, T., Photovoltaic effect in an electrically tunable van der Waals heterojunction. *Nano Lett.* **2014**, *14* (8), 4785-4791.
56. Cheng, R.; Li, D. H.; Zhou, H. L.; Wang, C.; Yin, A. X.; Jiang, S.; Liu, Y.; Chen, Y.; Huang, Y.; Duan, X. F., Electroluminescence and photocurrent generation from atomically sharp WSe<sub>2</sub>/MoS<sub>2</sub> heterojunction p-n diodes. *Nano Lett.* **2014**, *14* (10), 5590-5597.
57. Liu, Y. C.; Zhao, Y. P.; Jiao, L. F.; Chen, J., A graphene-like MoS<sub>2</sub>/graphene nanocomposite as a highperformance anode for lithium ion batteries. *J. Mater. Chem. A* **2014**, *2* (32), 13109-13115.
58. Shanmugam, M.; Jacobs-Gedrim, R.; Song, E. S.; Yu, B., Two-dimensional layered semiconductor/graphene heterostructures for solar photovoltaic applications. *Nanoscale* **2014**, *6* (21), 12682-12689.
59. Dean, C. R.; Young, A. F.; Meric, I.; Lee, C.; Wang, L.; Sorgenfrei, S.; Watanabe, K.; Taniguchi, T.; Kim, P.; Shepard, K. L.; Hone, J., Boron nitride substrates for high-quality graphene electronics. *Nat. Nanotechnol.* **2010**, *5* (10), 722-726.
60. Lee, G. H.; Yu, Y. J.; Cui, X.; Petrone, N.; Lee, C. H.; Choi, M. S.; Lee, D. Y.; Lee, C.; Yoo, W. J.; Watanabe, K.; Taniguchi, T.; Nuckolls, C.; Kim, P.; Hone, J., Flexible and transparent MoS<sub>2</sub> field-effect transistors on hexagonal boron nitride-graphene heterostructures. *ACS Nano* **2013**, *7* (9), 7931-7936.
61. Solis-Fernandez, P.; Bissett, M.; Ago, H., Synthesis, structure and applications of graphene-based 2D heterostructures. *Chem. Soc. Rev.* **2017**, *46* (15), 4572-4613.
62. Ma, L.; Huang, G. C.; Chen, W. X.; Wang, Z.; Ye, J. B.; Li, H. Y.; Chen, D. Y.; Lee, J. Y., Cationic surfactant-assisted hydrothermal synthesis of few-layer molybdenum disulfide/graphene composites: Microstructure and electrochemical lithium storage. *J. Power Sources* **2014**, *264*, 262-271.

63. Chang, K.; Chen, W. X., In situ synthesis of MoS<sub>2</sub>/graphene nanosheet composites with extraordinarily high electrochemical performance for lithium ion batteries. *Chem. Commun.* **2011**, 47 (14), 4252-4254.
64. Ratha, S.; Rout, C. S., Supercapacitor electrodes based on layered tungsten disulfide-reduced graphene oxide hybrids synthesized by a facile hydrothermal method. *ACS Appl. Mater. Interfaces* **2013**, 5 (21), 11427-11433.
65. Luxa, J.; Mazanek, V.; Bousa, D.; Sedmidubsky, D.; Pumera, M.; Sofer, Z., Graphene-amorphous transition-metal chalcogenide (MoS<sub>x</sub>, WS<sub>x</sub>) composites as highly efficient hybrid electrocatalysts for the hydrogen evolution reaction. *ChemElectroChem* **2016**, 3 (4), 565-571.
66. Gnanasekar, P.; Periyanaounder, D.; Kulandaivel, J., Vertically aligned MoS<sub>2</sub> nanosheets on graphene for highly stable electrocatalytic hydrogen evolution reactions. *Nanoscale* **2019**, 11 (5), 2439-2446.
67. Li, D. W.; Xiong, W.; Jiang, L. J.; Xiao, Z. Y.; Golgir, H. R.; Wang, M. M.; Huang, X.; Zhou, Y. S.; Lin, Z.; Song, J. F.; Ducharme, S.; Jiang, L.; Silvain, J. F.; Lu, Y. F., Multimodal nonlinear optical imaging of MoS<sub>2</sub> and MoS<sub>2</sub>-based van der Waals heterostructures. *ACS Nano* **2016**, 10 (3), 3766-3775.
68. Wang, T. Z.; Liu, C. C.; Jiang, F. X.; Xu, Z. F.; Wang, X. D.; Li, X.; Li, C. C.; Xu, J. K.; Yang, X. W., Solution-processed two-dimensional layered heterostructure thin-film with optimized thermoelectric performance. *Phys. Chem. Chem. Phys.* **2017**, 19 (27), 17560-17567.
69. Fujigaya, T.; Nakashima, N., Non-covalent polymer wrapping of carbon nanotubes and the role of wrapped polymers as functional dispersants. *Sci. Technol. Adv. Mater* **2015**, 16 (2), 024802-23.
70. Karousis, N.; Tagmatarchis, N.; Tasis, D., Current progress on the chemical modification of carbon nanotubes. *Chem. Rev.* **2010**, 110 (9), 5366-5397.
71. Zhao, Y. L.; Stoddart, J. F., Noncovalent functionalization of single-walled carbon nanotubes. *Acc. Chem. Res.* **2009**, 42 (8), 1161-1171.
72. Jeon, I.-Y.; Chang, D.; Nanjundan, A. K.; Baek, J.-B., Functionalization of carbon nanotubes. 2011.
73. Dassios, K. G.; Alafogianni, P.; Antiohos, S. K.; Leptokaridis, C.; Barkoula, N. M.; Matikas, T. E., Optimization of sonication parameters for homogeneous surfactant-assisted dispersion of multiwalled carbon nanotubes in aqueous solutions. *J. Phys. Chem. C* **2015**, 119 (13), 7506-7516.
74. Abreu, B.; Rocha, J.; Fernandes, R. M. F.; Regev, O.; Furó, I.; Marques, E. F., Gemini surfactants as efficient dispersants of multiwalled carbon nanotubes: Interplay of

molecular parameters on nanotube dispersibility and debundling. *J. Colloid Interface Sci* **2019**, *547*, 69-77.

75. Abreu, B.; Montero, J.; Buzaglo, M.; Regev, O.; Marques, E. F., Comparative trends and molecular analysis on the surfactant-assisted dispersibility of 1D and 2D carbon materials: Multiwalled nanotubes vs graphene nanoplatelets. *J. Mol. Liq.* **2021**, *333*, 116002.

76. Dai, J.; Fernandes, R. M. F.; Regev, O.; Marques, E. F.; Furó, I., Dispersing carbon nanotubes in water with amphiphiles: Dispersant adsorption, kinetics, and bundle size distribution as defining factors. *J. Phys. Chem. C* **2018**, *122* (42), 24386-24393.

77. Fernandes, R. M. F.; Abreu, B.; Claro, B.; Buzaglo, M.; Regev, O.; Furó, I.; Marques, E. F., Dispersing carbon nanotubes with ionic surfactants under controlled conditions: Comparisons and insight. *Langmuir* **2015**, *31* (40), 10955-10965.

78. Al-Hamadani, Y. A. J.; Chu, K. H.; Son, A.; Heo, J.; Her, N.; Jang, M.; Park, C. M.; Yoon, Y., Stabilization and dispersion of carbon nanomaterials in aqueous solutions: A review. *Sep. Purif. Technol.* **2015**, *156*, 861-874.

79. Shchukin, D. G.; Skorb, E.; Belova, V.; Mohwald, H., Ultrasonic cavitation at solid surfaces. *Adv. Mater.* **2011**, *23* (17), 1922-1934.

80. Rubio, N.; Fabbro, C.; Herrero, M. A.; de la Hoz, A.; Meneghetti, M.; Fierro, J. L. G.; Prato, M.; Vazquez, E., Ball-milling modification of single-walled carbon nanotubes: Purification, cutting, and functionalization. *Small* **2011**, *7* (5), 665-674.

81. Ji, H. M.; Hu, S.; Jiang, Z. Y.; Shi, S. J.; Hou, W. H.; Yang, G., Directly scalable preparation of sandwiched MoS<sub>2</sub>/graphene nanocomposites via ball-milling with excellent electrochemical energy storage performance. *Electrochim. Acta* **2019**, *299*, 143-151.

82. Fan, X. L.; Chang, D. W.; Chen, X. L.; Baek, J. B.; Dai, L. M., Functionalized graphene nanoplatelets from ball milling for energy applications. *Curr. Op. Chem. Eng.* **2016**, *11*, 52-58.

83. Marques, E. F.; Silva, B. F. B., Surfactants, Phase Behavior. In *Encyclopedia of Colloid and Interface Science*, Tadros, T., Ed. Springer Berlin Heidelberg: Berlin, Heidelberg, 2013; pp 1290-1333.

84. Holmberg, K.; Jönsson, B.; Kronberg, B.; Lindman, B., Surfactants and Polymers in Aqueous Solution, Second Edition. John Wiley & Sons: West Sussex, UK, 2003; pp 39-66.

85. Ferreira, P.; Abreu, B.; Freire, C.; Fernandes, D. M.; Marques, E. F., Nanocomposites prepared from carbon nanotubes and the transition metal dichalcogenides WS<sub>2</sub> and MoS<sub>2</sub> via surfactant-assisted dispersions as electrocatalysts for oxygen reactions. *Materials* **2021**, *14* (4), 896.

86. Fernandes, R. M. F.; Dai, J.; Regev, O.; Marques, E. F.; Furo, I., Block copolymers as dispersants for single-walled carbon nanotubes: modes of surface attachment and role of block polydispersity. *Langmuir* **2018**, *34* (45), 13672-13679.
87. Shen, J.; Hu, Y.; Qin, C.; Ye, M., Layer-by-Layer self-assembly of multiwalled carbon nanotube polyelectrolytes prepared by in situ radical polymerization. *Langmuir* **2008**, *24* (8), 3993-3997.
88. Wang, S.; Yu, D.; Dai, L., Polyelectrolyte functionalized carbon nanotubes as efficient metal-free electrocatalysts for oxygen reduction. *J. Am. Chem. Soc.* **2011**, *133* (14), 5182-5185.
89. Fernandes, D. M.; Mestre, A. S.; Martins, A.; Nunes, N.; Carvalho, A. P.; Freire, C., Biomass-derived nanoporous carbons as electrocatalysts for oxygen reduction reaction. *Catal. Today* **2020**, *357*, 269-278.
90. Wang, H. F.; Xu, Q., Materials design for rechargeable metal-air batteries. *Matter* **2019**, *1* (3), 565-595.
91. Seh, Z. W.; Kibsgaard, J.; Dickens, C. F.; Chorkendorff, I. B.; Norskov, J. K.; Jaramillo, T. F., Combining theory and experiment in electrocatalysis: Insights into materials design. *Science* **2017**, *355* (6321).
92. Liu, Q. F.; Pan, Z. F.; Wang, E. D.; An, L.; Sun, G. Q., Aqueous metal-air batteries: Fundamentals and applications. *Energy Storage Mater.* **2020**, *27*, 478-505.
93. Nunes, M.; Fernandes, D. M.; Morales, M. V.; Rodriguez-Ramos, I.; Guerrero-Ruiz, A.; Freire, C., Cu and Pd nanoparticles supported on a graphitic carbon material as bifunctional HER/ORR electrocatalysts. *Catal. Today* **2020**, *357*, 279-290.
94. Freire, C.; Fernandes, D. M.; Nunes, M.; Abdelkader, V. K., POM & MOF-based electrocatalysts for energy-related reactions. *ChemCatChem* **2018**, *10* (8), 1703-1730.
95. Nunes, M.; Rocha, I. M.; Fernandes, D. M.; Mestre, A. S.; Moura, C. N.; Carvalho, A. P.; Pereira, M. F. R.; Freire, C., Sucrose-derived activated carbons: electron transfer properties and application as oxygen reduction electrocatalysts. *RSC Adv.* **2015**, *5* (124), 102919-102931.
96. Mathumba, P.; Fernandes, D. M.; Matos, R.; Iwuoha, E. I.; Freire, C., Metal oxide (Co<sub>3</sub>O<sub>4</sub> and Mn<sub>3</sub>O<sub>4</sub>) impregnation into S, N-doped graphene for oxygen reduction reaction (ORR). *Materials* **2020**, *13* (7), 1562-1575.
97. Araujo, M. P.; Nunes, M.; Rocha, I. M.; Pereira, M. F. R.; Freire, C., Co<sub>3</sub>O<sub>4</sub> Nanoparticles anchored on selectively oxidized graphene flakes as bifunctional electrocatalysts for oxygen reactions. *ChemistrySelect* **2018**, *3* (35), 10064-10076.
98. Jiao, Y.; Zheng, Y.; Jaroniec, M. T.; Qiao, S. Z., Design of electrocatalysts for oxygen- and hydrogen-involving energy conversion reactions. *Chem. Soc. Rev.* **2015**, *44* (8), 2060-2086.

99. Daems, N.; Sheng, X.; Vankelecom, I. F. J.; Pescarmona, P. P., Metal-free doped carbon materials as electrocatalysts for the oxygen reduction reaction. *J. Mater. Chem. A* **2014**, *2* (12), 4085-4110.
100. Ma, R. G.; Lin, G. X.; Zhou, Y.; Liu, Q.; Zhang, T.; Shan, G. C.; Yang, M. H.; Wang, J. C., A review of oxygen reduction mechanisms for metal-free carbon-based electrocatalysts. *Npj Comput. Mater.* **2019**, *5*, 1-15.
101. Huang, Z. F.; Wang, J.; Peng, Y. C.; Jung, C. Y.; Fisher, A.; Wang, X., Design of efficient bifunctional oxygen reduction/evolution electrocatalyst: Recent advances and perspectives. *Adv. Energy Mater.* **2017**, *7* (23), 1700544.
102. Reier, T.; Oezaslan, M.; Strasser, P., Electrocatalytic oxygen evolution reaction (OER) on Ru, Ir, and Pt catalysts: A comparative study of nanoparticles and bulk materials. *ACS Catal.* **2012**, *2* (8), 1765-1772.
103. Zhu, Y.; Zhang, Z. Y.; Li, W. Q.; Lei, Z.; Cheng, N. C.; Tan, Y. Y.; Mu, S. C.; Sun, X. L., Highly exposed active sites of defect-enriched derived MOFs for enhanced oxygen reduction reaction. *ACS Sustain. Chem. Eng.* **2019**, *7* (21), 17855-17862.
104. Kishore, P. S.; Viswanathan, B.; Varadarajan, T. K., Electrochemical oxygen reduction reaction by Pt nanoparticles on carbon support stabilized by polyoxometalates. *J. Nanosci. Nanotechnol.* **2009**, *9* (9), 5188-5197.
105. Xie, X. H.; Nie, Y.; Chen, S.; Ding, W.; Qi, X. Q.; Li, L.; Wei, Z. D., A catalyst superior to carbon-supported-platinum for promotion of the oxygen reduction reaction: reduced-polyoxometalate supported palladium. *J. Mater. Chem. A* **2015**, *3* (26), 13962-13969.
106. Rocha, I. M.; Soares, O.; Fernandes, D. M.; Freire, C.; Figueiredo, J. L.; Pereira, M. F. R., N-doped carbon nanotubes for the oxygen reduction reaction in alkaline medium: Synergistic relationship between pyridinic and quaternary nitrogen. *ChemistrySelect* **2016**, *1* (10), 2522-2530.
107. Xiong, C.; Wei, Z. D.; Hu, B. S.; Chen, S. G.; Li, L.; Guo, L.; Ding, W.; Liu, X.; Ji, W. J.; Wang, X. P., Nitrogen-doped carbon nanotubes as catalysts for oxygen reduction reaction. *J. Power Sources* **2012**, *215*, 216-220.
108. Borghei, M.; Azcune, I.; Carrasco, P. M.; Sainio, J.; Kauppinen, E.; Ruiz, V., Nitrogen-doped graphene with enhanced oxygen reduction activity produced by pyrolysis of graphene functionalized with imidazole derivatives. *Int. J. Hydrog. Energy* **2014**, *39* (24), 12749-12756.
109. Geng, D. S.; Chen, Y.; Chen, Y. G.; Li, Y. L.; Li, R. Y.; Sun, X. L.; Ye, S. Y.; Knights, S., High oxygen-reduction activity and durability of nitrogen-doped graphene. *Energy Environ. Sci.* **2011**, *4* (3), 760-764.

110. Wang, L.; Yin, F. X.; Yao, C. X., N-doped graphene as a bifunctional electrocatalyst for oxygen reduction and oxygen evolution reactions in an alkaline electrolyte. *Int. J. Hydrog. Energy* **2014**, *39* (28), 15913-15919.
111. Cheng, Y. H.; Tian, Y. Y.; Fan, X. Z.; Liu, J. G.; Yan, C. W., Boron doped multi-walled carbon nanotubes as catalysts for oxygen reduction reaction and oxygen evolution reaction in alkaline media. *Electrochim. Acta* **2014**, *143*, 291-296.
112. Sheng, Z. H.; Gao, H. L.; Bao, W. J.; Wang, F. B.; Xia, X. H., Synthesis of boron doped graphene for oxygen reduction reaction in fuel cells. *J. Mater. Chem.* **2012**, *22* (2), 390-395.
113. Liu, R. L.; Wu, D. Q.; Feng, X. L.; Mullen, K., Nitrogen-doped ordered mesoporous graphitic arrays with high electrocatalytic activity for oxygen reduction. *Angew. Chem. Int. Ed.* **2010**, *49* (14), 2565-2569.
114. Jo, H. G.; Kim, K. H.; Ahn, H. J., Nitrogen-doped carbon quantum dots decorated on platinum catalysts for improved oxygen reduction reaction. *Appl. Surf. Sci* **2021**, *554*, 149594.
115. Li, Q. Q.; Zhang, S.; Dai, L. M.; Li, L. S., Nitrogen-doped colloidal graphene quantum dots and their size-dependent electrocatalytic activity for the oxygen reduction reaction. *J. Am. Chem. Soc.* **2012**, *134* (46), 18932-18935.
116. Thomas, A.; Fischer, A.; Goettmann, F.; Antonietti, M.; Muller, J. O.; Schlogl, R.; Carlsson, J. M., Graphitic carbon nitride materials: variation of structure and morphology and their use as metal-free catalysts. *J. Mater. Chem.* **2008**, *18* (41), 4893-4908.
117. Lee, J. S.; Jo, K.; Lee, T.; Yun, T.; Cho, J.; Kim, B. S., Facile synthesis of hybrid graphene and carbon nanotubes as a metal-free electrocatalyst with active dual interfaces for efficient oxygen reduction reaction. *J. Mater. Chem. A* **2013**, *1* (34), 9603-9607.
118. Ratso, S.; Kruusenberg, I.; Joost, U.; Saar, R.; Tammeveski, K., Enhanced oxygen reduction reaction activity of nitrogen-doped graphene/multi-walled carbon nanotube catalysts in alkaline media. *Int. J. Hydrog. Energy* **2016**, *41* (47), 22510-22519.
119. Pham, D. T.; Li, B.; Lee, Y. H., Nitrogen-doped activated graphene/SWCNT hybrid for oxygen reduction reaction. *Curr. Appl. Phys.* **2016**, *16* (9), 1242-1249.
120. Hao, L.; Yu, J.; Xu, X.; Yang, L.; Xing, Z. P.; Dai, Y.; Sun, Y.; Zou, J. L., Nitrogen-doped MoS<sub>2</sub>/carbon as highly oxygen-permeable and stable catalysts for oxygen reduction reaction in microbial fuel cells. *J. Power Sources* **2017**, *339*, 68-79.
121. Zhao, K.; Gu, W.; Zhao, L. Y.; Zhang, C. L.; Peng, W. D.; Xian, Y. Z., MoS<sub>2</sub>/Nitrogen-doped graphene as efficient electrocatalyst for oxygen reduction reaction. *Electrochim. Acta* **2015**, *169*, 142-149.

122. Bach, L. G.; Thi, M. L. N.; Bui, Q. B.; Nhac-Vu, H. T., Palladium sulfide nanoparticles attached MoS<sub>2</sub>/nitrogen-doped graphene heterostructures for efficient oxygen reduction reaction. *Synth. Met.* **2019**, *254*, 172-179.
123. Abreu, B.; Rocha, M.; Nunes, M.; Freire, C.; Marques, E. F., Carbon nanotube/graphene nanocomposites built via surfactant-mediated colloid assembly as metal-free catalysts for the oxygen reduction reaction. *J. Mater. Sci* **2021**, 1-16.
124. Goldstein, J. I.; Newbury, D. E.; Michael, J. R.; Ritchie, N. W.; Scott, J. H. J.; Joy, D. C., Scanning electron microscopy and x-ray microanalysis. 3 ed.; Springer: 2005; Vol. 27, pp 215-216.
125. Zhou, W.; Apkarian, R.; Wang, Z. L.; Joy, D., Fundamentals of Scanning Electron Microscopy (SEM). In *Scanning Microscopy for Nanotechnology: Techniques and Applications*, Zhou, W.; Wang, Z. L., Eds. Springer New York: New York, NY, 2007; pp 1-40.
126. Jenkins, R.; Snyder, R. L., *Introduction to X-ray powder diffractometry*. John Wiley & Sons, Inc.: New York, 1996.
127. Waseda Y., M. E., Shinoda K., *X-Ray Diffraction Crystallography: Introduction, Examples and Solved Problems*. Springer-Verlag Berlin Heidelberg, 2011.
128. Tao, L.; Wang, Q.; Dou, S.; Ma, Z. L.; Huo, J.; Wang, S. Y.; Dai, L. M., Edge-rich and dopant-free graphene as a highly efficient metal-free electrocatalyst for the oxygen reduction reaction. *Chem. Commun.* **2016**, *52* (13), 2764-2767.
129. Wang, Q.; Wang, Y. M.; Meng, Q. G.; Wang, T. L.; Guo, W. H.; Wu, G. H.; You, L., Preparation of high antistatic HDPE/polyaniline encapsulated graphene nanoplatelet composites by solution blending. *RSC Adv.* **2017**, *7* (5), 2796-2803.
130. Nie, P.; Min, C. Y.; Song, H. J.; Chen, X. H.; Zhang, Z. Z.; Zhao, K. L., Preparation and tribological properties of polyimide/carboxyl-functionalized multi-walled carbon nanotube nanocomposite films under seawater lubrication. *Tribol. Lett.* **2015**, *58* (1), 1-13.
131. Fernandes, D. M.; Mathumba, P.; Fernandes, A. J. S.; Iwuoha, E. I.; Freire, C., Towards efficient oxygen reduction reaction electrocatalysts through graphene doping. *Electrochim. Acta* **2019**, *319*, 72-81.
132. Zhou, R. F.; Zheng, Y.; Jaroniec, M.; Qiao, S. Z., Determination of the electron transfer number for the oxygen reduction reaction: From theory to experiment. *ACS Catal.* **2016**, *6* (7), 4720-4728.

## Appendix

### A.1. CVs of the materials in N<sub>2</sub>- and O<sub>2</sub>-saturated solutions

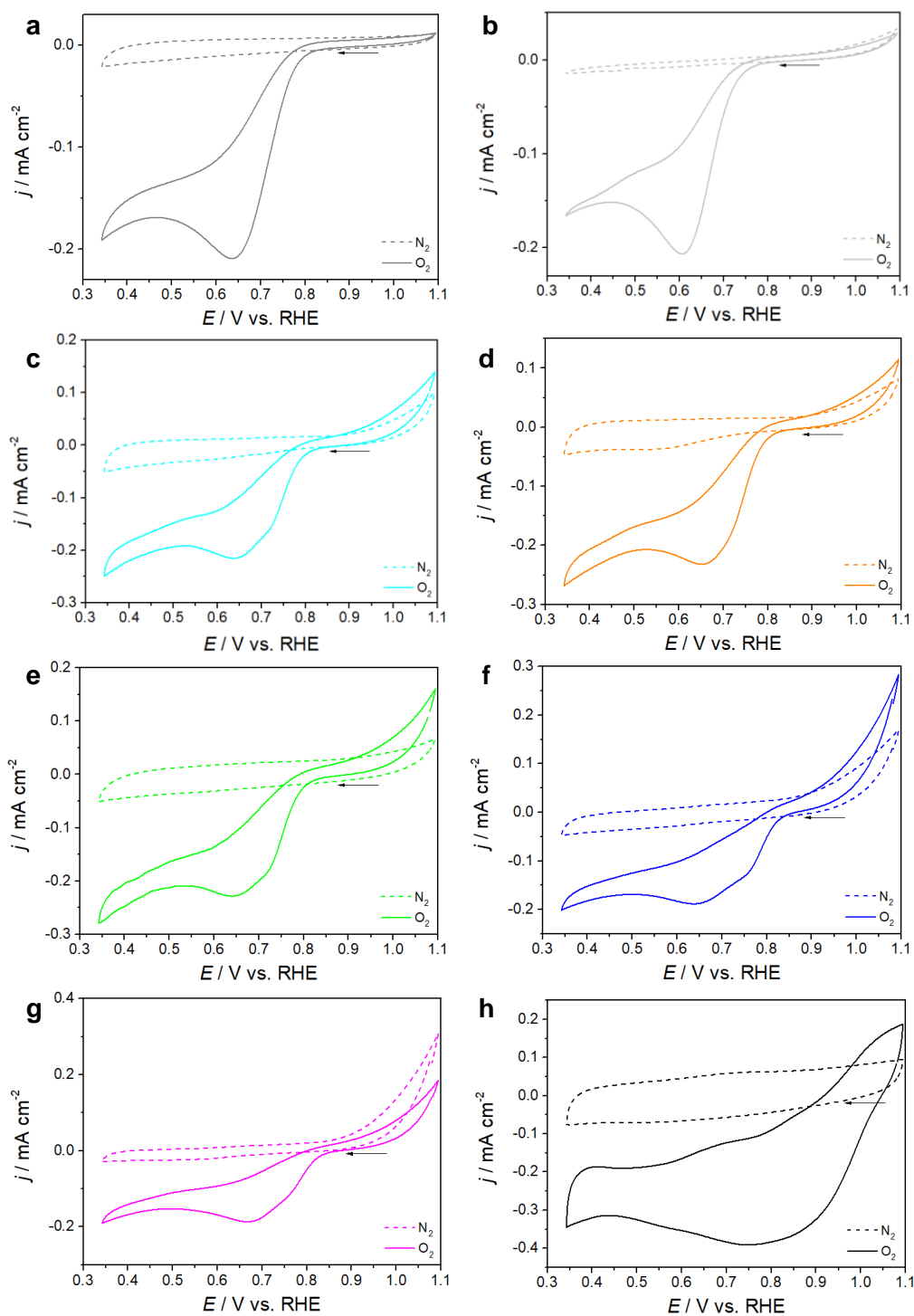


Figure 40. CVs of **a** GnPs, **b** MoS<sub>2</sub>, **c** 1S\_E, **d** 1S\_F, **e** 2S, **f** BM\_wos, **g** BM\_ws and **h** Pt/C, 0.1 mol·dm<sup>-3</sup> KOH N<sub>2</sub>- and O<sub>2</sub>-saturated solutions, at 0.005 V·s<sup>-1</sup>.

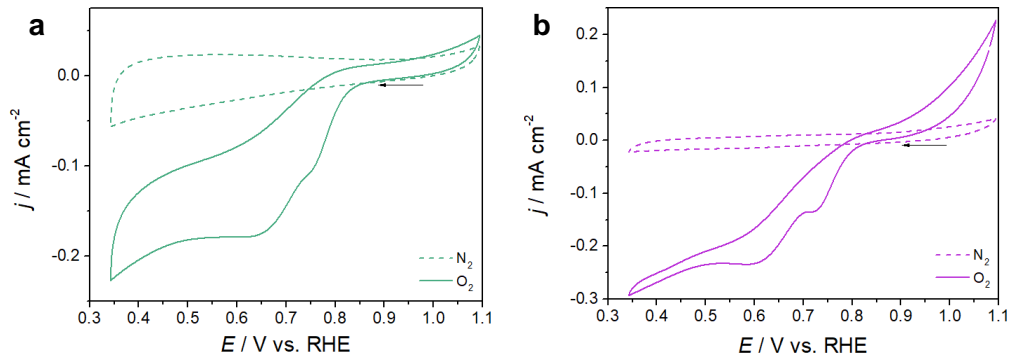


Figure 41. CVs of **a** 1S\_F(9:1) and **b** 1S\_F(1:9), 0.1 mol·dm<sup>-3</sup> KOH N<sub>2</sub>- and O<sub>2</sub>-saturated solutions, at 0.005 V·s<sup>-1</sup>.

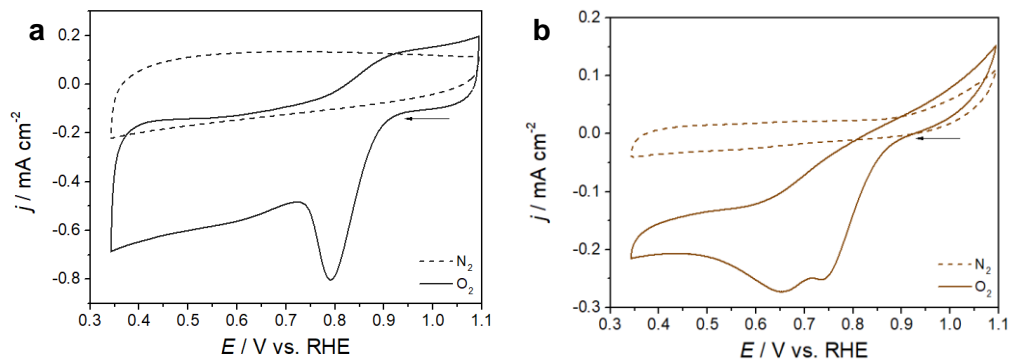


Figure 42. CVs of **a** N-GnPs and **b** 1S\_F(N-GnP), 0.1 mol·dm<sup>-3</sup> KOH N<sub>2</sub>- and O<sub>2</sub>-saturated solutions, at 0.005 V·s<sup>-1</sup>.

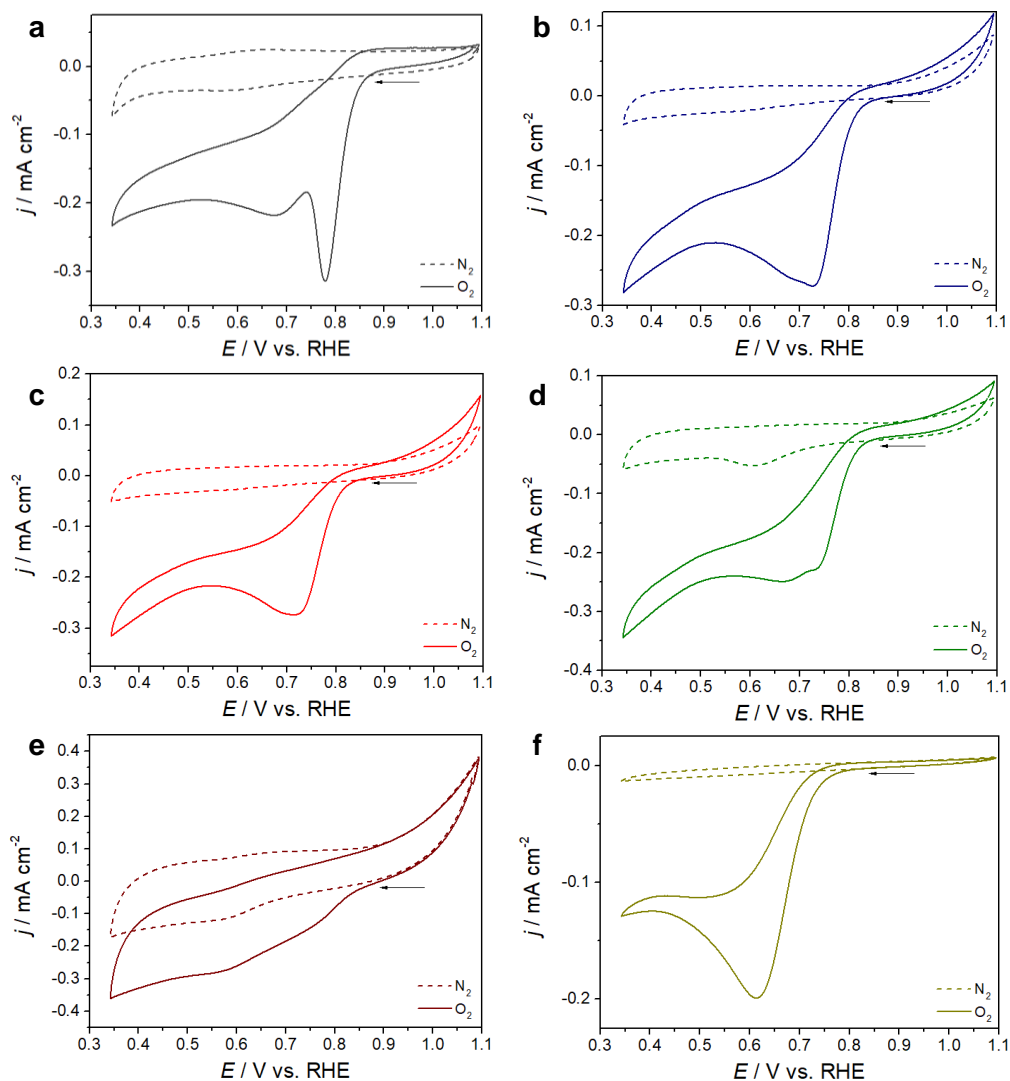


Figure 43. CVs of **a** MWNTs, **b** 1S\_E@MWNT, **c** 1S\_F@ MWNT, **d** 2S@MWNT, **e** BM\_wos@MWNT and **f** BM\_ws@MWNT, 0.1 mol·dm<sup>-3</sup> KOH N<sub>2</sub>- and O<sub>2</sub>-saturated solutions, at 0.005 V·s<sup>-1</sup>.

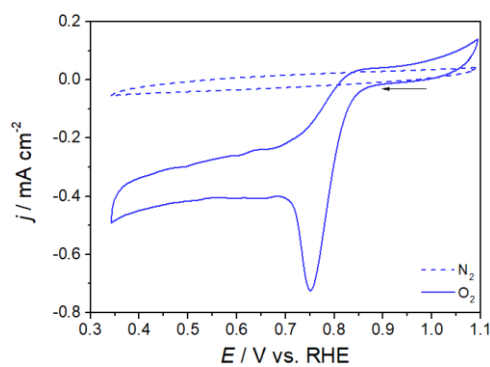


Figure 44. CVs of 1S\_F@MWNT (1:3), 0.1 mol·dm<sup>-3</sup> KOH N<sub>2</sub>- and O<sub>2</sub>-saturated solutions, at 0.005 V·s<sup>-1</sup>.

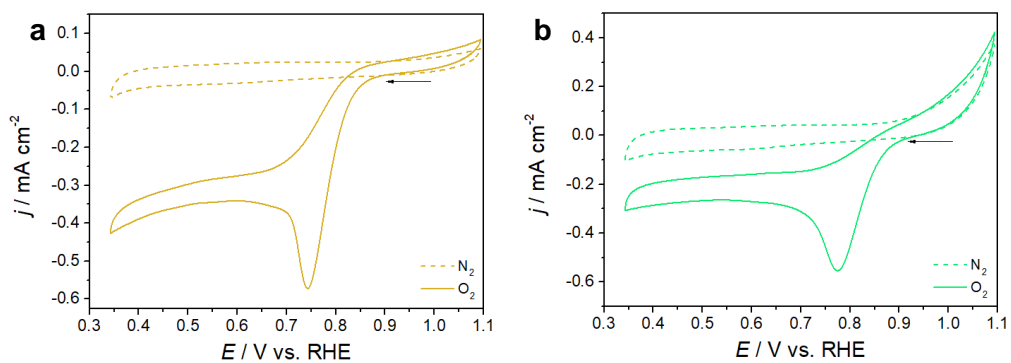


Figure 45. CVs of **a** 1S\_F(N-GnP)@MWNT (1:3) and **b** 1S\_F(N-GnP)@MWNT (3:1), 0.1 mol·dm<sup>-3</sup> KOH N<sub>2</sub>- and O<sub>2</sub>-saturated solutions, at 0.005 V·s<sup>-1</sup>.

## A.2. ORR polarization plots at several rotation rates

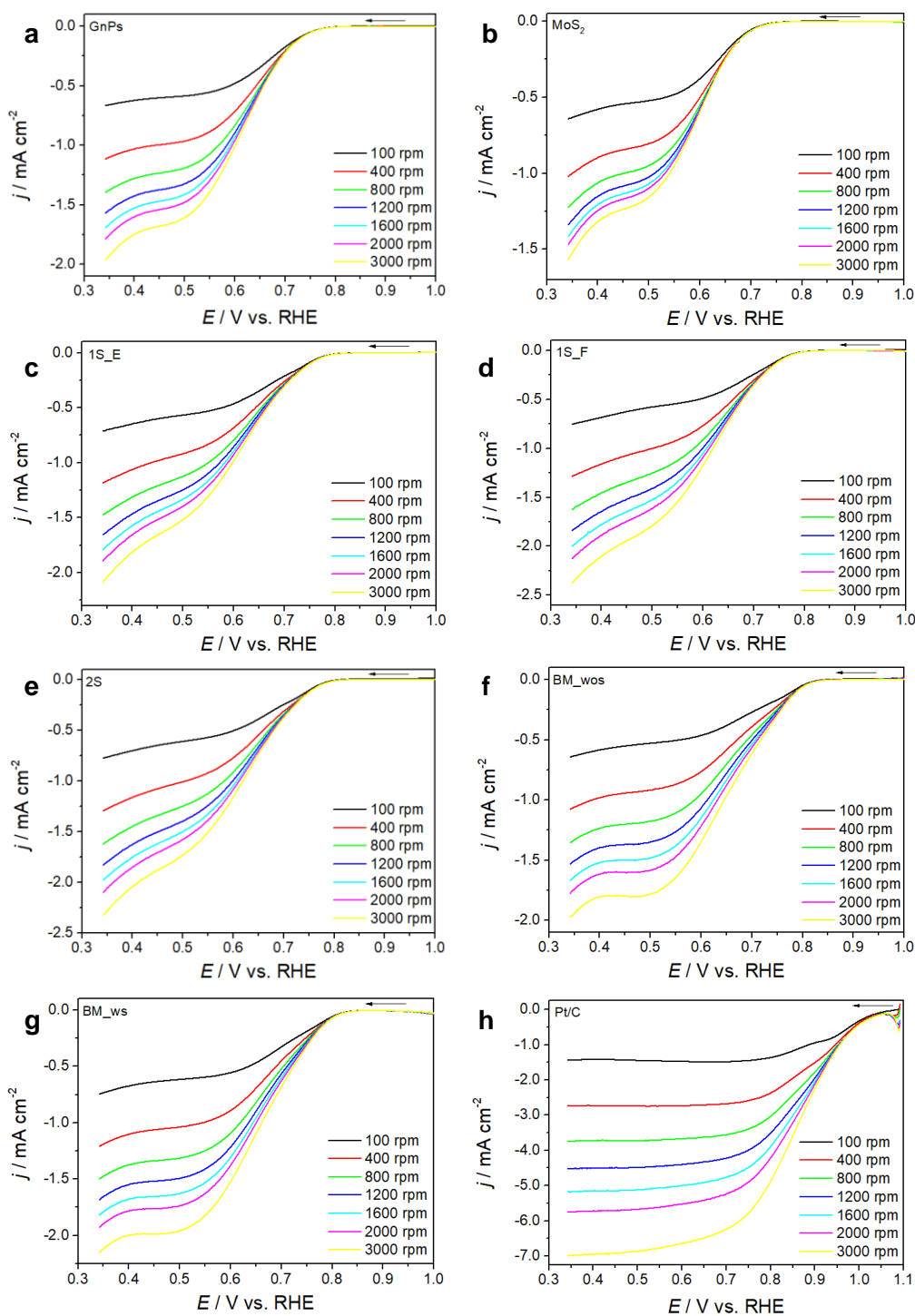


Figure 46. ORR polarization plots for **a** GnPs, **b** MoS<sub>2</sub>, **c** 1S\_E, **d** 1S\_F, **e** 2S, **f** BM\_wos, **g** BM\_ws and **h** Pt/C, at 100-3000 rpm and 0.005 V·s<sup>-1</sup>, in 0.1 mol·dm<sup>-3</sup> KOH.

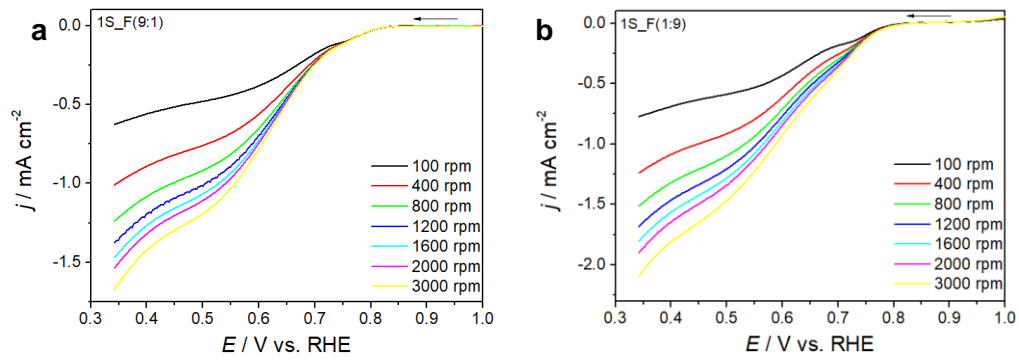


Figure 47. ORR polarization plots for **a** 1S\_F(9:1) and **b** 1S\_F(1:9), at 100-3000 rpm and 0.005 V·s<sup>-1</sup>, in 0.1 mol·dm<sup>-3</sup> KOH.

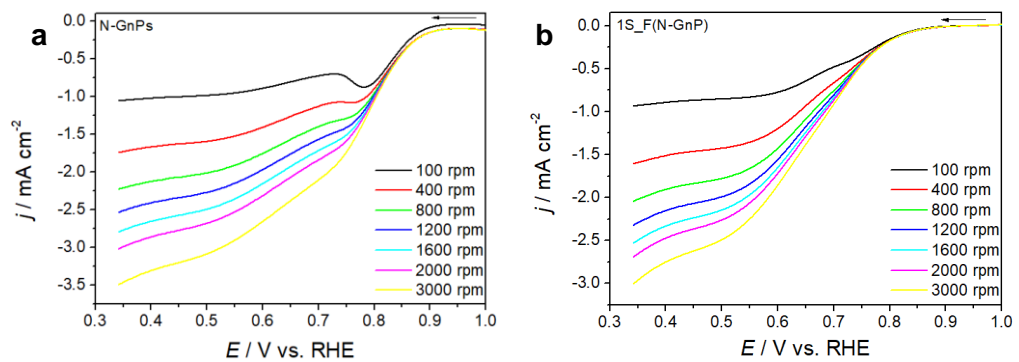


Figure 48. ORR polarization plots for **a** N-GnP and **b** 1S\_F(N-GnP), at 100-3000 rpm and 0.005 V·s<sup>-1</sup>, in 0.1 mol·dm<sup>-3</sup> KOH.

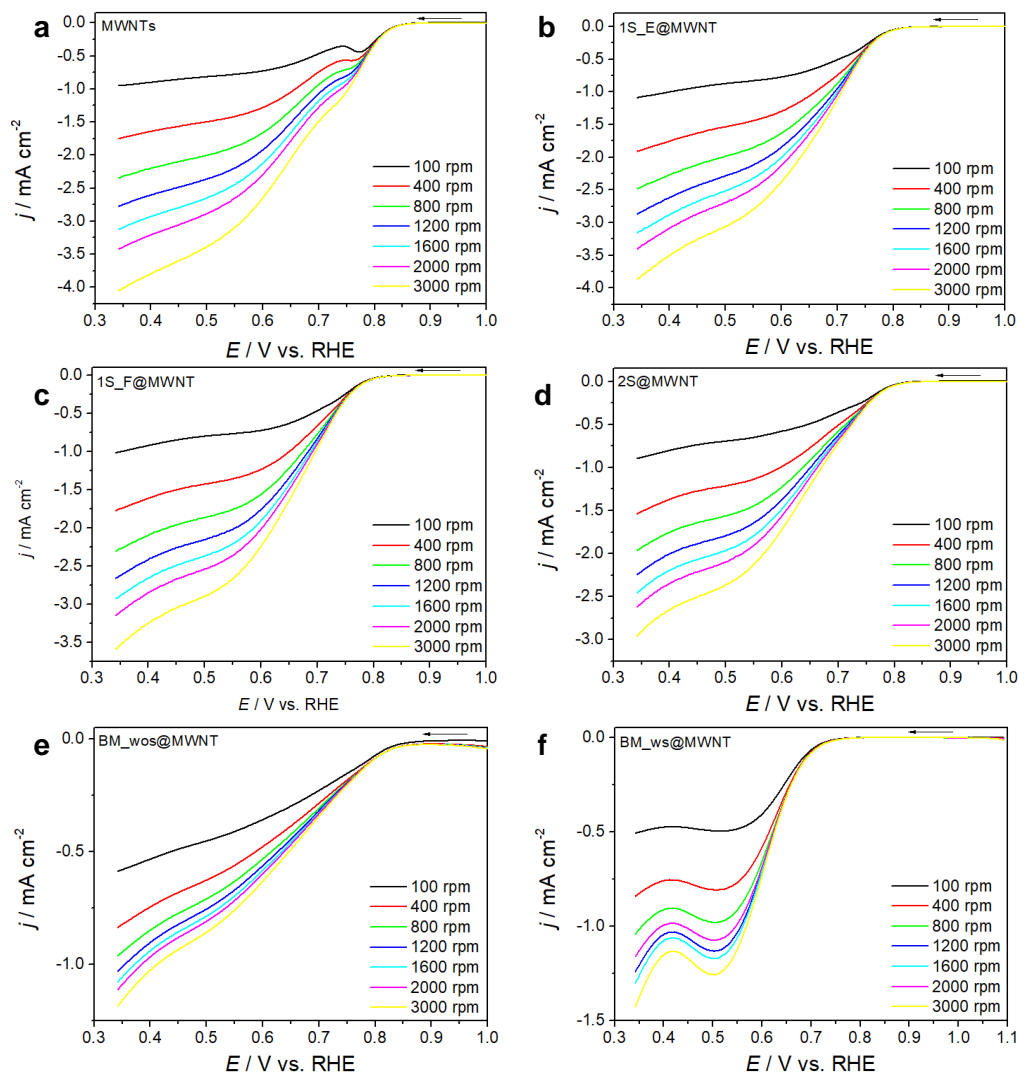


Figure 49. ORR polarization plots for **a** MWNTs, **b** 1S\_E@MWNT, **c** 1S\_F@ MWNT, **d** 2S@MWNT, **e** BM\_wos@MWNT and **f** BM\_ws@MWNT, at 100-3000 rpm and  $0.005 \text{ V}\cdot\text{s}^{-1}$ , in  $0.1 \text{ mol}\cdot\text{dm}^{-3} \text{ KOH}$ .

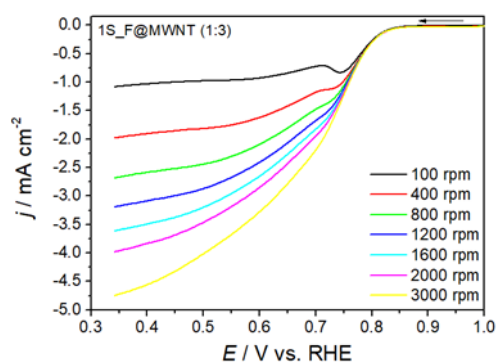


Figure 50. ORR polarization plots for 1S\_F@MWNT (1:3), at 100-3000 rpm and  $0.005 \text{ V}\cdot\text{s}^{-1}$ , in  $0.1 \text{ mol}\cdot\text{dm}^{-3} \text{ KOH}$ .

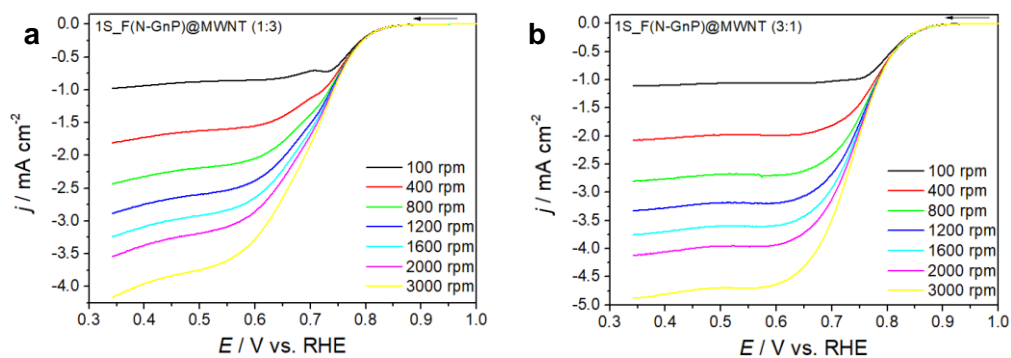


Figure 51. ORR polarization plots for **a** 1S\_F(N-GnP)@MWNT (1:3) and **b** 1S\_F(N-GnP)@MWNT (3:1), at 100-3000 rpm and 0.005 V·s<sup>-1</sup>, in 0.1 mol·dm<sup>-3</sup> KOH.

### A.3. ORR polarization Koutecky-Levich (K-L) plots

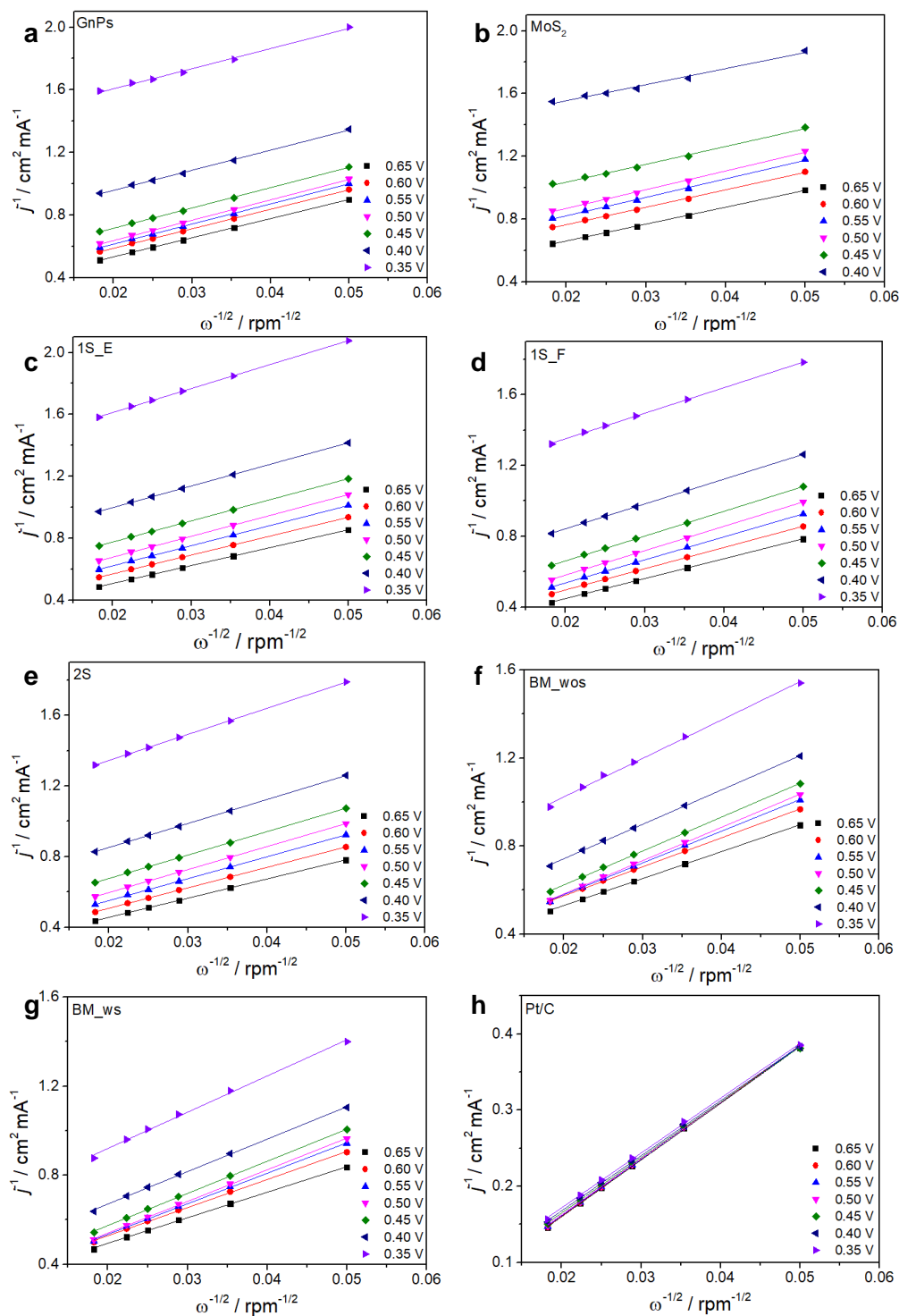


Figure 52. ORR polarization Koutecky-Levich (K-L) plots for **a** GnPs, **b** MoS<sub>2</sub>, **c** 1S\_E, **d** 1S\_F, **e** 2S, **f** BM\_wos, **g** BM\_ws and **h** Pt/C, extracted from data in Figure 46.

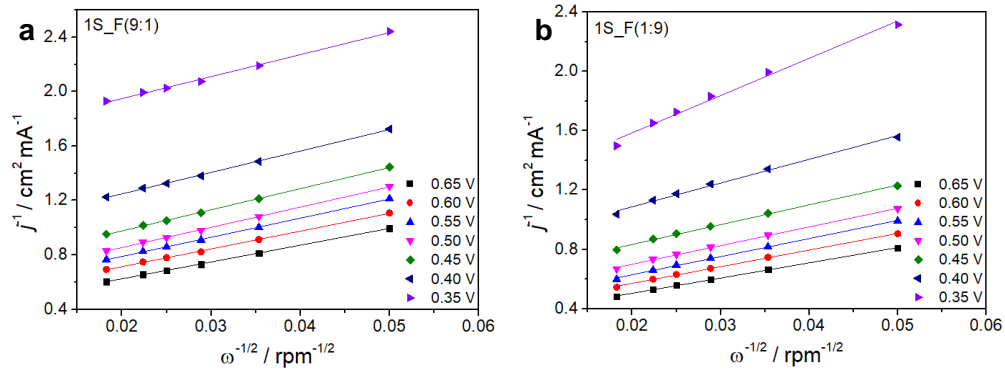


Figure 53. ORR polarization Koutecky-Levich (K-L) plots for **a** 1S\_F(9:1) and **b** 1S\_F(1:9), extracted from data in Figure 47.

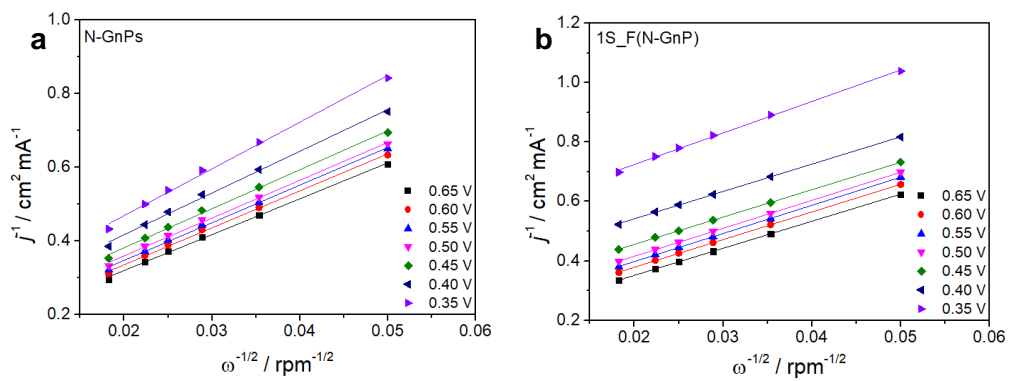


Figure 54. ORR polarization Koutecky-Levich (K-L) plots for **a** N-GnPs and **b** 1S\_F(N-GnP), extracted from data in Figure 48.

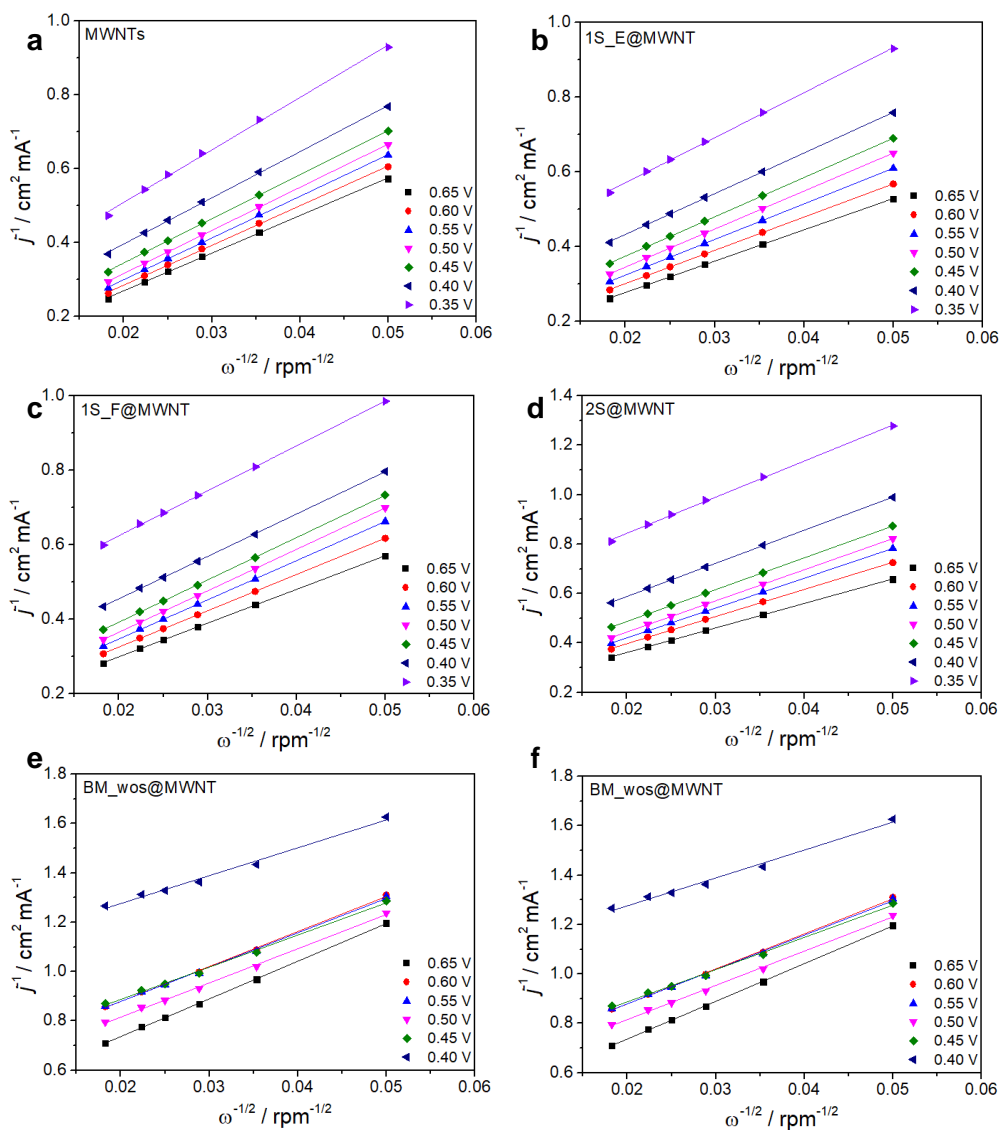


Figure 55. ORR polarization Koutecky-Levich (K-L) plots for **a** MWNTs, **b** 1S\_E@MWNT, **c** 1S\_F@ MWNT, **d** 2S@MWNT, **e** BM\_wos@MWNT and **f** BM\_ws@MWNT, extracted from data in Figure 49.

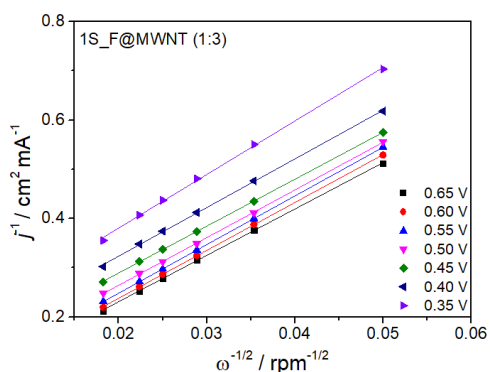


Figure 56. ORR polarization Koutecky-Levich (K-L) plots for 1S\_F@MWNT (1:3), extracted from data in Figure 50.

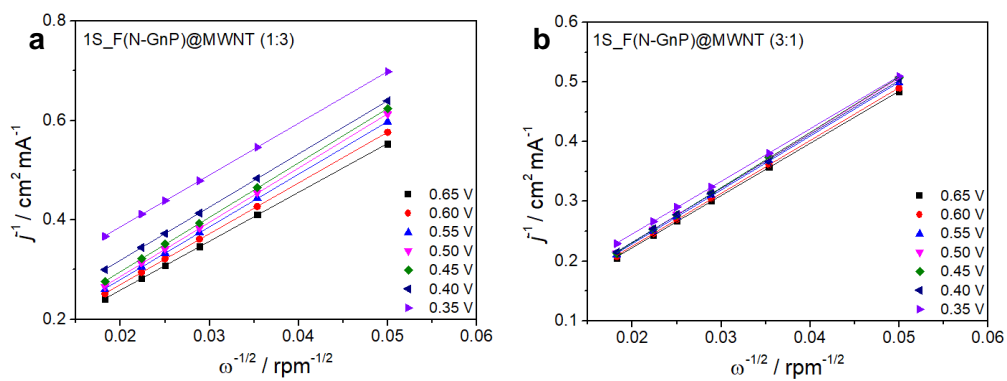


Figure 57. ORR polarization Koutecky-Levich (K-L) plots for **a** 1S\_F(N-GnP)@MWNT (1:3) and **b** 1S\_F(N-GnP)@MWNT (3:1), extracted from data in Figure 51.